THE MAGNETIC PROPERTIES OF THE SYSTEMS $La_xY_{1-x}TiO_3$, $La_xGd_{1-x}TiO_3$, $LaTiO_3$ AND $CeTiO_3$

By

© JOHN PAUL GORAL, B.Sc.

A Thesis
Submitted to the School of Graduate Studies
in Partial Fulfilment of the Requirements
for the Degree
Doctor of Philosophy

McMaster University
December 1982

MAGNETIC PROPERTIES OF
$La_xY_{1-x}TiO_3$ AND $La_xGd_{1-x}TiO_3$

DOCTOR OF PHILOSOPHY (1982)
(Chemistry)

McMASTER UNIVERSITY
Hamilton, Ontario

TITLE: The Magnetic Properties of the Systems $La_xY_{1-x}TiO_3$, $La_xGd_{1-x}TiO_3$, $LaTiO_3$ and $CeTiO_3$

AUTHOR: John Paul Goral, B.Sc. (McMaster University)

SUPERVISOR: Professor J.E. Greedan

NUMBER OF PAGES: xi, 133

ABSTRACT

The magnetic structures of $LaTiO_3$ and $CeTiO_3$ were determined by neutron diffraction. $LaTiO_3$ is a G-type antiferromagnet. The Ti^{3+} sublattice in $CeTiO_3$ displays G-type and possibly F-type ordering. The Ce^{3+} sublattice exhibits F-type and C-type components.

Solid solutions of the form $La_xY_{1-x}TiO_3$ and $La_xGd_{1-x}TiO_3$ were prepared. Magnetic measurements suggest a weakening of the antiferromagnetic Ti-O-Ti exchange as the Ti-O-Ti bond angle decreases from 157° ($LaTiO_3$). For sufficiently small bond angle, the Ti-Ti exchange becomes ferromagnetic. Crystal field calculations based on a localized Ti^{3+} $3d^1$ electron have reproduced the general features of susceptibility data reported for $La_xY_{1-x}TiO_3$ $(x = 0, .1, .2, .4, .7)$. This is in agreement with resistivity measurements undertaken on $La_{.1}Y_{.9}TiO_3$ and $La_{.2}Y_{.8}TiO_3$ which are characteristic of an activated transport mechanism.

ACKNOWLEDGEMENTS

I sincerely thank my supervisor, J.E. Greedan for his patience and good humor during the last five years. I also appreciate the helpful discussions with C.V. Stager, T. Birchall, M.F. Collins and D.A. Goodings.

Invaluable technical assistance was provided by J.D. Garrett, H.F. Gibbs, G. Hewitson and J. Couper. I am especially grateful to Helen Kennelly for her perserverance during the typing of this work.

TABLE OF CONTENTS

LIST OF FIGURES

LIST OF TABLES

CHAPTER 1

INTRODUCTION

1.1 Scope and Intent

The magnetic properties of the rare earth-transition metal perovskites RMO_3 (R = Lanthanide^{3+} ; M = Al,V,Cr,Mn,Fe) have been thorougly investigated and are well documented (Goodenough and Longo 1970, Hornreich 1978). Considerably less is known about the isostructural $RTiO_3$ compounds. These are the only reported examples of magnetically ordered Ti^{3+} oxide systems. The magnetic structures of the heavy rare earth titanites (R = Tb^{3+}, Dy^{3+}, Ho^{3+}, Er^{3+}, Tm^{3+}, Yb^{3+}) have been determined by Turner, Collins and Greedan. (Turner et.al. 1981, Turner et al. 1980). In all the above cases the Ti^{3+} moments align ferromagnetically. Magnetization and transport measurements imply that the magnetic moments are localized (Turner and Greedan 1980, Bazuev and Shveiken 1978). In contrast, magnetization and transport data collected on the light rare earth titanites $RTiO_3$ (R = La^{3+}, Ce^{3+}, Pr^{3+}, Nd^{3+}) are difficult to interpret assuming that the Ti^{3+} moments are both localized and ferromagnetically ordered (MacLean and Greedan 1981, MacLean et al. 1981, Bazuev et al. 1975).

The intent of this work is to further investigate the magnetic and transport properties of the $RTiO_3$ system. In the remainder of this chapter, some concepts useful in understanding the magnetic behaviour of these compounds are introduced. A theory due to Goodenough (1971) which rationalizes the magnetic and transport properties of perovskite materials based on structural arguments is also presented. In chapter 2, the details of sample preparation and analysis are summarized. The magnetic structure determinations of $LaTiO_3$ and $CeTiO_3$ by neutron diffraction are described in the next chapter. Following this, magnetic and transport measurements on the solid solution series $La_xY_{1-x}TiO_3$ are discussed and comparisons are made with other $RTiO_3$ compounds. In chapter 5 unusual susceptibility data collected on the $La_xY_{1-x}TiO_3$ system (MacLean 1980) are explained in terms of crystal field effects. The magnetic properties of the $La_xGd_{1-x}TiO_3$ solid solutions are described in chapter 6. Finally, the applicability of Goodenough's theory to the rare earth titanite system is discussed.

1.2 Magnetic Interactions

1.2.1 General Comments

The concept of magnetic exchange was first described by Heisenberg and Dirac in 1926. Applying the Pauli exclusion principle to a system of two localized electrons in a potential field, an energy difference between states of parallel and antiparallel spin is predicted. If the electrons occupy orthogonal orbitals, the parallel spin state is of lower energy (van Vleck 1965, Mattis 1965). In a simplistic view, this forms the basis of ferromagnetic ordering. Dirac showed in 1929 that H_{ex}, the exchange Hamiltonian for two electrons occupying localized orbitals, may be expressed in the following form:

$$H_{ex} = - J_{12}\vec{S}_1 \cdot \vec{S}_2 .$$

$\vec{S}_1, \vec{S}_2$ are the electron spins. J_{12} is the exchange integral between electrons (1) and (2) residing in single electron orbitals ψ_a, ψ_b.

$$J_{12} = \iint \psi_a^*(1)\psi_b^*(2)H'\psi_a(2)\psi_b(1) .$$

H' is the Hamiltonian representing the electron-electron interactions.

Although the Heisenberg exchange Hamiltonian is valid only in the severely limited circumstances described above, it has been applied to almost all magnetic systems. This is due mainly to its simple form and its success in rationalizing the gross magnetic properties of many compounds. The precise expression for the exchange Hamiltonian in a real magnetic system is extremely difficult to derive. It is necessary to determine the nature of the electron-electron correlations in a many particle system. Instead it is usual to treat the exchange Hamiltonian as a phenomenological expression limited only by the symmetry of the system. Normally however, a Heisenberg term is the dominant contribution.

Keffer (1966) discusses non-Heisenberg contributions to the total spin Hamiltonian. For example, van Vleck (1937) has suggested that spin orbit coupling may result in a pseudo-dipolar term of the form:

$$H_{ex} \propto (\vec{S}_1 \cdot \vec{r}_{12})^2 (\vec{S}_2 \cdot \vec{r}_{12})^2 \quad .$$

Dzialoshinski (1958) and Moriya (1960) have postulated an anti-symmetric coupling of the following type:

$$H_{ex} \propto \vec{D} \cdot (\vec{S}_1 \times \vec{S}_2) \quad .$$

$\vec{D}$ is a phenomenological vector which is dependent on the crystal symmetry. It has been proposed that the coupling between the rare earth and transition metal sublattices in the rare earth orthochromites is effected through this mechanism (Courths and Huffner 1975).

1.2.2 Mean Field Theory

One of the most common approaches to the analysis of magnetic interactions is the molecular field theory first introduced by Weiss in 1907. Originally derived for a ferromagnetic system, molecular field theory has been extended to anti-ferromagnets as well as ferrimagnets. The development of this theory may be found in a number of texts (Ashcroft and Merman

1976, Morrish 1965, Smart 1966). Some of the useful results will be reproduced here. The fundamental assumption of this theory is that the magnetic interactions between any single atom and the rest of the solid may be approximated by an effective magnetic field H_e. The magnitude of H_e is proportional to the magnetization M.

$$H_e = \lambda M \ .$$

In the case of a paramagnetic system, the magnetic species are assumed to be non-interacting. The magnetization has the form:

$$M = NgJB_J(x) \ .$$

N is the number of particles in the system, each possessing angular momentum J. g is the Landé splitting factor.

$$g = 1 + \frac{J(J+1)+S(S+1)-L(L+1)}{2J(J+1)} \ .$$

$B_J(x)$ is the Brillouin function.

$$B_J(x) = \left(\frac{2J+1}{2J}\right)\coth\left(\frac{(2J+1)x}{2J}\right) - \frac{1}{2J}\coth\left(\frac{x}{2J}\right) \ .$$

$x = \frac{gJH_0}{kT}$. H_0 is an applied magnetic field.

At high temperatures and low magnetic field $(x \ll 1)$ M reduces to a simpler form.

$$M = \frac{Ng^2J(J+1)H_0}{3kT} .$$

The magnetic susceptibility χ is defined as $\frac{\partial M}{\partial H_0}$.

$$\chi = \frac{Ng^2J(J+1)}{3kT} = \frac{C}{T} .$$

This is the well-known Curie law. It predicts a linear relationship between χ^{-1} and T. The Curie constant C is the inverse slope of this curve. It is characteristic of the J value of the paramagnetic species.

Interactions between the magnetic species may lead to a magnetically ordered state at non-zero temperature. An effective field H_e is created, due to the spontaneous ordering. The strength of the interaction is expressed by the magnitude of the coupling constant λ. In the high temperature expression for the paramagnetic magnetization, the applied magnetic field H_0 is replaced by the sum H_0+H_e.

$$M = \frac{C}{T} (H_0+H_e) .$$

Since $H_e = \lambda M$

$$M = \frac{C}{T} (H_0+\lambda M) = \frac{H_0C}{T} \left(\frac{T}{T-\lambda C}\right) .$$

Since $\chi = \partial M/\partial H_0$

$$\chi = \frac{C}{T-\theta} , \quad \theta = \lambda C , \quad \begin{array}{l} \lambda > 0 \text{ for a ferromagnet} \\ \lambda < 0 \text{ for an antiferromagnet.} \end{array}$$

The result is the Curie-Weiss law. At temperatures sufficiently large with respect to the magnetic coupling strength, the inverse susceptibilities of ferromagnets, ferrimagnets, antiferromagnets and paramagnets are all predicted to be linear with temperature. The Weiss constant θ may provide information on the nature of the magnetic coupling. Interpretation of this parameter is often ambiguous since the sign and magnitude of θ are also sensitive to crystal field effects (Mabbs and Machin 1973).

Molecular field theory was first applied to a ferrimagnetic system by Neel in 1948. He considered the antiferromagnetic coupling between two magnetic sublattices, A and B each possessing a different magnetic moment. In this case it is necessary to define two different effective fields.

$$H_e^A = \lambda_{A-A}M_A+\lambda_{A-B}M_B$$

$$H_e^B = \lambda_{B-B}M_B+\lambda_{A-B}M_A \quad .$$

M_A is the magnetization originating from ordering of the A sublattice. H_e^A is the effective field experienced by an atom on the A sublattice. λ_{A-A} represents the exchange coupling between atoms on the A sublattice. The inverse susceptibility is predicted to fit a four parameter hyperbola of the following form.

$$\chi^{-1} = \frac{T-\theta}{C} - \frac{\xi}{T-\theta'} \quad .$$

Both the Curie constant C and the Weiss constant θ have been previously discussed. ξ and θ' are parameters describing the curvature of the hyperbola at low temperature. From analysis of this curve, the mean field coupling constants λ_{A-A}, λ_{A-B} and λ_{A-B} may be determined.

$$\theta = -\frac{1}{C}\left(2C_AC_B\lambda_{A-B}-C_A^2\lambda_{A-A}-C_B^2\lambda_{B-B}\right)$$

$$\theta' = \frac{C_AC_B}{C}\left(2\lambda_{A-B}+\lambda_{B-B}+\lambda_{A-B}\right)$$

$$\xi = \frac{C_AC_B}{C^3}\left[C_A^2(\lambda_{A-A}+\lambda_{B-B})^2+C_B^2(\lambda_{B-B}+\lambda_{A-B})^2\right.$$

$$\left.-2C_AC_B(\lambda_{A-B}^2+(\lambda_{A-A}+\lambda_{B-B})\lambda_{A-B}+\lambda_{A-A}\lambda_{B-B})\right]$$

1.2.3 Spin Glasses

A new class of materials characterized by short range magnetic ordering has received much attention since 1972. In these compounds, the spins of certain of the magnetic species freeze into random orientations below some characteristic temperature. These materials are termed spin glasses or mictomagnets. The nature of the spin glass state is as yet not well understood. It has been suggested that the spin glass transition arises from weak interactions between randomly distributed magnetic clusters. Indeed this effect was first reported for metallic alloys such as AuFe (Cannella and Mydosh 1972). These materials have also been referred to as 'frustrated' magnetic systems. Toulouse (1977) has suggested that this short range ordering may be due to the competition between negative and positive exchange interactions in a randomly distributed magnetic system. The characteristic signature of the spin glass ordering temperature is the appearance of a cusp-like anomaly in the magnetic susceptibility. This anomaly is suppressed on application of an external magnetic field. Time dependent remanence effects have also been observed. The properties of the spin glass state are more fully described in the reviews of Mydosh (1978), Ford (1982) and the references contained therein.

1.3 A Proposed Relation Between Structure and Electronic Properties

All the materials to be discussed crystallize in the same orthorhombic distortion of the cubic perovskite structure. A corner-sharing network of oxygen octahedra forms the skeletal framework of the ideal perovskite. These octahedra are arranged in perfectly aligned linear chains in three dimensions. A transition metal ion (Ti^{3+}) occupies the body centre of each octahedron. The cubic perovskite structure is stabilized by a large cation ($Lanthanide^{3+}$) which occupies a 12-fold cubo-octahedral site (Fig. 1.1). The nearest neighbour Ti-Ti contacts are not direct but include an intervening oxide ion. In the ideal perovskite the Ti-O-Ti bond angle is exactly 180°.

In the case of the $RTiO_3$ compounds the rare earth ion is too small to stabilize the ideal structure. This leads to a cooperative distortion and buckling of the oxygen octahedra

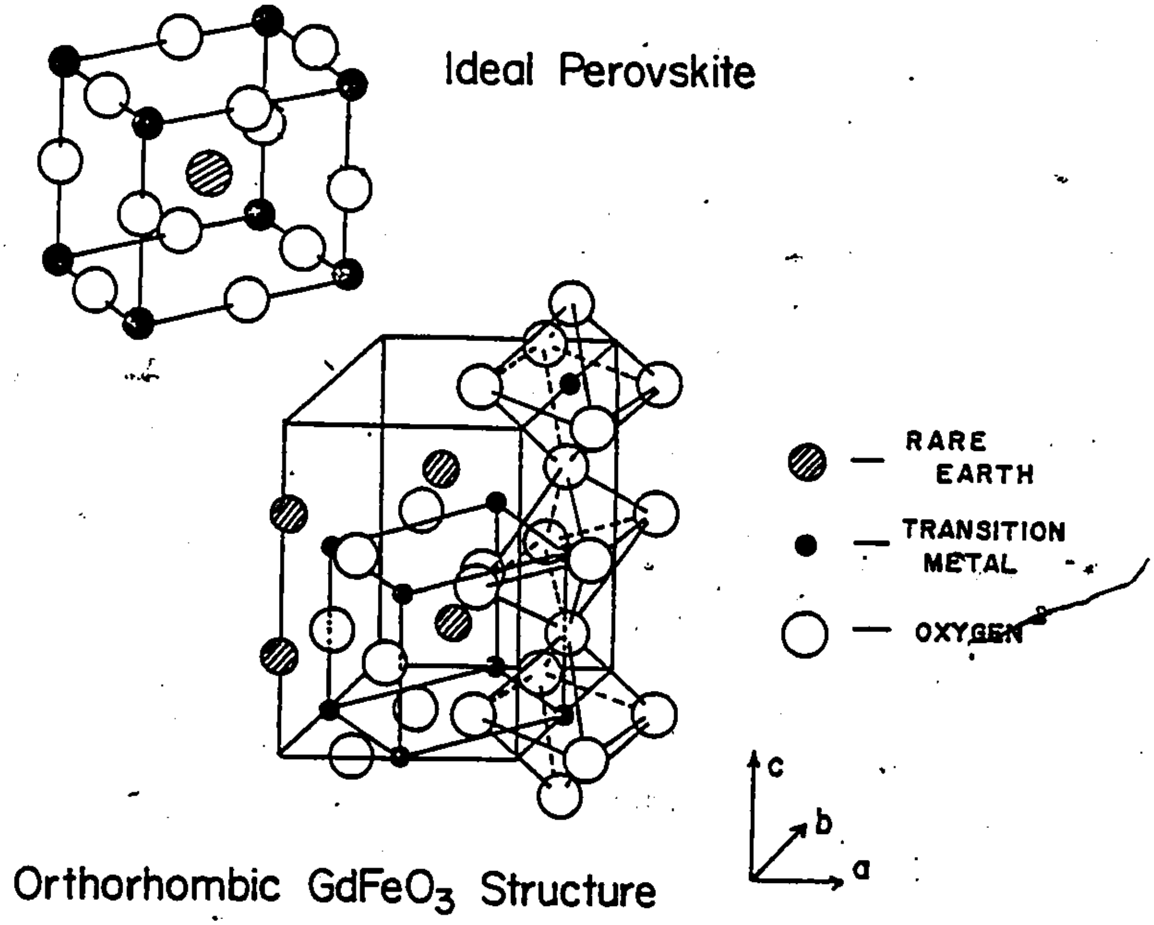

Ideal Perovskite

Orthorhombic $GdFeO_3$ Structure

Fig. 1.1 The ideal perovskite and $GdFeO_3$ structures.

(Fig. 1.1). The result is the $GdFeO_3$ structure which belongs to the orthorhombic space group Pbnm. There are four formula units per unit cell. The symmetry at the Ti^{3+} site is reduced from m3m to $\bar{1}$ and the rare earth coordination drops to 8-fold. As the size of the rare earth ion decreases, the orthorhombic distortion becomes more pronounced. Note the effect of this distortion on the Ti-O-Ti bond angle. (In fact, in these materials there are two different Ti-O-Ti bond angles whose magnitudes differ by ∿ 2°.) In both cases the Ti-O-Ti bond angle decreases from 180° as the rare earth becomes smaller. Anticipating results to be discussed later, the Ti-O-Ti bond angle is an important characteristic of these compounds. However, the magnitude of this angle is not always known by direct measurement. Instead, the variation in the Ti-O-Ti bond angle has been monitored by means of the cube of the effective rare earth radius which is readily obtainable from the compilation of Shannon (1976). The correlation between these two parameters is demonstrated in Fig. 1.2. Here the average Ti-O-Ti bond angle is plotted against (rare earth radius)^3 for the members of the $RTiO_3$ series whose crystal structures have been solved (MacLean et al. 1979, Appendix I). The correlation is quite good.

It has been proposed that the Ti-O-Ti bond angle is a determining factor in both transport and magnetic properties of perovskite related materials. Goodenough (1966) argues that the transport properties of these materials are governed by the d electrons of the transition metal. He points out that the outer

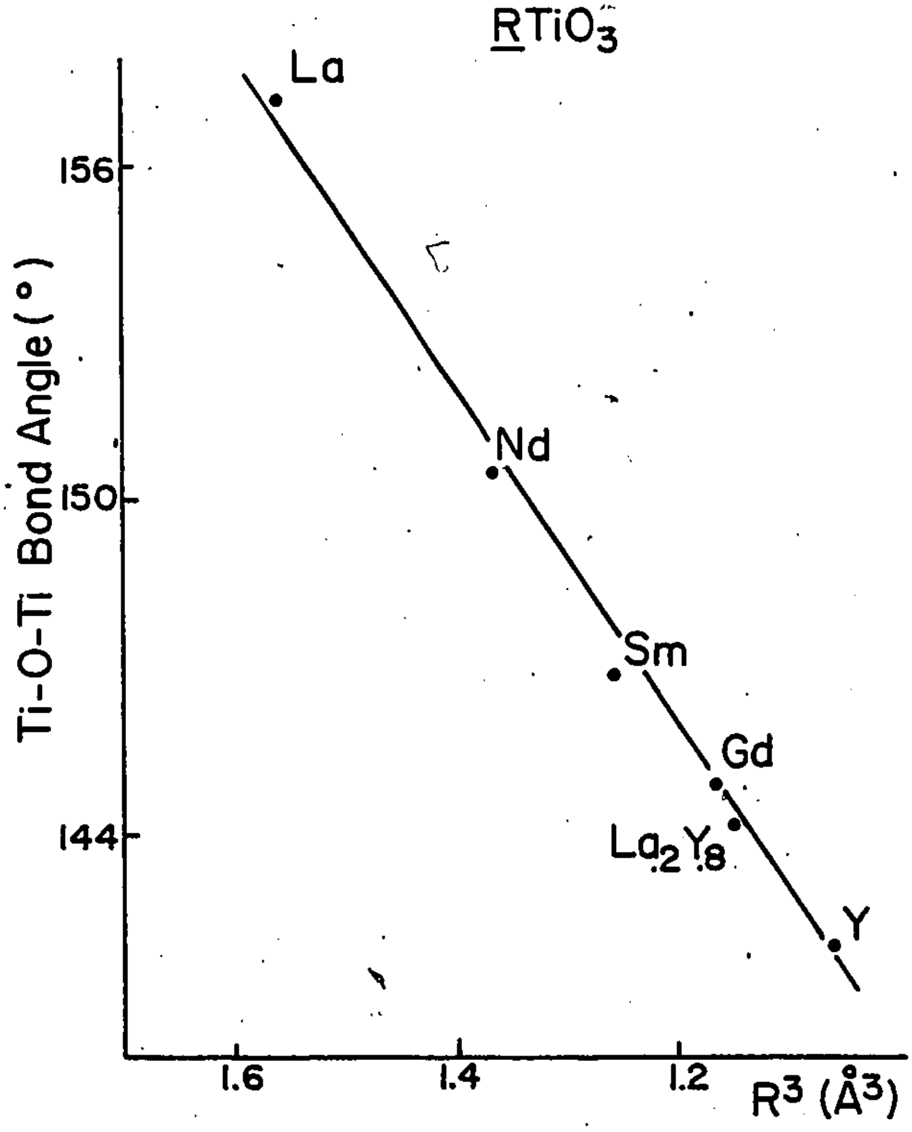

Fig. 1.2 Average Ti-O-Ti bond angle vs. (effective rare earth radius)^3 for the $RTiO_3$ phases whose crystal structures have been reported.

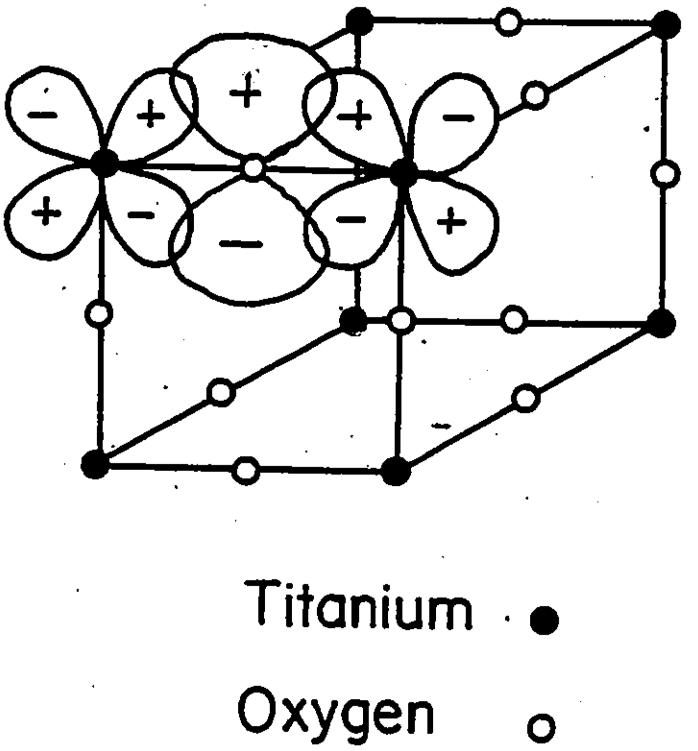

Fig. 1.3 The proposed dπ-pπ-dπ interaction pathway for the Ti^{3+} 3d^{1} electron.

s and p orbitals of neighbouring atoms in a crystal overlap sufficiently to form filled, low energy bands. The unpaired 4f electrons of the rare earth may be treated as localized since they are well screened by the 5s and 5p electrons. The d electrons form an intermediate regime whose properties are dependent on the extent of d-orbital overlap. Since the Ti^{3+} ion in the $RTiO_3$ phases is in octahedral coordination the $3d^1$ electron is assumed to occupy a t_{2g} like atomic orbital. This orbital is of the correct symmetry to interact with the pπ orbital on O^{2-} (Fig. 1.3). When the Ti-O-Ti bond angle is 180°, the dπ-pπ-dπ overlap is maximized and itinerant electron behaviour is predicted. This situation is most closely realized for $LaTiO_3$ and $CeTiO_3$, the $RTiO_3$ compounds having the largest rare-earth ion (MacLean and Greedan 1981). As the size of the rare earth becomes smaller and the magnitude of the Ti-O-Ti bond angle decreases, orbital overlap becomes less favourable. This corresponds to a narrowing of the electron bands finally resulting in localized electron behaviour.

The Ti-O-Ti bond is also the proposed pathway of the magnetic interactions. This superexchange mechanism involves the transfer of electrons between the titanium and oxygen orbitals, forming excited states of the Ti-O-Ti system. Anderson (1950) has pointed out that since the superexchange is effected by means of electron transfer through an O^{2-} p-type orbital, the strongest coupling should occur when the transition metal orbitals have a similar symmetry. This corresponds to the maxima in the wavefunction of the O^{2-} and two neighbouring Ti^{3+} ions being colinear, i.e. Ti-O-Ti = 180°.

The sign and exact magnitude of the resulting exchange is difficult to determine. Predictions have been made for 180° and 90° superexchange in perovskite like materials (Goodenough 1958, Kanamori, 1959, Goodenough 1963). For the d^1 system, antiferromagnetic superexchange coupling is predicted at 180° (Martin, 1968). In the 90° case both ferromagnetic and antiferromagnetic interactions come into play. The sign of the coupling cannot in general be predicted since the resultant configuration is highly sensitive to the extent of the orbital overlap. The situation is even more complex for the $RTiO_3$ materials since the bond angles are neither 180° nor 90°, but intermediate in the range 157° - 134°. A phenomenological phase diagram relating the magnetic and transport properties of the Ti^{3+} sublattice to the extent of the $d\pi$-$p\pi$-$d\pi$ orbital overlap has been proposed for the $RTiO_3$ system (Fig. 1.4) (Goodenough 1971). The operative parameter is the transfer integral b which expresses the extent of interaction of the titanium ions through orbital overlap with the intervening oxide ion. The magnitude of b diminishes as the Ti-O-Ti bond angle decreases and the orbital overlap becomes less effective.

This phenomenological theory predicts a transition from itinerant to localized electron behaviour as the rare earth ion

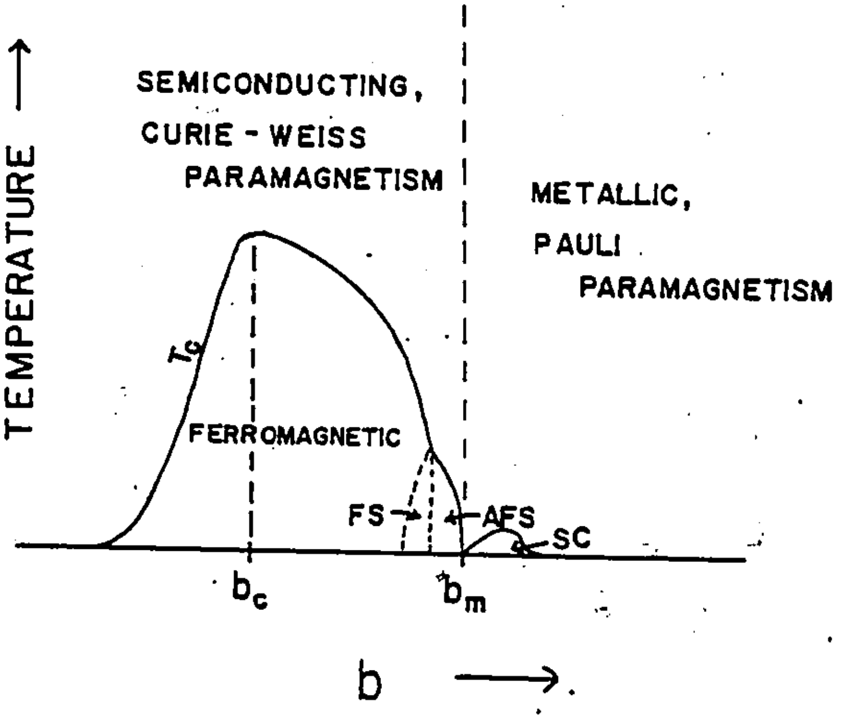

Fig. 1.4 A phenomenological phase diagram for the $RTiO_3$ series. FS = ferromagnetic spiral, AFS = antiferromagnetic spiral, SC = superconducting (from Goodenough 1971).

becomes smaller and the Ti-O -Ti bond angle decreases. In addition, the Ti-Ti exchange interactions may become less strongly antiferromagnetic changing sign at some intermediate Ti-O-Ti angle.

CHAPTER 2

SAMPLE PREPARATION AND ANALYSIS

2.1 Preparation

Polycrystalline samples of the following compounds were prepared:

(i) $La_xY_{1-x}TiO_3$ (x = .3,.4,.5,.6,.7,.8,.9,.95,1.0)

(ii) $La_xGd_{1-x}TiO_3$ (x = 0,.02,.05,.1,.3,.4 ,.5,.6,.7, .8,.9,.95,1.0)

(iii) $CeTiO_3$.

For all phases except $CeTiO_3$, the same starting materials were used; Ti_2O_3 and the appropriate rare earth oxide(s) R_2O_3 (99.99% Research Chemicals):

$$R_2O_3+Ti_2O_3 \rightarrow 2RTiO_3 .$$

The rare earth oxides were prefired for 12 hours in air at 1000°C. Ti_2O_3 was prepared by arc-melting Ti sponge (99.99% Alpha Inorganics) and TiO_2 (99.95% Atomergic Chemicals):

$$Ti+3TiO_2 \rightarrow 2Ti_2O_3 .$$

Since the products tended to be slightly oxidized, a reduced form of titanium sesquioxide ($\sim Ti_2O_{2.98}$) was often used. $CeTiO_3$ ~~was~~ prepared using CeO_2.

$$CeO_2 + TiO \rightarrow CeTiO_3 \; .$$

TiO was made in the same manner as Ti_2O_3.

$CeTiO_3$, $La_xY_{1-x}TiO_3$ ($x = .3 - 1.0$) and $La_xGd_{1-x}TiO_3$ ($x = .6 - 1.0$) were prepared by arc-melting. The appropriate mixtures of the titanium oxide and rare earth oxides were weighed and pressed into pellets. The pellets were placed on a rotating water-cooled copper hearth and outgassed under a stream of high purity argon. The sample was melted for a period of about one minute. The boule was turned over and the heating repeated at least three times. $GdTiO_3$-$La_{.5}Gd_{.5}TiO_3$ were prepared by solid state reaction. Pellets of the starting materials were sealed under argon in molybdenum crucibles and subjected to radio frequency heating near 1500°C for about 18 hrs.

Single crystals of $La_{.1}Y_{.9}TiO_3$, $La_{.2}Y_{.8}TiO_3$ and $La_xGd_{1-x}TiO_3$ ($x = 0, .02, .05, .1$) were grown by the Czochralski technique (Laudise 1970). The growth was carried out in a tri arc furnace. Pellets of the starting materials were placed on the molybdenum core of a rotating water cooled graphite hearth. They were outgassed under a stream of titanium-gettered high purity argon. A gas flow of ∿ 4 litres/minute was maintained for the duration of the crystal growth. The tungsten tipped seed rod was water cooled. The hearth and seed rod were counter-rotated at a rate of ∿ 20 rpm while the pull rate was in the range 1 - 2 cm/hr. The largest crystals were found in the middle of the boule growing in a starburst from the tip of the seed rod. Crystals of about 20 mg (1 - 5 mm dimensions) consisting of one or two grains were extracted. Laue photographs confirmed that the misalignment of the grains was on order of 2°.

2.2 Analysis

The Ti^{3+} content was monitored by thermogravimetric analysis, TGA. The product was weighed before and after heating in air at 1000°C for at least four hours.

$$2RTi^{(3+)}O_3 + \frac{1}{2} O_2 \rightarrow R_2Ti_2^{(4+)}O_7 \quad .$$

The results are listed in Table 2.1. As was mentioned previously, the products tended to be slightly oxidized. In fact, earlier preparations of the $La_xGd_{1-x}TiO_3$ phases using the solid state reaction technique yielded severely oxidized single phase materials. The extent of oxidation became more pronounced as the reaction time was lengthened and the La content was increased. TGA results and cell constants for the heavily oxidized phases $La_xGd_{1-x}TiO_3$ (x = .02 - .5) are given in Table 2.2. The effect of the oxidation is to decrease the size of the unit cell. Note also that the critical temperatures of these oxidized phases are lower than those observed for the stoichiometric materials. Oxidative non-stoichiometry is well known in perovskite materials. Single phase materials of compositions between $LaTiO_3$-$La_{2/3}TiO_3$ and $CeTiO_3$-$Ce_{2/3}TiO_3$ have been reported previously (Kestigian and Ward 1955, Bazuev et al. 1978).

Table 2.1

Oxidative Weight Gain Data for $La_xY_{1-x}TiO_3$

	Weight gain (theoretical)	Weight gain (observed)	$100\times(\frac{wtg(theo)-wtg(obs)}{wtg(theo)})$
$La_{0.3}$	4.00	3.86	3.5
$La_{0.4}$	3.91	3.82	2.3
$La_{0.5}$	3.81	3.84	-0.8
$La_{0.6}$	3.72	3.74	-0.5
$La_{0.7}$	3.64	3.64	0
$La_{0.8}$	3.56	3.62	-1.7
$La_{0.9}$	3.48	3.37	3.2
$La_{0.95}$	3.44	3.35	2.6
$LaTiO_3$	3.41	3.28	3.8

Oxidation Weight Gain (wtg) for $La_xGd_{1-x}TiO_3$

	wtg_{theo} (%)	wtg_{obs} (%)	$(\frac{wtg_{theo}-wtg_{obs}}{wtg_{theo}})\times 100$ (%)
$LaTiO_3$	3.41	3.28	3.8
$La_{0.95}$	3.39	3.26	3.8
$La_{0.9}$	3.38	3.30	2.4
$La_{0.8}$	3.35	3.36	-.3
$La_{0.7}$	3.33	3.32	.3
$La_{0.6}$	3.30	3.27	1.0
$La_{0.5}$	3.28	3.31	-.8
$La_{0.4}$	3.25	3.21	1.2
$La_{0.3}$	3.23	3.29	-1.9
$La_{0.1}$	3.18	3.13	1.6
$La_{0.05}$	3.17	3.23	-1.9
$La_{0.02}$	3.16	3.09	2.2
$GdTiO_3$	3.16	3.09	2.2

Table 2.2

Weight Gain Data for the Heavily Oxidized Phases $\mathrm{La_xGd_{1-x}TiO_3}$

	% $\mathrm{Ti^{4+}}$	RE Vacancy (%)	T_c	T_c (final product)
$\mathrm{La_{.02}}$	13	4	24	30
$\mathrm{La_{.05}}$	13	4	20	22
$\mathrm{La_{.1}}$	31	10	15	18
$\mathrm{La_{.4}}$	31	10	8	14
$\mathrm{La_{.5}}$	37	13	8	16

Lattice Constants for the Heavily Oxidized Phases
$\mathrm{La_xGd_{1-x}TiO_3}$

	a(Å)	b(Å)	c(Å)	Volume (Å^3)	Volume (final product)
$\mathrm{La_{.02}}$	5.399	5.680	7.692	235.9	(236.9)
$\mathrm{La_{.05}}$	5.411	5.679	7.698	236.6	(237.1)
$\mathrm{La_{.1}}$	5.427	5.677	7.712	237.6	(237.6)
$\mathrm{La_{.2}}$	5.451	5.649	7.733	238.1	(239.3)
$\mathrm{La_{.3}}$	5.462	5.634	7.766	239.0	(240.7)
$\mathrm{La_{.4}}$	5.480	5.611	7.784	239.3	(241.7)
$\mathrm{La_{.5}}$	5.487	5.579	7.817	239.3	(243.0)

Table 2.3

Cell constants for $La_xY_{1-x}TiO_3$

	a(Å)	b(Å)	c(Å)	V(Å^3)
*$YTiO_3$	5.340(5)	5.690(5)	7.611(5)	231.2(5)
*$La_{0.1}$	5.366(3)	5.677(3)	7.651(5)	233.1(4)
*$La_{0.2}$	5.395(3)	5.672(3)	7.684(5)	235.1(4)
$La_{0.3}$	5.429(5)	5.677(6)	7.725(15)	238.1(9)
$La_{0.4}$	5.462(10)	5.671(6)	7.736(7)	239.6(9)
$La_{0.5}$	5.477(10)	5.667(1)	7.769(8)	241.1(7)
$La_{0.6}$	5.517(11)	5.649(11)	7.815(1)	243.6(12)
$La_{0.7}$	5.589(11)	5.626(6)	7.879(15)	247.7(12)
$La_{0.8}$	5.566(11)	5.623(5)	7.930(16)	248.2(12)
$La_{0.9}$	5.593(11)	5.618(6)	7.937(8)	249.4(10)
$La_{0.95}$	5.626(4)	5.620(6)	7.913(14)	250.2(9)
$LaTiO_3$	5.633(10)	5.614(5)	7.940(6)	251.1(9)

* From MacLean (1980).

Cell constants for $La_xGd_{1-x}TiO_3$.

	a (Å)	b (Å)	c (Å)	Volume (Å^3)
$GdTiO_3$	5.409(5)	5.712(4)	7.681(7)	237.3(6)
$La_{0.02}$	5.409(5)	5.700(5)	7.683(6)	236.9(6)
$La_{0.05}$	5.414(5)	5.693(5)	7.694(8)	237.1(7)
$La_{0.1}$	5.429(5)	5.681(6)	7.705(8)	237.6(7)
$La_{0.2}$	5.450(5)	5.677(5)	7.733(9)	239.3(7)
$La_{0.3}$	5.475(6)	5.664(4)	7.762(5)	240.7(6)
$La_{0.4}$	5.497(6)	5.656(4)	7.789(6)	242.2(6)
$La_{0.5}$	5.516(6)	5.634(4)	7.820(6)	243.0(6)
$La_{0.6}$	5.532(11)	5.654(11)	7.830(12)	244.9(13)
$La_{0.7}$	5.561(9)	5.640(6)	7.864(16)	246.6(12)
$La_{0.8}$	5.593(10)	5.627(16)	7.885(11)	248.1(11)
$La_{0.9}$	5.622(4)	5.619(6)	7.908(11)	249.8(8)
$La_{0.95}$	5.621(4)	5.609(5)	7.917(12)	249.6(8)
$LaTiO_3$	5.633(10)	5.614(5)	7.940(6)	251.1(9)

Tofield and Scott (1974) have summarized the three types of oxidative non stoichiometry observed in ABO_3 perovskite-like structures. These are i) addition of interstitial oxygen, ii) vacancies on the A and B sites leaving the oxygen sublattice intact and iii) A vacancies only. Model (i) is unlikely due to the large size of the O^{2-} ion. The reduced size of the oxidized unit cell observed in Table 2.2 strongly suggests model (ii) or (iii). Assuming model (iii) the extent of the rare earth vacancies has been calculated to be as much as 13%.

The cell constants presented in Table 2.3 were derived by a least squares fit of 10 - 18 powder x-ray peaks. An internal Si or KCl standard was used in all cases. A Guinier camera was used to collect data for the phases $La_{.6}Y_{.4}TiO_3$-$La_{.9}Y_{.1}TiO_3$. In this composition range, peak overlap was especially severe. For all materials prepared, the observed powder patterns were indicative of single phase materials, consistent with a random distribution of the rare earth ions in the solid solution systems. A plot of cell volume vs. (rare earth radius)^3 yields a smooth curve for both the $La_xY_{1-x}TiO_3$ and $La_xGd_{1-x}TiO_3$ series (Fig. 2.1,2.2). A single crystal x-ray structure was undertaken on $La_{.2}Y_{.8}TiO_3$ (Appendix I). No superlattice reflections or violations of the expected symmetry were observed in the precession photographs. The data were refined in the $GdFeO_3$ structure assuming random distribution of the rare earth species. The weighted R factor of .0303 is comparable to

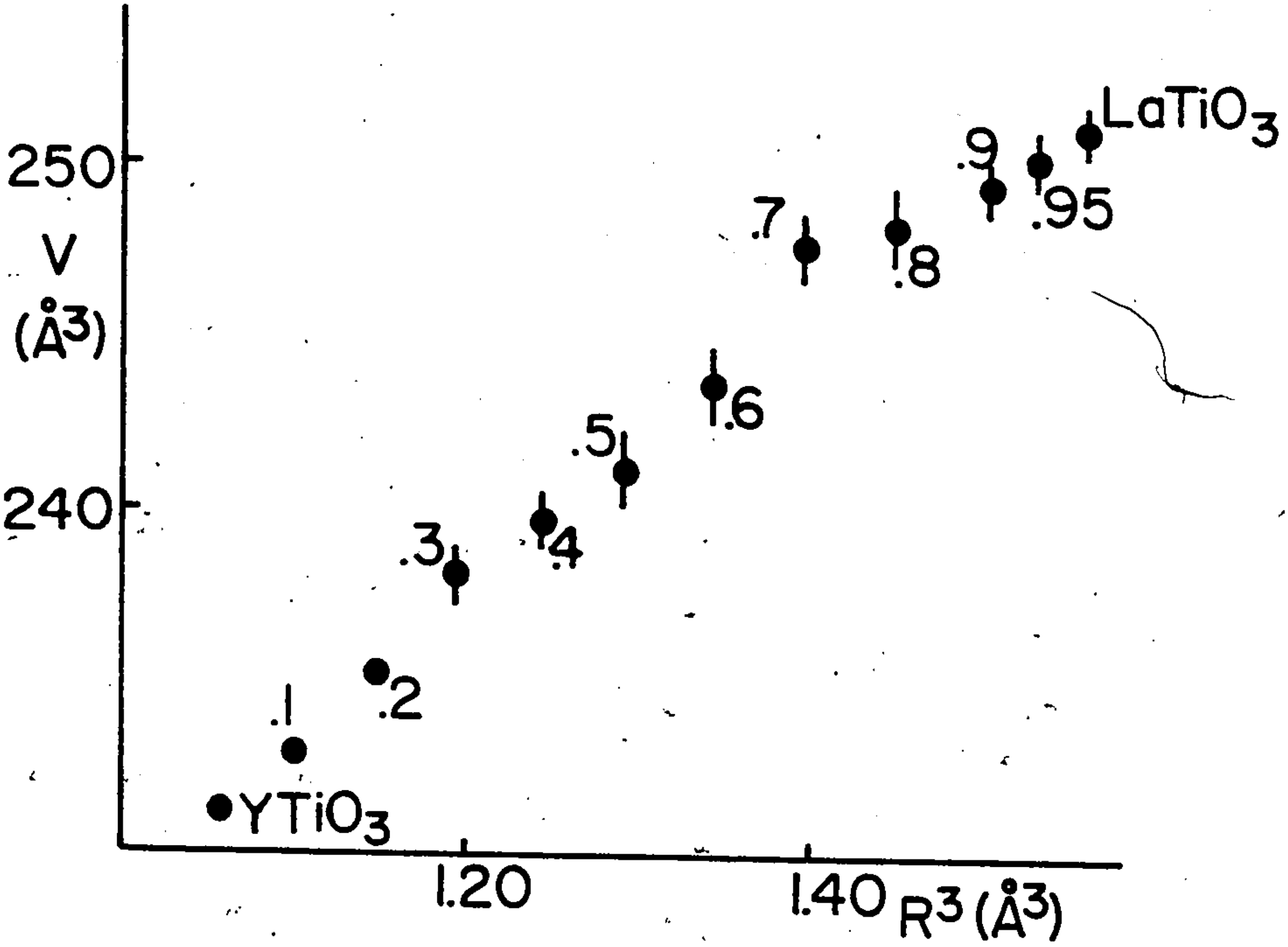

Fig. 2.1 Cell volume vs. (effective rare earth radius)^3 for the $La_xY_{1-x}TiO_3$ series. Error bars represent one standard deviation.

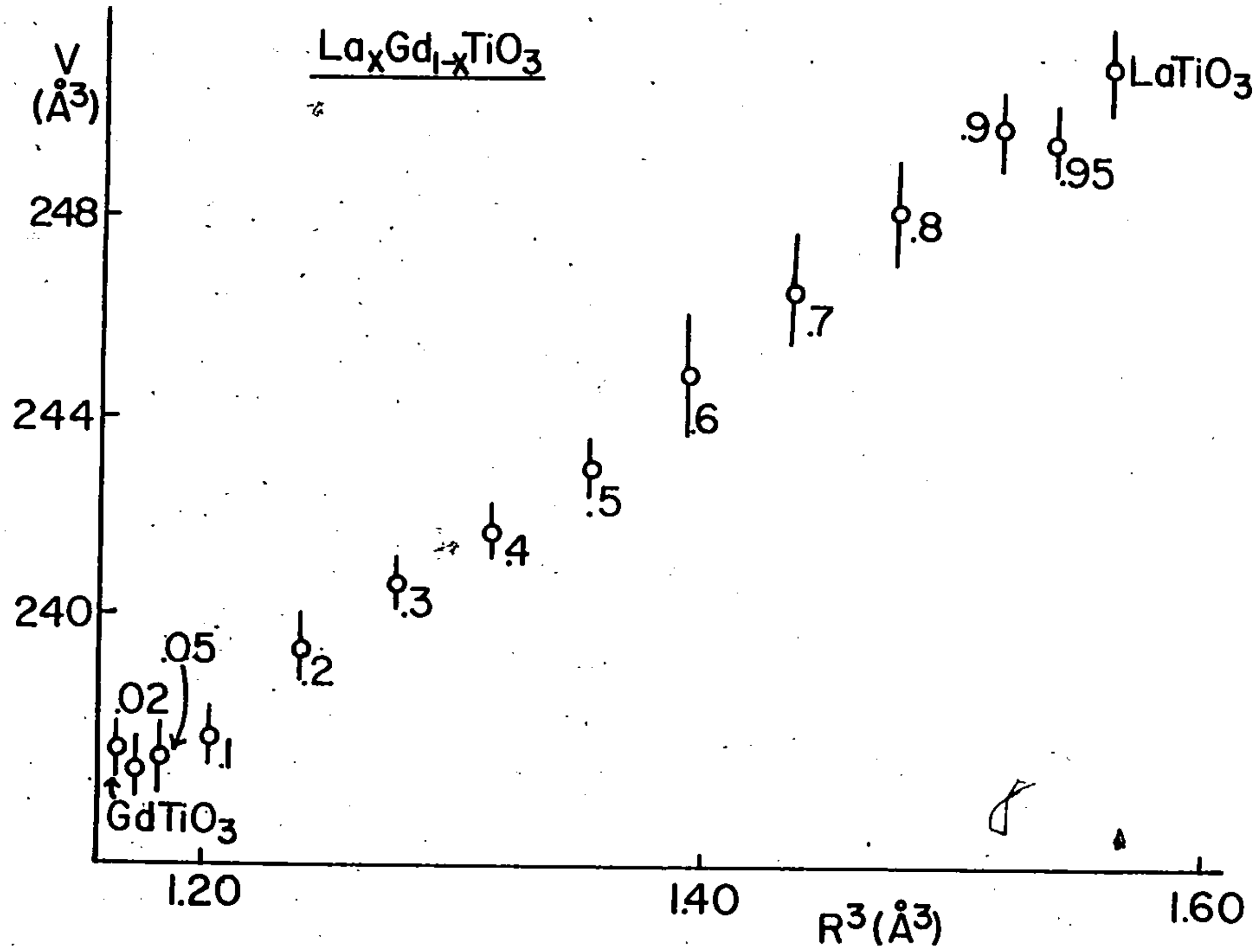

Fig. 2.2 Cell volume vs. (effective rare earth radius)^3 for the $La_xGd_{1-x}TiO_3$ series. Error bars represent one standard deviation.

those reported by MacLean et al. (1979) for the single species rare earth titanites. These data suggest that the solid solutions prepared are indeed single phase materials whose structure varies continuously as the rare earth ratio is altered.

CHAPTER 3

THE MAGNETIC STRUCTURES OF $LaTiO_3$ and $CeTiO_3$

3.1 Introduction

The magnetic structures of the heavy rare earth titanites $RTiO_3$ ($R = Tb^{3+}$, Dy^{3+}, Ho^{3+}, Er^{3+}, Tm^{3+}, Yb^{3+}) have been previously determined by neutron scattering (Turner et al. 1981, Turner et al. 1980). The rare earth ions display F-type and C-type magnetic components while ordering within the Ti sublattice is always ferromagnetic. Extensive work has also been carried out on the isostructural orthoferrites $RFeO_3$, and orthochromites $RCrO_3$ (Goodenough and Longo 1970, Hornreich 1978). In these materials, the ordering within the transition metal sublattices is predominantly antiferromagnetic, regardless of the identity of the rare earth ion.

The magnetic susceptibility of $LaTiO_3$ is temperature independent down to 125K, at which point it increases dramatically. A saturation moment of less than .01 μ_B molecule^{-1} at 4.2K has been reported along with a hysteresis in the magnetization-field curve (MacLean and Greedan 1981). These data point to a canted antiferromagnetic spin arrangement as observed for both $LaFeO_3$ and $LaCrO_3$ (Goodenough and Longo 1970). MacLean and Greedan (1981) also report magnetization data for

$CeTiO_3$. A critical temperature near 116K is clearly evident while the curvature at low temperatures may indicate a second T_c in the range 40K - 80K. The magnetic structures of $CeFeO_3$ and $CeCrO_3$ have not been reported.

Neutron diffraction measurements were undertaken on $LaTiO_3$ and $CeTiO_3$ in an attempt to determine the magnetic structures of these compounds, including the magnitude of the titanium (III) and cerium (III) moments.

3.2 Scattering Theory

In a magnetically ordered material the neutron may scatter coherently from both the nuclei and the unpaired electron density. For a beam of unpolarized neutrons the nuclear and magnetic contributions to the intensity are additive:

$$I_{hk\ell} \propto F^2_{hk\ell} = (F^N_{hk\ell})^2 + (q_{hk\ell}F^M_{hk\ell})^2 \qquad \text{(Bacon 1967).}$$

$F^N_{hk\ell}$, the nuclear structure factor for the reflection $hk\ell$, has the following form:

$$F^N_{hk\ell} = \sum_j b_j \exp 2\pi i(hx_j+ky_j+\ell z_j)\,\exp(-\omega_j) \ .$$

$\sum_j$ denotes a summation over the j atoms of the unit cell positioned at fractional co-ordinates (x_j, y_j, z_j). b_j is the neutron scattering length, characteristic of the atom j. $\text{Exp}(-2\omega)$ is the Debye-Waller factor for the atom j. This term accounts for the decrease in scattering intensity due to thermal vibration of the reflecting planes. These temperature effects become appreciable at large scattering angle.

$$\exp(-2\omega) = \exp(-2B\sin^2\theta/\lambda^2) \qquad \text{(Woolfson 1970)}$$

2θ = Bragg scattering angle

λ = neutron wavelength .

The magnitude of B increases with temperature from a value of zero and 0K.

Since the neutron possesses a magnetic moment of 1.91 nuclear magnetons, it can interact with the moment on an atom having unpaired electron density. This is the origin of the observed magnetic scattering intensity. $F^M_{hk\ell}$, the magnetic structure factor, closely resembles its nuclear counterpart.

$$F^M_{hk\ell} = \sum_j p_j \exp 2\pi_i (hx_j+ky_j+\ell z_j) \exp(-\omega_j) \ .$$

In this case the neutron scattering length is replaced by the magnetic scattering amplitude p_j.

$$p_j = \frac{e^2\gamma}{2mc^2}\mu_j f_j \qquad \text{(Bacon 1967)} \ .$$

e = electronic charge, γ = neutron magnetic moment, m = neutron mass, c = velocity of light, μ_j = magnetic moment on atom j and f_j = magnetic form factor. The magnetic intensity is proportional to the square of the magnetic moment. The magnetic form factor f_j is due to the interference of the neutron waves scattered from different regions of the unpaired electron density. This leads to a decrease in the magnetic scattering intensity as the scattering angle increases.

In the compounds studied here, the magnetic intensity becomes negligible above $2\theta = 40°$. The magnetic scattering intensity is the product of $(q_{hk\ell}F^{M}_{hk\ell})^2$.

$$q_{hk\ell} = \hat{r}_{hk\ell}(\hat{r}_{hk\ell}\cdot\hat{K}) - \hat{K}$$

$\hat{r}_{hk\ell}$ = unit vector perpendicular to the reflecting planes

$\hat{K}$ = unit vector parallel to the atomic moment.

The directional information on the magnetic moment is contained in the dot product of $q_{hk\ell}$. Thus both the magnitude and direction of the magnetic moment may be inferred from the magnetic scattering intensity.

Spin Configurations in $RTiO_3$

Each unit cell in the $GdFeO_3$ structure contains four rare earth and four transition metal sites. Assuming the magnitic and crystallographic unit cells to be the same, there are 3 possible spin configurations which would lead to a zero net moment on the rare earth sublattice. The same may be shown for the transition metal sublattice. These antiferromagnetic spin arrangements have been designated G, C and A (Bertaut 1963). The ferromagnetic arrangement has been labelled F.

$$F = S1+S2+S3+S4$$

$$G = S1-S2+S3-S4$$

$$C = S1+S2-S3-S4$$

$$A = S1-S2-S3+S4$$

S_i = spin on atom i .

The atomic positions i are specific for the $GdFeO_3$ structure. These are presented in Table 3.1.

Substituting the above spin arrangements into $F^M_{hk\ell}$, it is found that each of the spin configurations contributes to a specific class of reflections.

F: $h+k = 2n \qquad \ell = 2n$
G: $h+k = 2n+1 \qquad \ell = 2n+1$
C: $h+k = 2n+1 \qquad \ell = 2n$
A: $h+k = 2n \qquad \ell = 2n+1$.

Magnetic moments on the Ti sublattice scatter exclusively into these reflections. Since the Ce ions are slightly removed from special crystallographic positions, the magnetic scattering from the rare earth sublattice is a maximum under the above conditions. Bertaut (1963) has categorized these spin modes based on their transformation properties under the symmetry operations of the space group. Assuming a second order spin Hamiltonian, he has summarized the symmetry allowed spin configurations on each sublattice as well as those expected in the event of a coupling between the rare-earth and transition metal.

Table 3.1

Rare earth and transition metal positions in the $GdFeO_3$ structure

	Ti sublattice		Rare earth sublattice	
atom 1	$(\frac{1}{2},0,0)$		$(1-x,y,\frac{1}{4})$	
atom 2	$(\frac{1}{2},0,\frac{1}{2})$		$(x,1-y,\frac{3}{4})$	
atom 3	$(0,\frac{1}{2},\frac{1}{2})$		$(\frac{1}{2}-x,\frac{1}{2}-y,\frac{3}{4})$	
atom 4	$(0,\frac{1}{2},0)$		$(\frac{1}{2}+x,\frac{1}{2}+y,\frac{1}{4})$	
		$LaTiO_3$	$x = .0051$	$y = .0323$
		$CeTiO_3$	$x = .0071$	$y = .0395$

3.3 Experimental Procedure

Data were collected at the McMaster Nuclear Reactor using the triple axis spectrometer in the double axis mode. The samples were polycrystalline powders, loosely packed in a cylindrical thin-walled vanadium sample holder. The neutron wavelength was 1.40 Å. The sample temperature was maintained by means of a displex helium refrigerator and monitored using a gold - .07% iron vs. chromel thermocouple. Diffraction data were accumulated on a position sensitive detector in the angular range $2\theta = 8° - 42°$. Due to the small magnitude of the moments observed, the duration of the data collection was about 140 hours at each temperature.

3.4 Data Treatment

The nuclear contribution to the scattered intensity was derived from the diffraction pattern collected above T_c. Nuclear intensities were calculated using the crystallographic data of MacLean et al. (1979). The atomic positions for $LaTiO_3$ were taken directly and those for $CeTiO_3$ were interpolated between the values reported for $LaTiO_3$ and $NdTiO_3$. The neutron scattering lengths were taken from Bacon (1967). Intensities were corrected for Lorentz effects. A scale factor, SF, was calculated in order to normalize the calculated and observed intensities.

$$SF = \frac{\sum_i \sigma_i \; I_i^c/I_c^o}{\sum_i \sigma_i} \; .$$

I_i^c = calculated intensity of reflection i

I_c^o = observed intensity of reflection i

σ_i = standard deviation of I_i^o .

Exceptionally poor agreement was observed between $I^{obs}_{(101,011)}$ and $I^{calc}_{(101,011)}$ for both $LaTiO_3$ and $CeTiO_3$, most likely due to second order diffraction effects from the intense (202,022) multiplet . ($I^{calc}_{(202,022)}/I^{calc}_{(101,011)} \approx 10^3$). Data collected on finely divided copper powder yielded a second order contribution from the (111) reflection of (.018) $I^{obs}_{(111)}$. This should be compared to $(I^{obs}_{(101,011)}-I^{calc}_{(101,011)})LaTiO_3$ of (.012) $I^{obs}_{(202,022)}$ and $(I^{obs}_{(101,011)}-I^{calc}_{(101,011)})$ $CeTiO_3$ of (.014)$I^{obs}_{(202,022)}$.

The additional Bragg intensity which developed below T_c was attributed to magnetic scattering and thermal effects. Isotropic Debye-Waller factors were estimated from the X-ray temperature factors reported by MacLean et al. (1979) (Appendix II).

The results for $LaTiO_3$ are shown in Table 3.2. Within experimental error, these estimated values compare well with those observed. At high angle, the temperature effects are calculated to be as much as 6% of the total intensity. Unfortunately, this is of the same magnitude as the predicted enhancement due to magnetic scattering. As a result, most confidence is

Table 3.2

Observed and calculated temperature effects for $LaTiO_3$

	$(I_{10K}-I_{152K})^{(a)}$ observed	$(I_{10K}-I_{152K})^{(a),(b)}$ calculated
(011,101)$^{(c)}$	43%(6σ)	0
(121,21$\bar{1}$,013,103)$^{(c)}$	5%(6σ)	4%
(111)	-3%(.5σ)	2%
(120,210)	2%(1σ)	4%
(122,212)	3%(1σ)	5%
(110,002)	.5%(.6σ)	0
(020,200,112)	-6%(.5σ)	5%
(022,202)	4%(11σ)	4%
(220,004)	3%(2.5σ)	6%

(a) expressed as % enhancement of intensity at 152K, statistical reliability is given in brackets

(b) using values of B in Appendix II

(c) magnetically enhanced reflections

placed on low angle reflections where temperature effects are negligible ($2\theta < 23°$).

Further complicating matters is the scattering due to the aluminum can of the displex refrigerator. Fig. 3.1 shows the spectrum of the aluminum can compared to that of $LaTiO_3$. From Table 3.8 it can be seen that all $CeTiO_3$ reflections which overlap aluminum peaks have intensities significantly larger than those calculated using any of the proposed models. Since a large uncertainty would be introduced into the weak magnetic enhancements by subtracting out the aluminum reflections, no attempt was made to correct for this effect. These overlapping peaks were not used in the subsequent refinements.

For both $LaTiO_3$ and $CeTiO_3$, the orthorhombic a and b axes are almost identical. Consequently, reflections of the form $(hk\ell)$ and $(kh\ell)$ are not resolved and the calculations are virtually insensitive to interchange of the x and y axes.

The magnetic form factor for Ti^{3+} was taken from Freeman and Watson (1961) and that for Ce^{3+} was derived from calculations of Stassis et al. (1977). The goodness of fit of the observed data to the proposed magnetic structures is reported using the following R factor.

$$R = \frac{\sum_i \omega_i |I_i^{obs} - I_i^{calc}|}{\sum_i \omega_i I_i^{Q}}$$

ω_i = the weighting factor of reflection i

$$= \frac{1}{\sigma_i^2}.$$

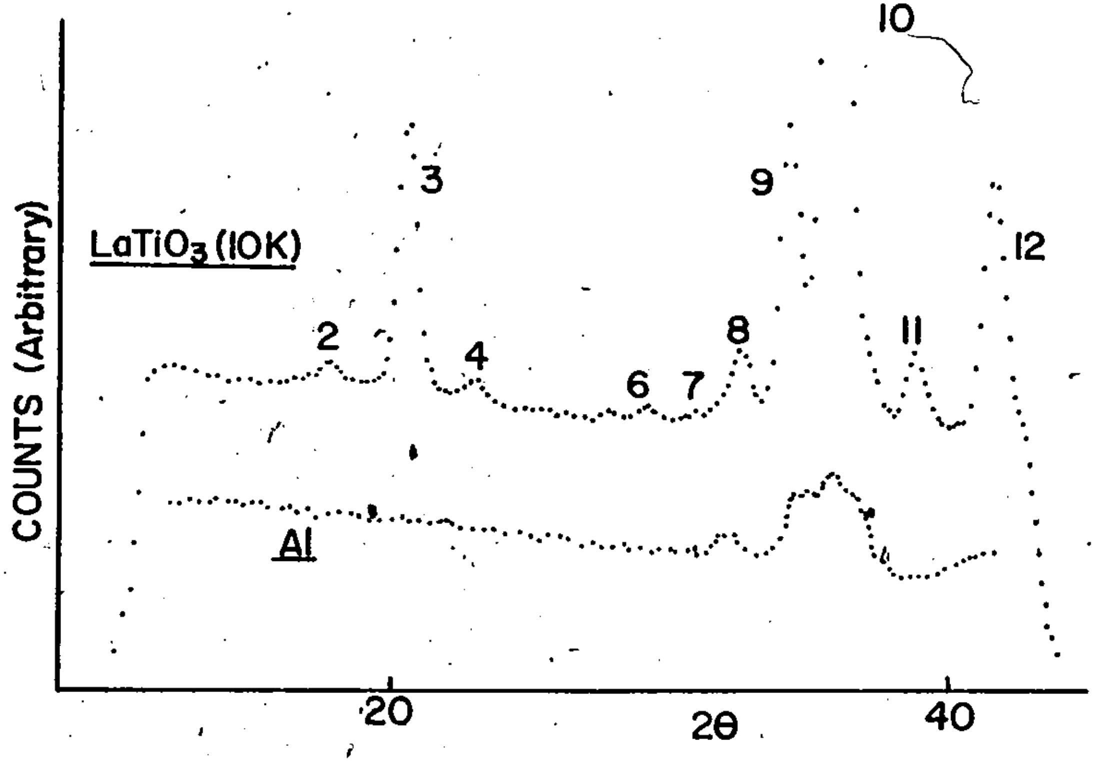

Fig. 3.1 Diffraction pattern of $LaTiO_3$ at 10K and that of the empty experimental apparatus, The reflections 2-12 are identified in the following key.

KEY TO FIGURES 3.1 AND 3.4

Peak No.	
1	(010,100)
2	(101,011)
3	(110,002)
4	(111)
5	(102,012)
6	(020,200,112)
7	(201,003,021)
8	(120,210)
9	(121,211,013,103)
10	(202,022)
11	(122,212)
12	(220,004)

The standard deviation of the magnetic moments is defined as the change in magnitude necessary to double the value of R.

3.5 Results and Discussion

3.5.1 $LaTiO_3$

Recalling the bulk magnetization data which indicate a critical temperature near 125K, data were collected at 10K and 152K. The diffraction pattern observed at 152K is consistent with the X-ray structure of MacLean et al. (1979). No new diffraction peaks appeared at 10K. After correction for temperature effects, the only intensity enhancements greater than three standard deviations were observed for the (011,101) and (121,211;013,103) reflections, characteristic of a G-type antiferromagnetic ordering (Table 3.3, Fig. 3.2). The latter reflection overlaps an aluminum peak and is considered unreliable. The magnitude of the Ti^{3+} moment is based solely on the (011,101) magnetic intensity, assuming a G-type antiferromagnetic array. The calculated magnetic intensities do not vary significantly with moment direction. The magnitude of the Ti^{3+} moment at 10K is estimated to be .45(5) μ_B (Table 3.6). This value is significantly smaller than the .84(1) μ_B reported for $YTiO_3$ at 4.2K (Garrett et al. 1981).

Magnetization measurements (MacLean and Greedan 1981) imply a ferromagnetic component of 7×10^{-3} μ_B/FU at 4.2K. The detection of such a small moment is beyond the scope of this experiment. Thus these two techniques indicate that the Ti^{3+}

moments order in a G-type ferromagnetic array with a small ferromagnetic component (Fig. 3.3). The value of the saturation moment reported by MacLean and Greedan (1981) implies a canting angle of less than 1°. This is consistent with the results reported for the isostructural orthochromites and orthoferrites. In these ordered materials, the transition metal adopts either a G_y ~~G_z~~ F_x or G_xF_z spin configuration (Hornreich 1978). Such a spin arrangement is in agreement with the magnetic properties of the La-rich members of the solid solutions $La_xY_{1-x}TiO_3$ and $La_xGd_{1-x}TiO_3$ to be discussed in a later chapter.

3.5.2 $CeTiO_3$

Diffraction data were collected at 148K, 81K and 10K. No new peaks appeared in the diffraction pattern on cooling to 81K although significant (> 3 σ) magnetic enhancement was observed for the G-type and F-type reflections (Table 3.4). This is in contrast to $LaTiO_3$ where only G-type ordering was observable by neutron diffraction. In analogy with $LaTiO_3$, the critical temperature at 116K was attributed to magnetic ordering within the Ti^{3+} sublattice. There are at least two different ways to rationalize the data at 81K.

(i) One approach is to assign all magnetic intensity to the Ti^{3+} sublattice alone. Models assuming F_xG_z and G_xF_z spin configurations on Ti^{3+} were compared to the observed intensities. Due to the overlap of the reflections, the calculated intensities are insensitive to

Table 3.3

LaTiO$_3$ neutron intensity data at 10K and 152K

	Intensities$^{(a)}$ (counts)		$I_{10K}-I_{152K}$$^{(a)}$		Observed Magnetic Intensity
	10K	152K	Counts	Enhancement$^{(b)}$	
G					
(011,101)	54,979 (2,025)	38,400 (2,025)	16,579 (2,864)	+43% (6σ)	16,579 (2,864)
(121,211,013,103)$^{(c)}$	726,171 (3,538)	694,343 (3,536)	31,828 (5,002)	+5% (6σ)	4,054 (637)
A					
(111)	37,744 (2,019)	39,007 (2,023)	-1,263 (2,858)	-3% (.5σ)	
C					
(120,210)$^{(c)}$	182,975 (3,461)	178,720 (3,463)	4,255 (4,896)	+2% (1σ)	
(122,212)$^{(c)}$	156,009 (3,159)	151,483 (3,161)	4,526 (4,469)	+3% (1σ)	
F					
(110,002)	548,688 (3,107)	546,099 (3,111)	2,589 (4,397)	+.5% (.5σ)	
(020,200,112)	36,319 (3,141)	38,508 (3,143)	-2,189 (4,443)	-6% (.5σ)	
(022,202)$^{(c)}$	3,190,175 (6,968)	3,083,222 (6,963)	106,953 (9,851)	+4% (11σ)	
(220,004)	659,725 (5,298)	640,456 (5,299)	19,269 (7,493)	+3% (2.5σ)	

Table 3.3 (continued)

(a) standard deviation given in brackets

(b) expressed as a % increase of the intensity at 152K

(c) overlapping aluminum reflections

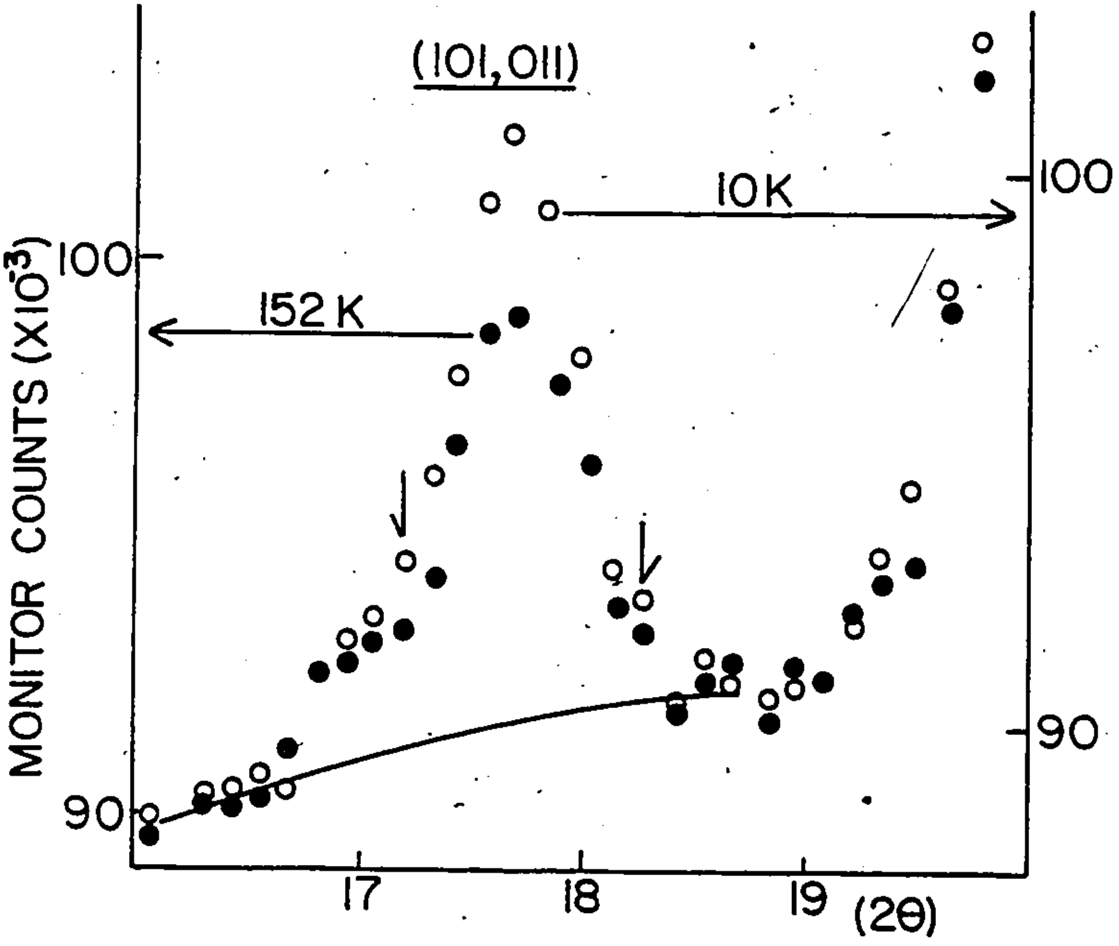

Fig. 3.2 The (101,011) reflection of $LaTiO_3$ at 10K and 152K.

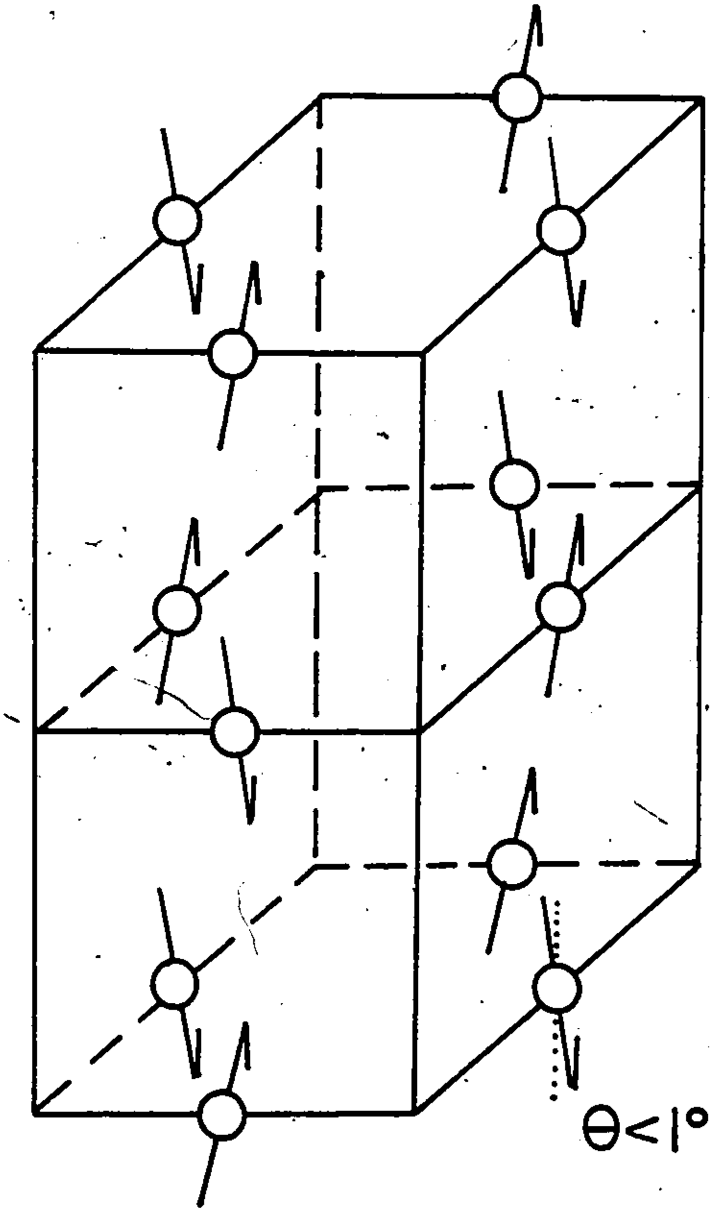

Fig. 3.3 The proposed magnetic structure of $LaTiO_3$ at 10K. The ferromagnetic canting angle is estimated at less than one degree.

Table 3.4

CeTiO$_3$ neutron intensity data at 81K and 148K

	81K	148K	$I_{81K}-I_{148K}$ (a)		Temperature Effects$^{(a)}$	Observed Magnetic Intensity
			Counts	Enhancement		
<u>G</u>						
(011,101)	65,817 (1,926)	51,748 (1,923)	14,069 (2,724)	+24% (5σ)	0	14,069 (2,724)
(121,211,013,103)$^{(b)}$	1,297,909 (2,308)	1,258,667 (2,301)	39,242 (3,258)	+3% (12σ)	+2.5%	6,540 (543)
<u>A</u>						
(111)	23,145 (1,585)	21,436 (1,587)	1,709 (2,243)	+8% (.7σ)	0	
<u>C</u>						
(010,100)	2,620 (4,346)	2,200 (4,345)	420 (6,145)	+19% (.1σ)	0	
(012,102)	1,517 (1,723)	300 (1,723)	1,217 (2,437)	+400% (.6σ)	0	
(120,210)$^{(b)}$	325,190 (1,943)	327,648 (1,945)	-2,458 (2,751)	-7% (.9σ)	+2%	
(122,212)$^{(b)}$	258,402 (2,091)	263,234 (2,092)	4,832 (2,957)	-2% (1.6σ)	+3%	
<u>F</u>						
(110,002)	294,105 (2,410)	279,387 (2,407)	14,718 (3,407)	+5% (4σ)	0	14,718 (3,407)
(020,200,112)	418,857 (2,409)	389,956 (2,404)	28,901 (3,405)	+7.4% (8σ)	+1.5%	23,043 (2,713)
(022,202)$^{(b)}$	3,676,769 (3,108)	3,659,746 (3,102)	17,023 (4,391)	+4.6% (4σ)	+ 2%	9,622 (2,459)

(a) expressed as % increase of the intensity at 148K (b) overlapping aluminum reflections the interchange of the x, y, and z axes. The best consistency between the F-type and G-type reflections was obtained for an F component of .832 (total moment) and a G component of .555 (total moment) (Table 3.7). This corresponds to a strikingly large ferromagnetic canting angle of 34°. The magnitude of the Ti^{3+} moment at 81K is estimated at .6(1) μ_B.

(ii) An alternative interpretation of these data may also be considered. The canting angle of 34° is an order of magnitude larger than that observed for the transition metal sublattice in the $RCrO_3$ and $RFeO_3$ compounds (Goodenough and Longo 1970, Hornreich 1978). It is possible that the Ti^{3+} sublattice orders in a G-type antiferromagnetic arrangement and induces a ferromagnetic moment on Ce^{3+}. Consistent with the symmetry arguments of Bertaut (1963), the data were analyzed assuming $G_x(Ti^{3+})F_z(Ce^{3+})$ and $G_z(Ti^{3+})F_x(Ce^{3+})$ spin configurations. The resultant R value is comparable to that obtained assuming that all the magnetic scattering intensity is due to ordering within the Ti^{3+} sublattice (Table 3.7). The neutron data are not able to distinguish between these two possibilities.

At 10K, all reflections display magnetic enhancement (Fig. 3.4, Table 3.5). Recall that the magnetization-temperature data of MacLean and Greedan (1981) exhibit unusual curvature

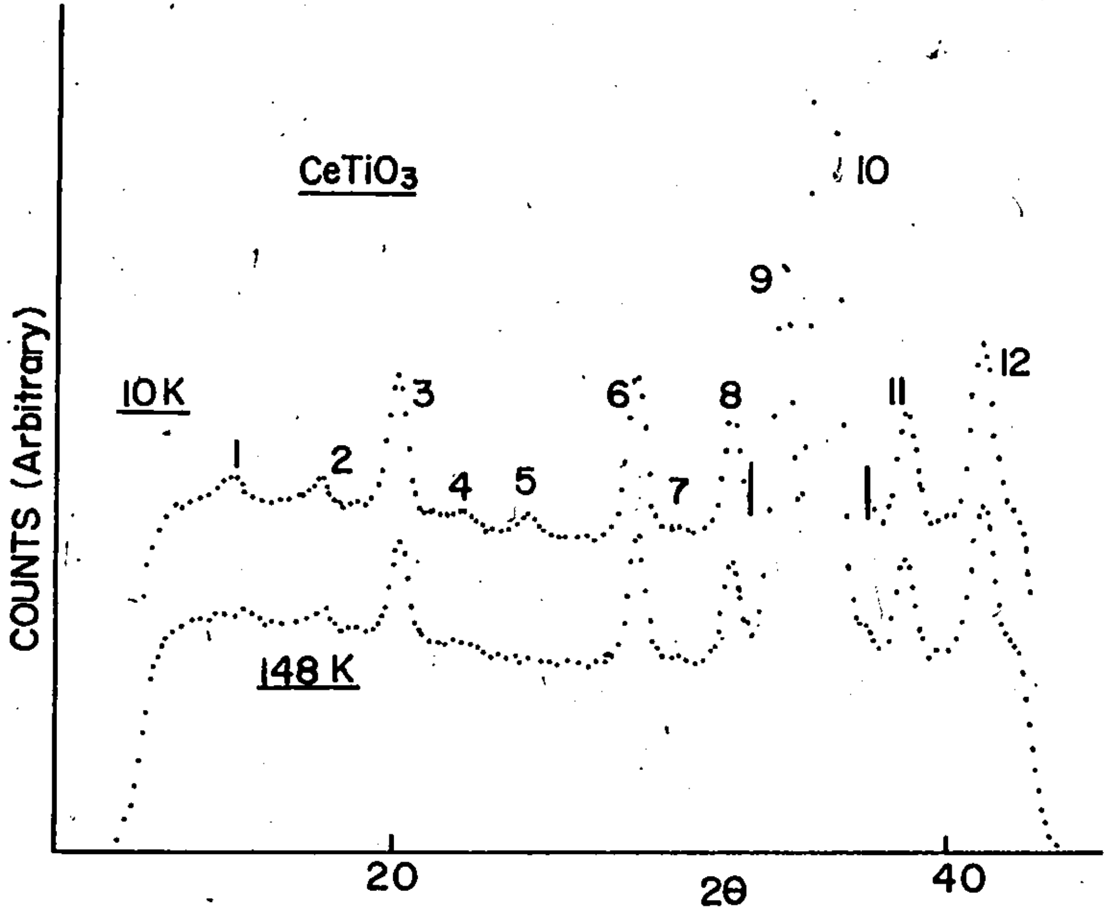

Fig. 3.4 The diffraction patterns of $CeTiO_3$ at 10K and 148K. The reflections are identified in the key to figure 3.1. Peaks number 9 and 10 of the 10K pattern have been omitted for clarity.

Table 3.5

CeTiO$_3$ neutron intensity data at 10K and 148K

	10K	148K	$I_{10K}-I_{148K}$ (a) Counts	$I_{10K}-I_{148K}$ (a) Enhancement	Temperature Effects(a)	Observed Magnetic Intensity
<u>G</u>						
(011,101)	78,400 (2,024)	51,748 (1,923)	26,652 (2,792)	52% (10σ)	0	26,652 (2,792)
(121,211,013,103)(b)	1,373,630 (2,416)	1,258,667 (2,301)	114,963 (3,336)	9% (34σ)	5%	52,030 (1,485)
<u>A</u>						
(111)	29,043 (1,684)	21,436 (1,587)	7,607 (2,314)	35% (3σ)	1.5%	7,285 (2,215)
<u>C</u>						
(010, 010)	63,602 (6,663)	2,200 (4,345)	61,402 (7,955)	2,800% (7σ)	0	61,402 (7,955)
(012,102)	52,463 (1,828)	300 (1,723)	52,163 (2,512)	17,300% (21σ)	0	52,163 (2,512)
(120,210)(b)	367,203 (2,051)	327,648 (1,945)	39,555 (2,827)	12% (14σ)	4%	26,449 (1,885)
(122,212)(b)	321,334 (2,208)	263,234 (2,092)	58,100 (3,041)	22% (19σ)	6%	42,306 (2,212)
<u>F</u>						
(110,002)	399,157 (2,532)	279,387 (2,407)	119,770 (3,494)	43% (34σ)	0	119,770 (3,494)
(020,200,112)	485,573 (3,440)	389,956 (2,404)	95,617 (4,197)	25% (23σ)	4%	80,019(c) (6,104)
(022,202)(b)	3,853,374 (3,225)	3,659,746 (3,102)	193,628 (4,475)	5% (43σ)	4%	47,238 (1,091)

(a) expressed as % increase of the intensity at 148K, (b) overlapping aluminum reflections
(c) standard error is based on an uncertainty in the temperature effects of .02 (peak intensity)

near 60K. Magnetic ordering of both the Ti^{3+} and Ce^{3+} sublattices is postulated. The enhancement of the A-type reflection is small and can be attributed to the displacement of the Ce atoms from special crystallographic positions. There still remains evidence for F-type, G-type and C-type magnetic ordering at 10K. In light of the proposed structures at 81K, it is necessary to consider two separate models for the magnetic ordering of $CeTiO_3$ at 10K.

(i) One may assume that the Ti^{3+} sublattice exhibits both F-type and C-type components. C-type and F-type magnetic ordering is then assigned to the Ce^{3+} sublattice as reported for the rare earth ions in $DyTiO_3$, $TbTiO_3$ and $HoTiO_3$ (Turner et al. 1981, Turner et al. 1980). Satisfactory agreement between the observed and calculated magnetic intensities is possible assuming either $G_xF_z(Ti^{3+})$ $F_xC_y(Ce^{3+})$ or $F_xG_z(Ti^{3+})C_yF_z(Ce^{3+})$ spin arrangements (Table 3.8, models I,II). The R value varies slightly on interchange of the x and y axes on Ce^{3+}. A Ti^{3+} moment of .7(1) μ_B and a Ce^{3+} moment of 1.35(9) μ_B at 10K are estimated in both cases. Crystal field calculations of Greedan and Seto (1981) on the isostructural $CeScO_3$ predict a ground state Ce^{3+} moment of 1.77 μ_B. Both models I and II in Table 3.8 violate the symmetry rules developed by Bertaut (1963). For the G_xF_z configuration on Ti^{3+} (Table 3.8, model I), Bertaut predicts F_z on Ce^{3+}. No C-type ordering is permitted. For F_xG_z on Ti^{3+} (Table 3.8, model II), an F_xC_y configuration for Ce^{3+} is predicted (Table 3.8, model III). In this case the R value is significantly larger than for the symmetry forbidden arrangement. The symmetry rules developed by Bertaut are not always realized in practice. The Cr^{3+} sublattice in $ErCrO_3$ displays two symmetry disallowed magnetic components (Bertaut and Mareschal 1967). Bertaut himself points out that it may be necessary to consider spin interactions of order greater than two (Bertaut 1963).

(ii) It is also possible that the Ti^{3+} sublattice orders in a G-type arrangement with negligible ferromagnetic component. F-type and C-type ordering are assigned to the Ce^{3+} sublattice. Satisfactory agreement between observed and calculated magnetic intensities is possible assuming G_z on Ti^{3+} and F_xC_y on Ce^{3+} (model IV, Table 3.8). This combination is symmetry allowed. Both configurations belong to the irreducible representation Γ_2 developed by Bertaut (1963). The Ce^{3+} moment of 1.35(15) μ_B is the same as that predicted by models I and II. The Ti^{3+} moment of ,36(10) μ_B is not significantly different from the .45(5) μ_B deduced for $LaTiO_3$ at 10K.

Saturation moments may be calculated for the above models and compared to the measurements of MacLean and Greedan (1981).

At 10K, all three models (Table 3.8, models I, II and IV) predict saturation moments significantly larger than the reported value of .5 μ_B FU^{-1}. Similarly the ferromagnetic components of the Ti^{3+} moment inferred from the neutron data at 81K are larger than the reported value (.2 μ_B FU^{-1}).

Magnetization-field data were collected on the same sample that was used in the neutron diffraction studies. In contrast to the results of MacLean and Greedan (1981), saturation behaviour was not observed up to an applied field of 46 KG (Fig.3.5). The value of .9 μ_B FU^{-1} at 46 KG is not inconsistent with the saturation magnetizations predicted by models I, II and IV in Table 3.8.

The temperature dependence of the (010,100) and (012,102) reflections was examined between 10K and 81K (Figs. 3.6 and 3.7). These are C-type reflections having no nuclear contribution. The total intensity is derived from magnetic ordering within the Ce^{3+} sublattice. Significant magnetic intensity is observed below 60K. Clearly these curves do not resemble Brillouin functions. It is difficult to identify a critical temperature arising from a spontaneous ordering of the Ce^{3+} moments. Mean field coupling constants reported for the phases $RTiO_3$ (R = Gd^{3+}, Tb^{3+}, Dy^{3+}, Ho^{3+}, Er^{3+} and Tm^{3+}) indicate that the rare earth-rare earth interactions are much weaker than the rare earth-titanium interactions (Turner and Greedan 1980). Further discounting the probability of significant Ce-Ce coupling is

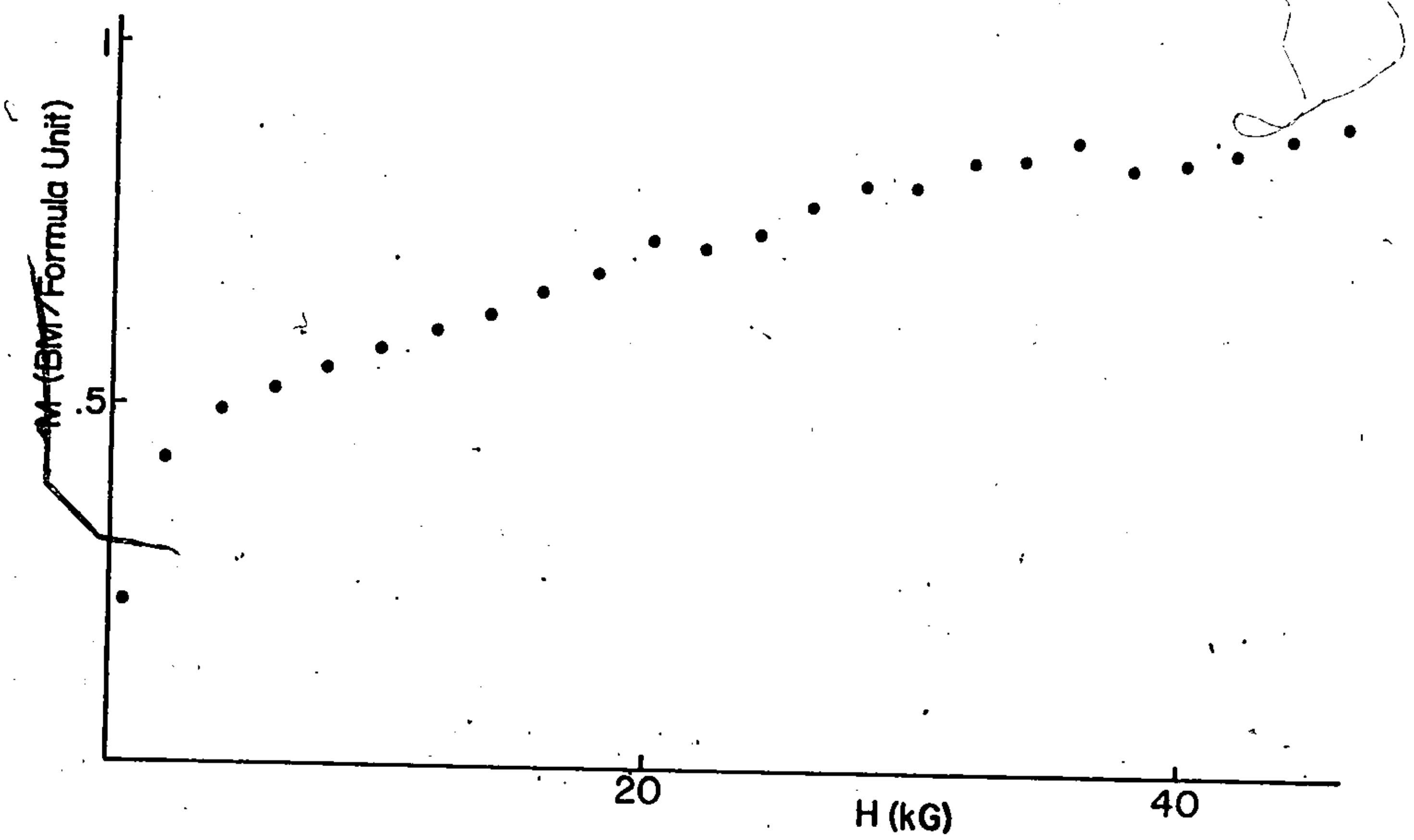

Fig. 3.5 Magnetization vs. field for polycrystalline $CeTiO_3$ at 4.2K.

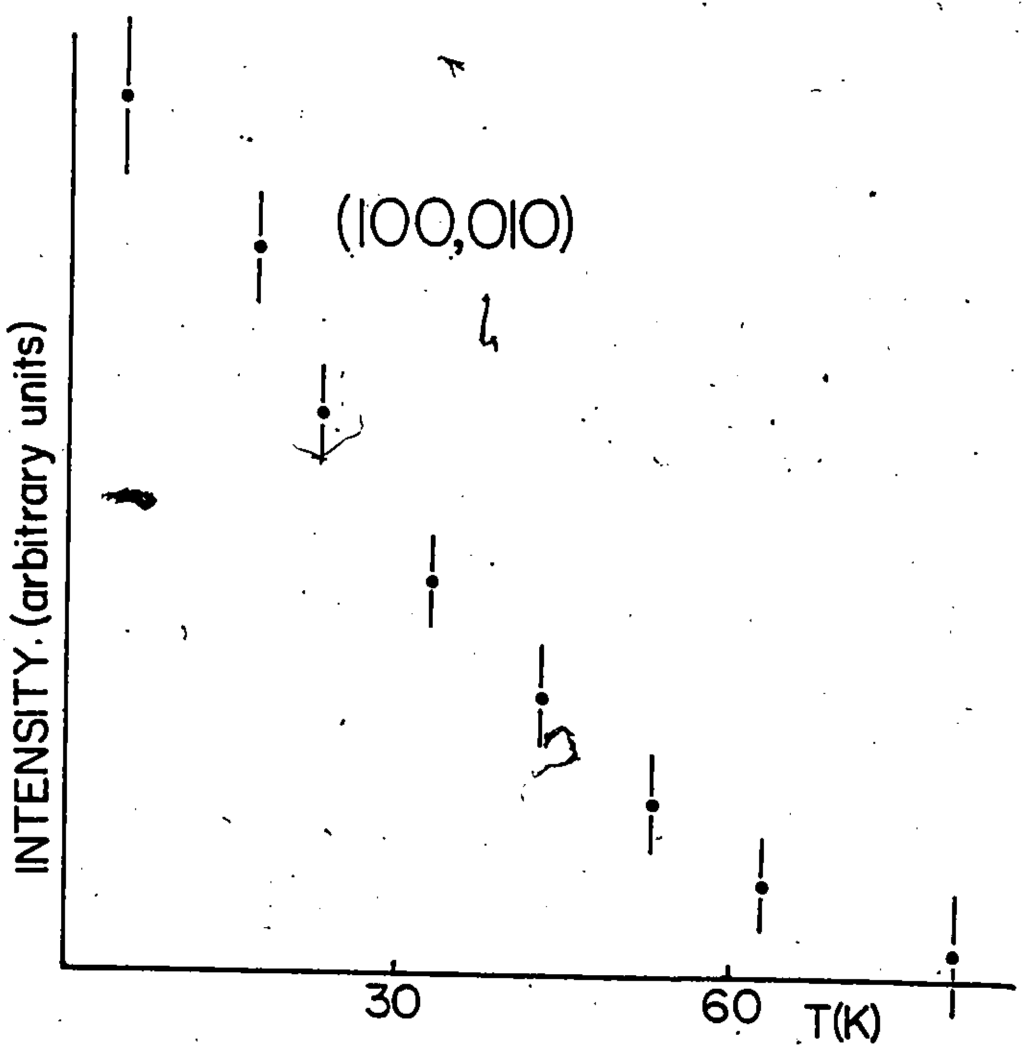

Fig. 3.6 Intensity vs. temperature for the (100,010) reflection of $CeTiO_3$.

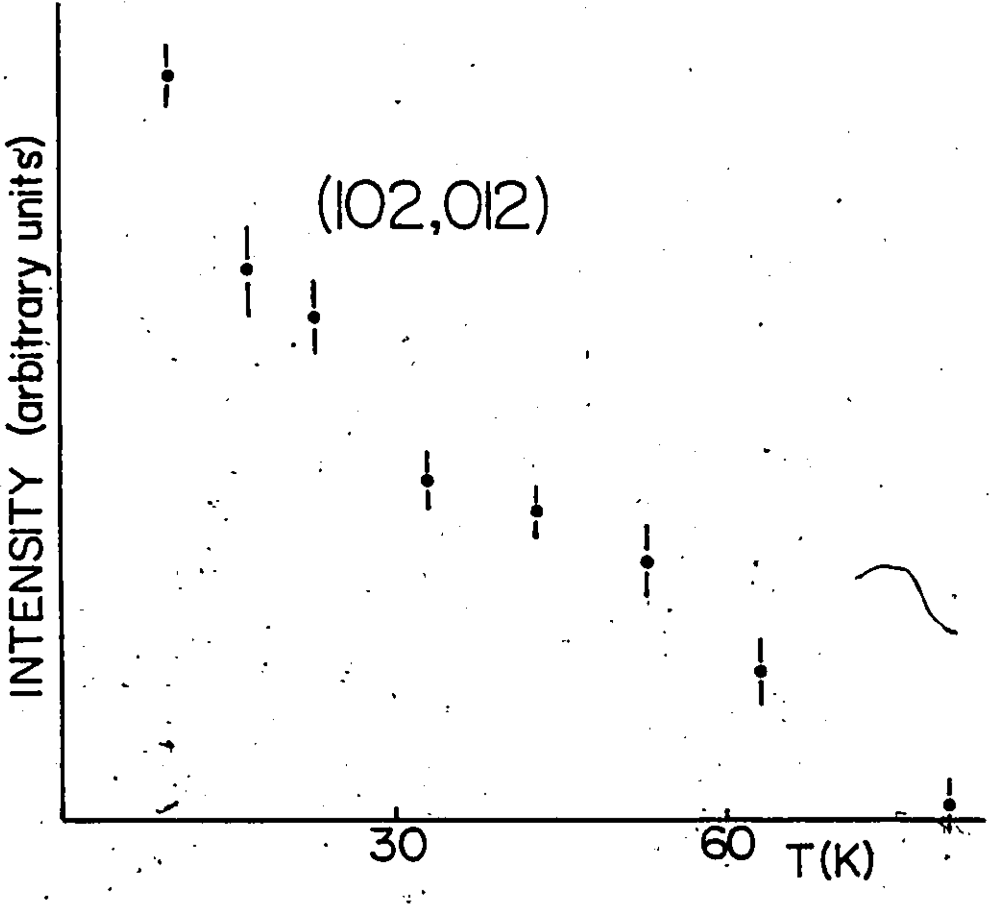

Fig. 3.7 Intensity vs. temperature for the (102,012) reflection of $CeTiO_3$.

the report of paramagnetic behaviour of isostructural $CeScO_3$ down to 4.2K (Greedan and Seto 1981). It is reasonable that the Ce^{3+} moments align in a C-type arrangement via the intense internal magnetic field arising from the Ti^{3+} sublattice. The temperature dependence of the intensity of the (100) magnetic reflection has been reported for the isostructural $HoCrO_3$ (Shamir et al. 1977). At low temperatures these data exhibit the same form as observed for $CeTiO_3$. As in the rare earth orthotitanites, the rare earth-transition metal coupling in $HoCrO_3$ is much stronger than the rare earth-rare earth interactions.

In summary, two models are proposed to describe the ordering in $CeTiO_3$. In both cases the critical temperature of 116K is ascribed to spontaneous ordering of the Ti^{3+} sublattice.

(i) At 81K the Ti^{3+} sublattice is ordered in a G-type antiferromagnetic arrangement with a ferromagnetic canting angle of 34°. The Ti^{3+} moment is estimated at .6(1) μ_B. At this temperature the Ce^{3+} sublattice is not magnetically ordered. At 10K the Ti^{3+} retains G-type and F-type components. The Ce^{3+} sublattice is also magnetically ordered but displays C-type and F-type compounds. The deduced Ti^{3+} and Ce^{3+} moments are .7(1) μ_B and 1.35(9) μ_B respectively. The ferromagnetic components of the Ce^{3+} and Ti^{3+} sublattices lie along perpendicular directions. This model of the ordered state at 10K violates the symmetry relations of Bertaut (1963). It is also necessary to postulate a ferromagnetic canting of the Ti^{3+} moments which is much larger than previously reported for any of the isostructural $RCrO_3$ or $RFeO_3$ compounds.

(ii) At 81K the Ti^{3+} moments are ordered in a G-type arrangement. This induces a ferromagnetic moment on the Ce^{3+} sublattice. The Ti^{3+} and Ce^{3+} moments are estimated at .35(5) μ_B and .4(1) μ_B respectively. At 10K, the Ce^{3+} sublattice displays both C-type and F-type ordering. The Ti^{3+} moments are still ordered in a G-type arrangement. The Ce^{3+} moment is the same as predicted by (i) above while the Ti^{3+} moment is estimated at .36(10) μ_B. This scheme is consistent with the symmetry rules of Bertaut (1963). It is not necessary to postulate an unusually large ferromagnetic canting of the Ti^{3+} moments as in model (i). Also, the value of the Ti^{3+} moment is very close to that deduced for $LaTiO_3$. Unfortunately the neutron data alone are not able to differentiate between models (i) and (ii).

The temperature dependence of the (010,100) and (012,102) magnetic intensities has been investigated. The results imply that the Ce^{3+} moments order in an F-type/C-type arrangement below 60K due to weak coupling with the Ti^{3+} sublattice.

Table 3.6

$LaTiO_3$ (10K) - calculated vs. observed magnetic Intensities

	Observed	Calculated[a]		
		$\mu = .5\mu_B$	$\mu = .45\ \mu_B$	$\mu = .4\mu_B$
(011,101)	21(4)	25	20	17
(021,211,013,103)[b]	5(1)	9	8	7

(a) assuming a G-type antiferromagnet (moment directed along x, y or z)

(b) overlapping aluminum reflection

Table 3.7

$CeTiO_3$ (81K) - calculated vs. observed Magnetic Intensities

	Observed	(I)[a] $\mu = .6(1)\mu_B$ $G = .555\ \mu_B$ $F = .832\ \mu_B$	(II)[a] $\mu = .45\ \mu_B$ $F = G = .707\ \mu_B$	(III)[c] $\mu(Ti^{3+}) = .35\mu_B$ $\mu(Ce^{3+}) = .4(1)\mu_B$
<u>G</u>				
(011,101)	11(2)	11	10	12
(121,211,013,103)[b]	6(3)	4	4	4
<u>F</u>				
(110,002)	11(3)	12	5	10
(020,200,112)	17(4)	8	4	8
(022,202)[b]	7(2)	2	1	3
		$\mu_{sat} = .50\mu_B$ $R = .15$	$\mu_{sat} = .32\mu_B$ $R = .34$	$\mu_{sat} = .4$ $R = .18$

(a) assume F_xG_z, F_yG_z, G_xF_z or G_yF_z on titanium

(b) overlapping aluminum reflections

(c) assume G_x on titanium and F_z on cerium or G_z on titanium and F_x on cerium

Table 3.8

$CeTiO_3$ (10K) - Calculated vs. observed magnetic intensities

	Observed	(I) Ti-.7(1)μ_B G_x(.608)F_z(.794) Ce-.135(9)μ_B F_x(.814)C_y(.581)	(II) Ti-.7(1)μ_B F_x(.832)G_z(.55) Ce-1.35(9)μ_B C_y(.581)F_z(.814)	(III) Ti-.6(3)μ_B F_x(.832)G_z(.555) Ce-1.8(4)μ_B F_x(.894)C_y(.447)	(IV) Ti-.36(10)μ_B G_z Ce-1.35(15)μ_B F_x(.842)C_y(.540)
C					
(010,100)	47(5)	43	43	45	37
(012,102)	40(2)	42	42	44	37
(120,210)$^{(a)}$	20(2)	12	13	13	11
(122,212)$^{(a)}$	32(3)	21	21	21	18
G					
(011,101)	20(2)	19	17	19	20
(121,211,013,103)$^{(a)}$	39(3)	11	6	7	6
A					
(111)	6(2)	5	6	11	6
F					
(110,002)	91(3)	93	89	88	83
(020,200,112)	61(8)	76	75	220	70
(022,202)$^{(a)}$	36(4)	28	29	32	26
(a) overlapping aluminum reflection		μ_{sat}=1.2(1)μ_B R = .06	μ_{sat}=1.2(1)μ_B R = .06	μ_{sat}=2.1(3)μ_B R = .21	μ_{sat}=1.1(1)μ_B R = .07

CHAPTER 4

THE MAGNETIC AND TRANSPORT PROPERTIES OF THE $La_xY_{1-x}TiO_3$ SOLID SOLUTIONS

4.1 Introduction

The physical properties of $LaTiO_3$ and $YTiO_3$ are strikingly different. Above 125K, both the magnetic susceptibility and electrical resistivity reported for $LaTiO_3$ are consistent with itinerant electron behaviour (MacLean and Greedan 1981). Below 125K, the electrical resistivity increases as the temperature drops, characteristic of an activated transport mechanism (Fig. 4.1). The magnetic susceptibility increases sharply below this temperature indicating the onset of magnetic ordering. One explanation of these data is a metal-semiconductor transition at 125K. Recall also that neutron diffraction data presented in chapter 3 confirm an antiferromagnetic arrangement of the Ti^{3+} lattice in $LaTiO_3$ at 10K.

The resistivity curve of $YTiO_3$ is characteristic of an activated transport mechanism (Bazuev and Shveiken 1978). This compound appears to order ferromagnetically below 29K (Greedan and MacLean 1978). A saturation moment of .84 μ_B/Ti^{3+} ion at 4.2K has been reported for a single crystal sample (Garrett et al. 1981). Above T_c, the susceptibility is of the Curie-Weiss type.

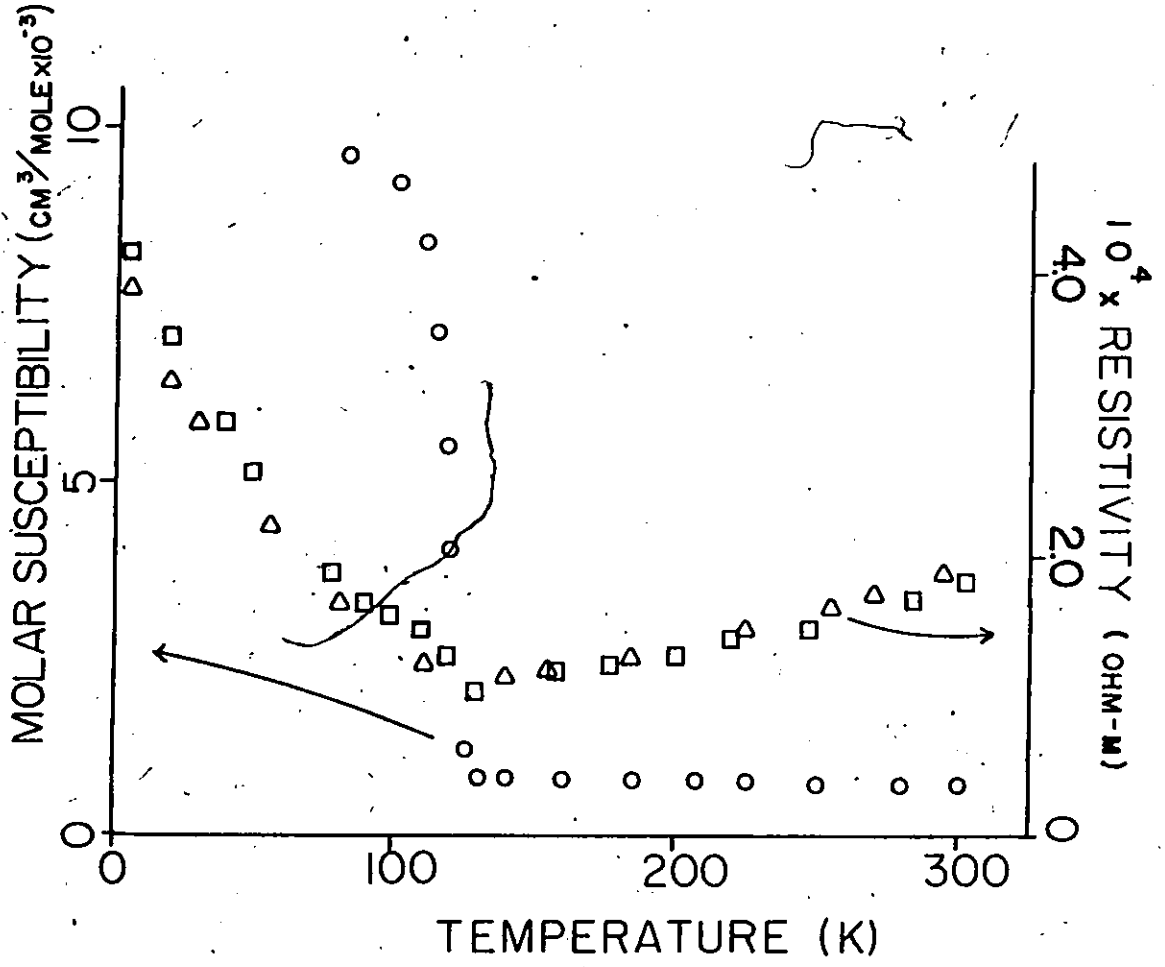

Fig. 4.1 Magnetic susceptibility vs. temperature and electrical resistivity vs. temperature for $LaTiO_3$ (from MacLean and Greedan 1981).

The Curie constant of .35 cm^3 K $mole^{-1}$ is extremely close to the spin only d^1 value of .37 (Johnston 1975). These data are characteristic of localized electron behaviour. Both La^{3+} and Y^{3+} have closed shell configurations, thus the observed magnetic and electronic properties may be attributed to the $3d^1$ electron on Ti^{3+}.

Recall that since there are no short Ti-Ti contacts, the exchange pathway between the Ti^{3+} ions includes an intervening oxide ion. Also overlap of the Ti dπ orbitals with the pπ orbitals on oxygen is maximized when the Ti-O-Ti bond angle is 180°. Recall that a metal-semiconductor transition in these materials has been predicted as this bond angle decreases from 180° and the dπ-pπ-dπ overlap becomes less favourable (Fig. 1.4). The Ti-O-Ti bond angle is 157° in $LaTiO_3$, compared to 142° in $YTiO_3$. Resistivity data reported for the $RTiO_3$ series (R = $Lanthanide^{3+}$) are consistent with a transition between itinerant and localized electron behaviour occuring between $CeTiO_3$ and $PrTiO_3$ (MacLean and Greedan 1981, MacLean et al. 1981). Based on the size of the rare earth ion, the Ti-O-Ti bond angles in these materials are expected to fall between those of $LaTiO_3$ and $YTiO_3$.

In the heavy rare-earth titanites $RTiO_3$ (R = Tb^{3+} to Yb^{3+}) the Ti^{3+} sublattice orders ferromagnetically (Turner et al. 1981, Turner et al. 1980). In contrast, the Ti^{3+}-Ti^{3+} exchange interactions in $LaTiO_3$ are predominantly antiferromagnetic. (The ferromagnetic canting angle is less than 1°.) One interpretation of the neutron scattering data for $CeTiO_3$ suggests that the ordered Ti^{3+} sublattice possesses appreciable ferromagnetic and antiferromagnetic components. The rare earth radius (and presumably the Ti-O-Ti bond angle) in $CeTiO_3$ is intermediate to those of $LaTiO_3$ and $YTiO_3$.

Goodenough (1966) has argued that the magnetic and transport properties of the rare earth titanite series are dominated by the $3d^1$ electron on Ti^{3+}. Further, he has suggested that these properties may be adjusted structurally through manipulation of the Ti-O-Ti bond angle. Solid solutions of the form $La_xY_{1-x}TiO_3$ (x = .3 - 1.0) were prepared to investigate this prediction. Results will be taken from the work of Greedan and MacLean (1978) on the compositions $La_xY_{1-x}TiO_3$ (x = 0 - .2).

4.2 Experimental Method

Magnetic data for both the $La_xY_{1-x}TiO_3$ and $La_xGd_{1-x}TiO_3$ solid solutions were collected on a PAR vibrating sample magnetometer using pressed polycrystalline pellets weighing about 300 mg. The system was calibrated by means of a high purity nickel standard. Temperature was monitored through a gold -.07% iron vs. chromel thermocouple. D.C. resistivity measurements were undertaken on single crystal samples of $La_{.1}Y_{.9}TiO_3$ and $La_{.2}Y_{.8}TiO_3$ in the temperature range 225 - 300K using the van der Pauw technique (van der Pauw 1958). The experimental apparatus and procedure were identical to those described by MacLean (1980).

4.3 Results and Discussion

On the basis of magnetization data collected in the range 4K - 300K one can separate the solid solutions into four distinct classes.

(I) The magnetization temperature curves of $La_{.95}Y_{.05}TiO_3$ and $La_{.9}Y_{.1}TiO_3$ closely resemble that of $LaTiO_3$ (Fig. 4.2). These data are characterized by a single sharp drop in the magnetization near 120K. A canted antiferromagnetic structure analogous to that of $LaTiO_3$ is postulated for all three of these compounds. The critical temperature, T_c, has been estimated by a linear extrapolation of M^2 vs T. T_c drops with increasing Y composition, suggesting a weakening of the antiferromagnetic exchange interactions as the effective size of the rare earth ion decreases (Table 4.1).

(II) In contrast to the class (I) compounds, the magnetization-temperature data of the phases $La_{.8}Y_{.2}TiO_3$ - $La_{.6}Y_{.4}TiO_3$ do not resemble Brillouin functions. The initial steep drop in the magnetization at 4K gives way to a region of slightly convex curvature in the region of 80K. At higher temperatures, the magnetization becomes almost temperature independent (Fig. 4.3). T_c corresponds to this point at which the magnetization decreases to a small, nearly constant value. This was verified by the disappearance of hysteresis in magnetization-temperature curves obtained above T_c. In these phases, T_c decreases with increasing Y content, indicating

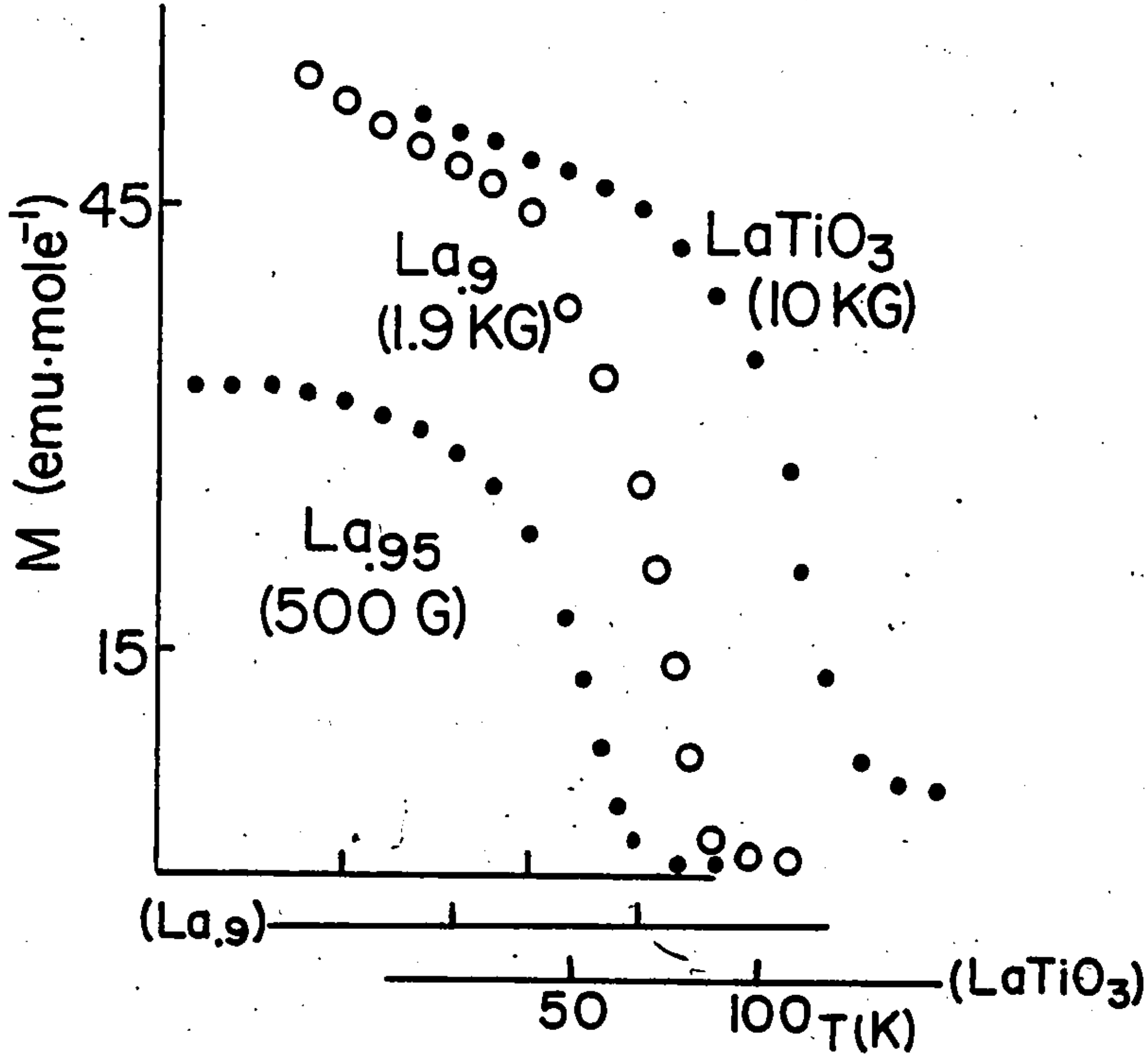

Fig. 4.2 Magnetization vs. temperature for LaTiO$_3$, La$_{.95}$Y$_{.05}$TiO$_3$ and La$_{.9}$Y$_{.1}$TiO$_3$. The applied field is given in brackets.

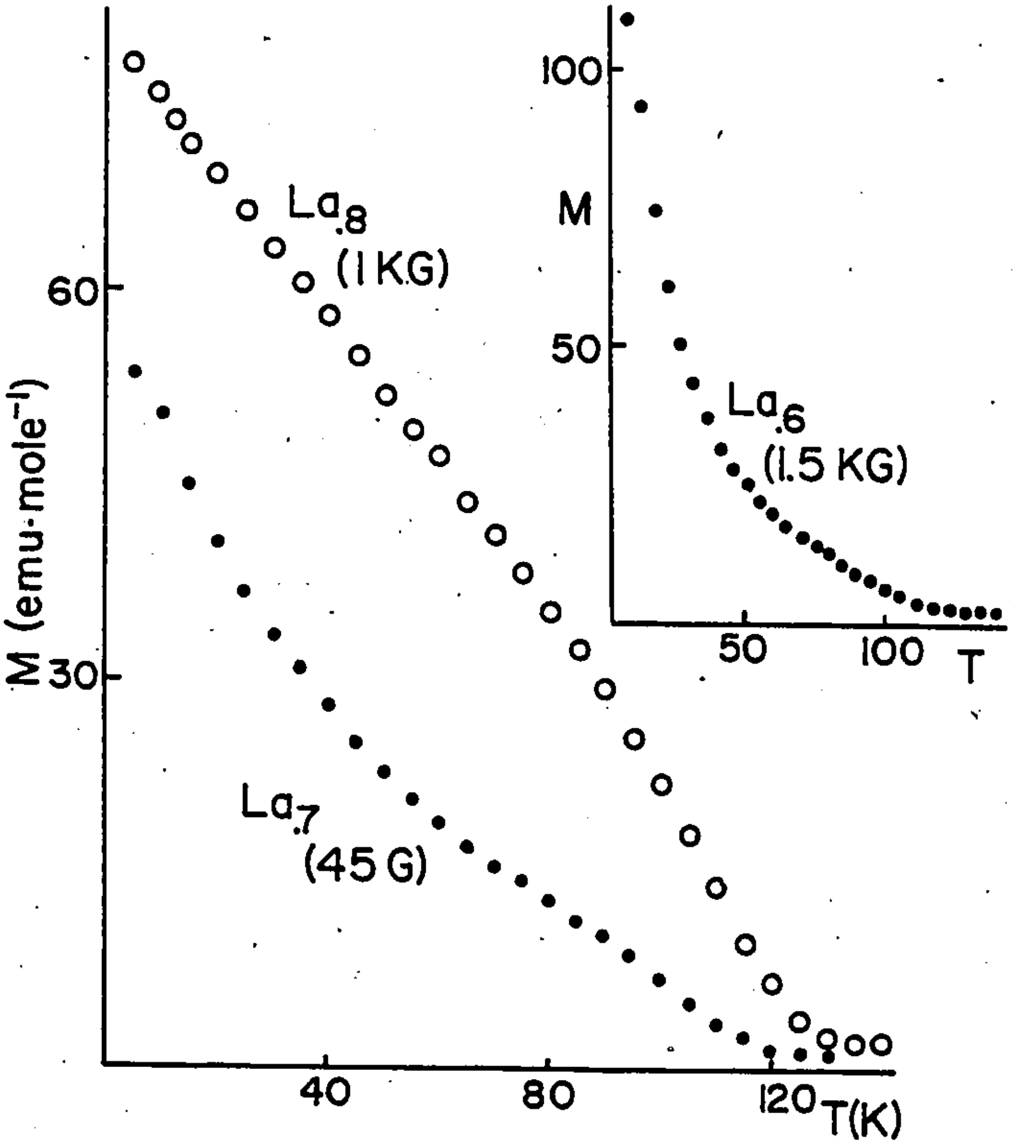

Fig. 4.3 Magnetization vs. temperature for $La_{.8}Y_{.2}TiO_3$ $La_{.7}Y_{.3}TiO_3$ and $La_{.6}Y_{.4}TiO_3$. The applied field is given in brackets.

a further weakening of the antiferromagnetic Ti-Ti exchange interactions. Note however that the values of T_c for both $La_{.8}Y_{.2}TiO_3$ and $La_{.7}Y_{.3}TiO_3$ are higher than that of the 90% La compound. This may imply that the type of magnetic ordering present in the group (II) compounds is more complex than the canted antiferromagnetic structure assumed for the group (I) phases. The small magnitude of the magnetization observed for the group (II) materials implies that the exchange interactions are predominantly antiferromagnetic.

(III) For both $La_{.5}Y_{.5}TiO_3$ and $La_{.4}Y_{.6}TiO_3$, the magnetization drops sharply and smoothly near 12K (Fig. 4.4). At first sight there is no evidence of magnetic ordering down to 4.2K. However hysteresis effects indicate critical temperatures greater than 40K. In these phases, T_c was estimated by a systematic search for hysteresis in the magnetization-temperature curves at various temperatures. The data for $La_{.5}Y_{.5}TiO_3$ are shown in Fig.4.5. The magnitude of the zero field remanence decreases with increasing temperature as expected. (The positive intercept on the M axis is due to the uncertainty in the zero of the apparatus.) This behaviour implies the existence of a small ferromagnetic component in the magnetically ordered state. Surprisingly, no anomaly in the magnetization-temperature curve is observed in the region of T_c (Fig.

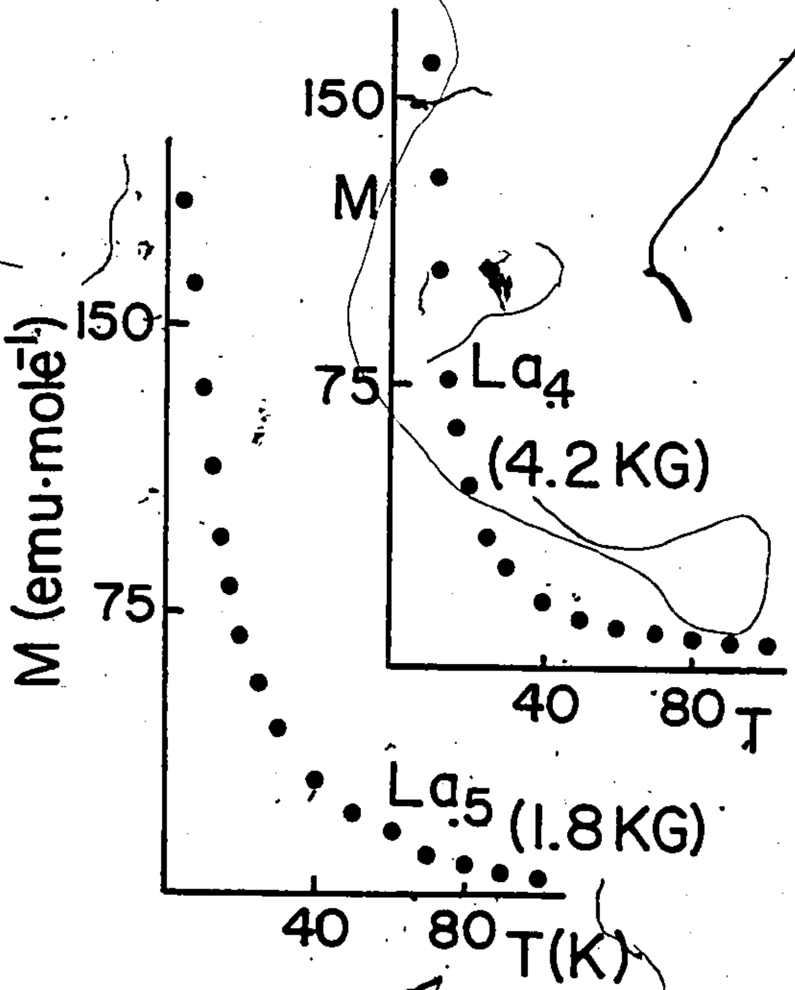

Fig. 4.4 Magnetization vs. temperature for $La_{.5}Y_{.5}TiO_3$ and $La_{.4}Y_{.6}TiO_3$. The applied field is given in brackets.

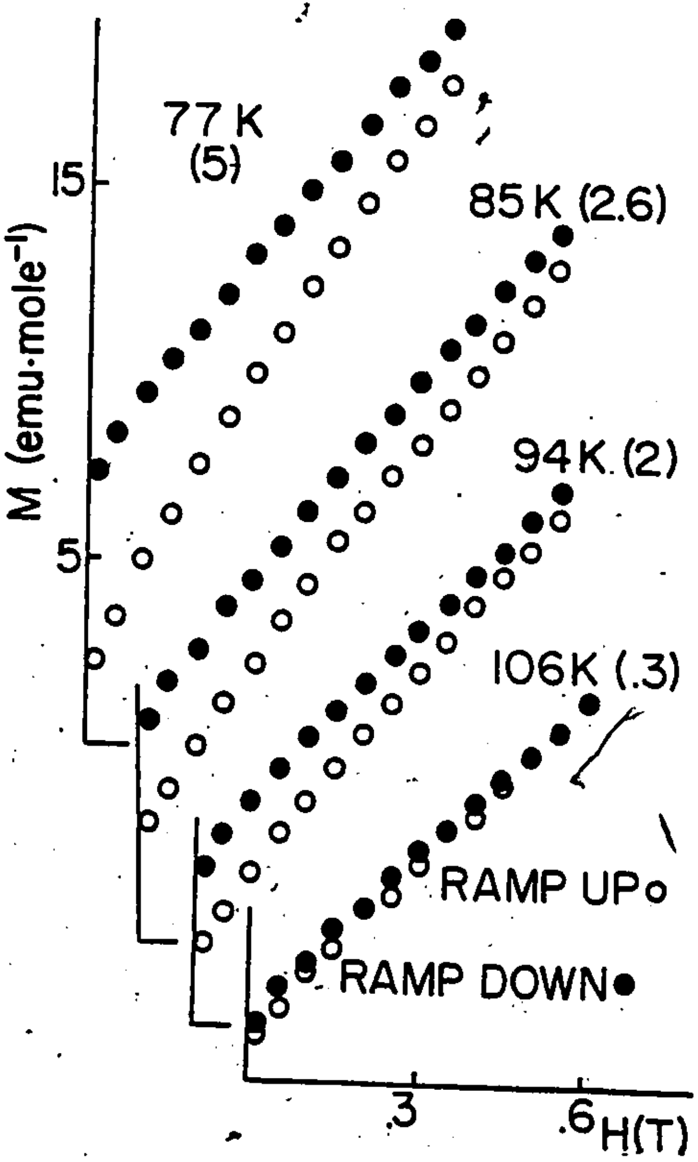

Fig. 4.5 Magnetic hysteresis measurements for $La_{.5}Y_{.5}TiO_3$ at various temperatures. The magnitude of the zero field remanence (emu/mole) is given in brackets.

4.6) As is the case in the group (I) and (II) compounds, T_c decreases with increasing Y composition.

(IV) The phases $La_{.3}Y_{.7}TiO_3$-$La_{.05}Y_{.95}TiO_3$ appear closely related to $YTiO_3$. As in the group (I) compounds, the magnetization-temperature curves are all Brillouin-like, although the magnitude of the observed moments points to predominantly ferromagnetic exchange interactions (Fig. 4.7). T_c was determined by linear extrapolation of M^2 vs T. Unlike the other members of the series, the critical temperature decreases as the La content grows. This suggests that the ferromagnetic exchange interactions are weakened as the effective size of the rare earth ion increases.

Some general comments may be made from the above discussion. The magnetic behaviour in this system is best understood for the extreme composition ranges. At the La-rich end of the series ($LaTiO_3$-$La_{.9}Y_{.1}TiO_3$) the exchange is mainly antiferromagnetic. As the effective rare earth size decreases, the strength of the exchange interactions diminishes. At the other end of the series ($YTiO_3$-$La_{.3}Y_{.7}TiO_3$) the exchange interactions are ferromagnetic. In these phases the exchange forces are weakened as the La content increases. For the intermediate compositions ($La_{.8}Y_{.2}TiO_3$-$La_{.4}Y_{.6}TiO_3$) the magnetic properties are complex and not understood.

Although the details of the magnetic ordering in the intermediate phases are as yet unclear, it appears that the nature of the Ti-Ti exchange interactions in the $La_xY_{1-x}TiO_3$ system may

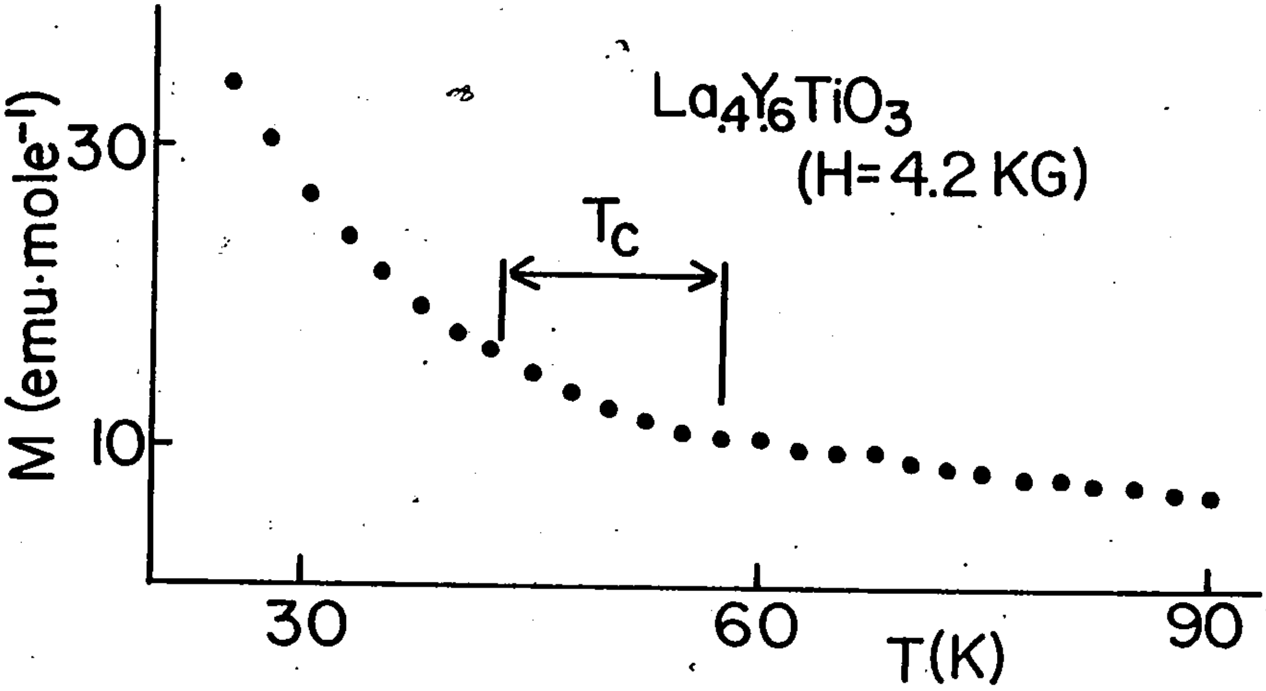

Fig. 4.6 Magnetization vs. temperature for $La_{.4}Y_{.6}TiO_3$. Note the smooth curvature in the region of T_c.

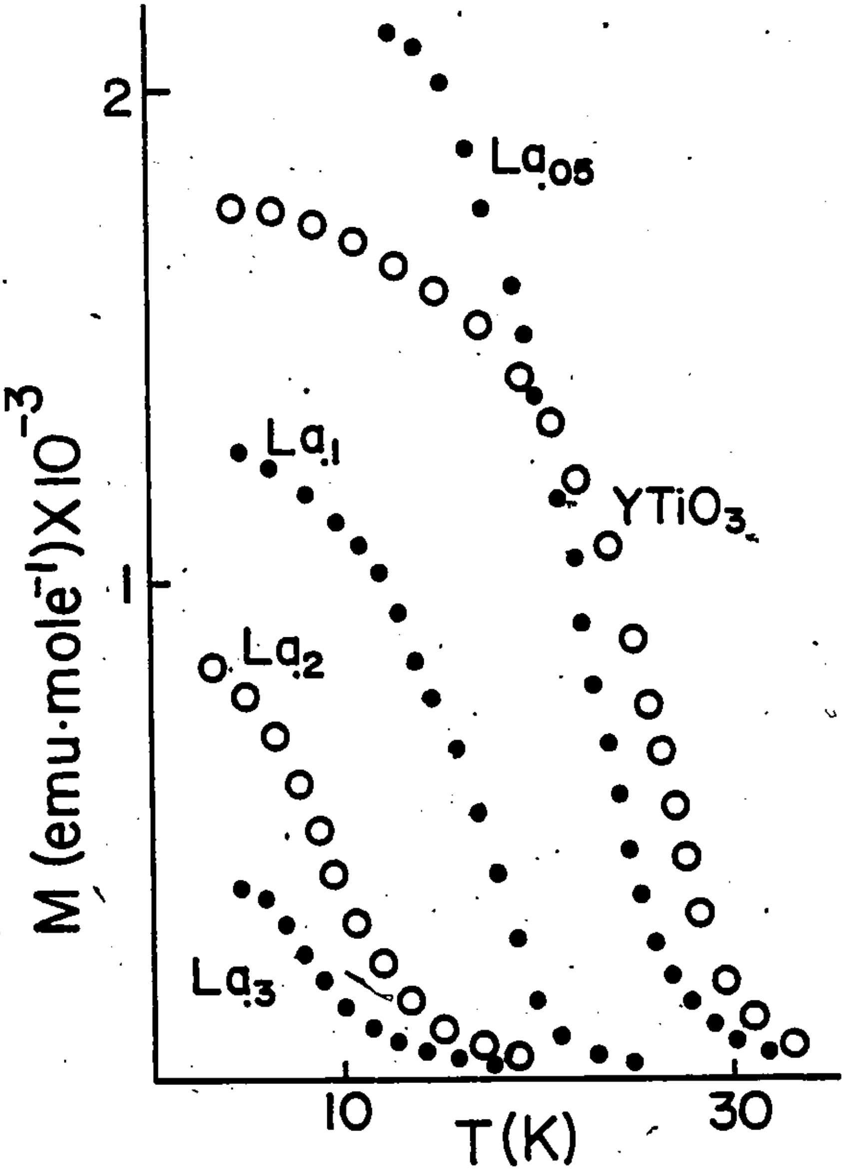

Fig. 4.7 Low-field magnetization vs. temperature for the phases $La_xY_{1-x}TiO_3$ (x = 0,.05, .1,.2,.3). Some data is from Greedan and MacLean (1978).

be adjusted structurally through the size of the rare earth ion. If these effects truly result from the change in the Ti-O-Ti bond angle as the rare earth size varies, there should be some correlation between the magnetic properties of the $La_xY_{1-x}TiO_3$ compounds and the other rare earth titanite phases having similar rare earth radii. Both the $CeTiO_3$ neutron data discussed previously and the mean field coupling constants derived for the heavy rare earth titanites suggest that the Ti-Ti coupling is the dominant exchange interaction in these materials (Turner and Greedan 1980). Fig. 4.8 shows the relationship between critical temperature and (rare earth radius)^3 for the $La_xY_{1-x}TiO_3$ system and the isostructural $RTiO_3$ compounds ($R = \text{Lanthanide}^{3+}$). The ionic radius of Ce^{3+} places $CeTiO_3$ on the borderline between the antiferromagnetic group (I) phases and the magnetically complex group (II) materials. Neutron diffraction data collected on this material suggest that the titanium sublattice may possess both ferromagnetic and antiferromagnetic components. The critical temperature assigned to magnetic ordering of the Ti sublattice in $CeTiO_3$ (116K) scales well with that inferred from the $La_xY_{1-x}TiO_3$ series. The magnetic structure of $PrTiO_3$ is unknown. The susceptibility at high temperatures follows the Curie-Weiss law. Magnetic ordering appears to set in at 96K although its exact nature is not understood. Magnetization-temperature data exhibit a field-dependent anomaly below T_c (MacLean et al. 1981). The ionic radius of Pr^{3+} places this material in region (II), where the magnetic properties of the corresponding $La_xY_{1-x}TiO_3$ phases are also poorly understood.

$NdTiO_3$ does not appear to order magnetically down to 4.2K (MacLean et al. 1981). Note that T_c for the $RTiO_3$ phases ($R = La^{3+}, Ce^{3+}, Pr^{3+}, Nd^{3+}$) drops sharply with decreasing ionic size. This behaviour is also observed in the corresponding $La_xY_{1-x}TiO_3$ compositions although the decrease in T_c is not as precipitous. The magnetic properties of $SmTiO_3$ are especially curious and have not been published (private communication). The susceptibility is field dependent. There is evidence of a cusp in the susceptibility near 50K but it is unclear whether or not this arises from long range magnetic ordering. The size of the Sm^{3+} ion places this compound in region (III). The magnetic behaviour of the $La_xY_{1-x}TiO_3$ phases in this class is equally puzzling.

In the heavy $RTiO_3$ compounds ($R = Tb^{3+}, Dy^{3+}, Ho^{3+}, Er^{3+}, Tm^{3+}, Yb^{3+}$) the titanium sublattice is ferromagnetically ordered (Turner et al. 1981, Turner et al. 1980). All these phases fall into group (IV) of the $La_xY_{1-x}TiO_3$ system where ferromagnetic exchange forces appear to dominate.

Qualitatively, at least, there seems to be a correlation between the Ti-Ti exchange mechanism and size of the rare earth ion in both the $La_xY_{1-x}TiO_3$ series and the pure rare earth titanites, $RTiO_3$. In cases where the nature of the exchange is known, there is agreement between the two systems. Both the $La_xY_{1-x}TiO_3$ solid solutions and $RTiO_3$ compounds display complex

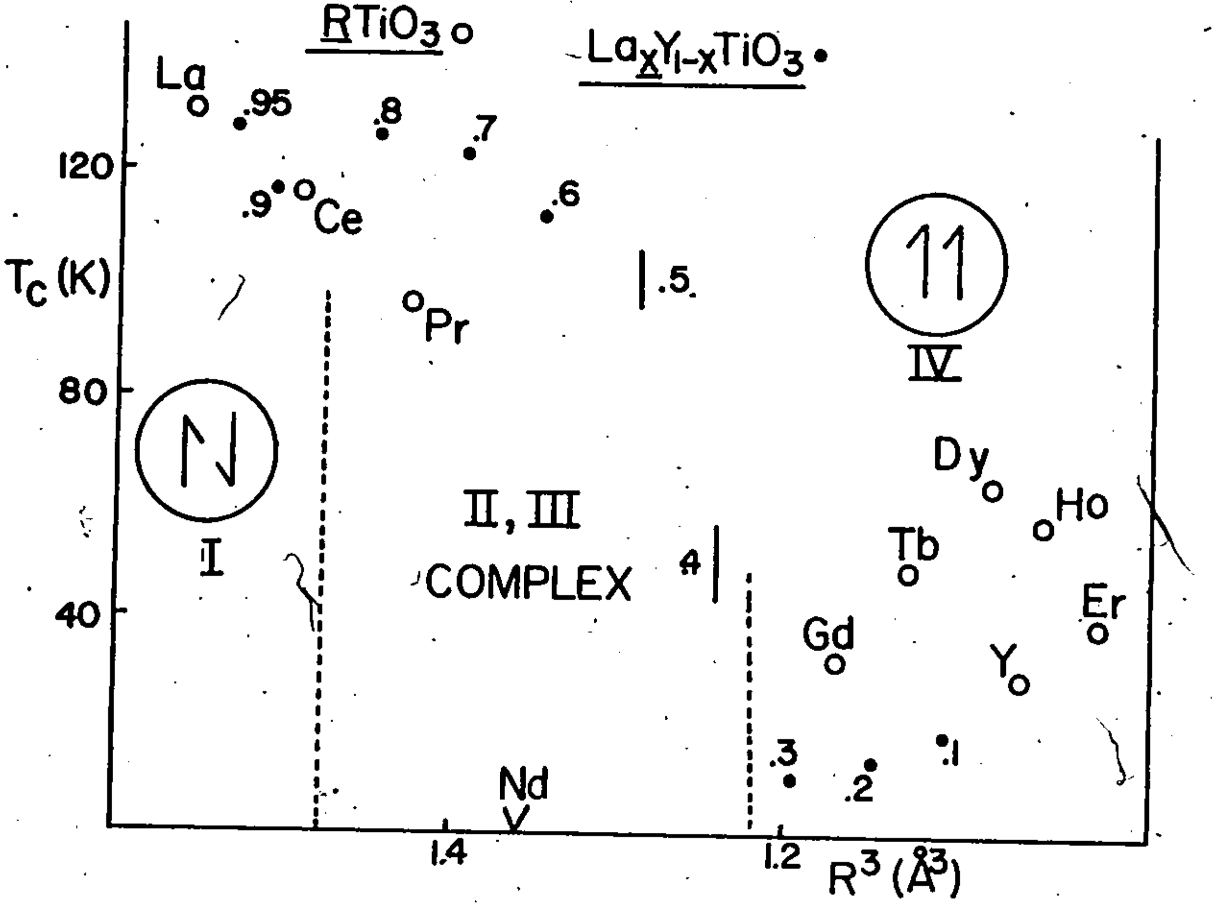

Fig. 4.8 Critical temperature vs. (effective rare earth radius)^3 for the $La_xY_{1-x}TiO_3$ and $RTiO_3$ systems.

magnetic behaviour for intermediate values of the rare earth radius. The dependence of T_c on the size of the rare earth ion is also qualitatively the same in both systems.

Electrical resistivity data were collected on single crystal samples of $La_{.1}Y_{.9}TiO_3$ and $La_{.2}Y_{.8}TiO_3$. Fig. 4.9 reveals a linear relationship between $\ln\rho$ and reciprocal temperature for both phases. The activation energies are .221(4) ($La_{.1}$) and .187(4) ($La_{.2}$) eV mole^{-1}. The rare earth radii of these materials correspond to those of $TbTiO_3$ and $GdTiO_3$ (Fig. 4.8). Resistivity curves obtained for sintered pellets of $TbTiO_3$ and $GdTiO_3$ are also characteristic of an activated transport mechanism (Bazuev and Shveiken, 1978). The reported activation energies are .20 ($TbTiO_3$) and .18 ($GdTiO_3$) eV mole^{-1}. MacLean (1980) calculates an activation energy of .18 eV mole^{-1} for a single crystal sample of $GdTiO_3$. Thus in this limited composition range ($x \leq .2$), there is good correlation between the transport properties of the $La_xY_{1-x}TiO_3$ system and the corresponding $RTiO_3$ compounds. Considered together, the magnetic and transport measurements on $La_{.1}Y_{.9}TiO_3$ and $La_{.2}Y_{.8}TiO_3$ strongly suggest that the Ti^{3+} $3d^1$ electron is localized.

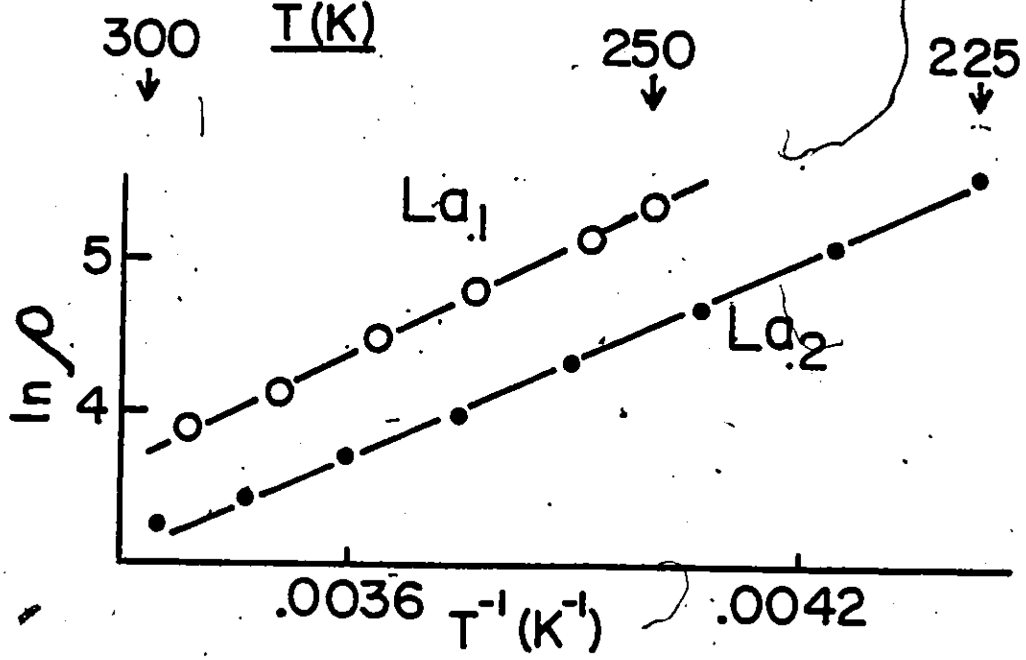

Fig. 4.9 Natural logarithm of the electrical resistivity (ohm-cm) vs. reciprocal temperature for $La_{.1}Y_{.9}TiO_3$ and $La_{.2}Y_{.8}TiO_3$. The activation energies are .221(4) eV $mole^{-1}$ and .187(4) eV $mole^{-1}$ respectively.

Table 4.1

Critical temperatures of the $La_xY_{1-x}TiO_3$ series

	T_c(K)
$YTiO_3$	29(2)
$La_{.1}$	19(2)
$La_{.2}$	14(2)
$La_{.3}$	11(2)
$La_{.4}$	43-57
$La_{.5}$	94-106
$La_{.6}$	112(4)
$La_{.7}$	123(4)
$La_{.8}$	125(4)
$La_{.9}$	115(2)
$La_{.95}$	127(2)
$LaTiO_3$	130(2)

CHAPTER 5

SUSCEPTIBILITY CALCULATIONS ON $La_xY_{1-x}TiO_3$ $(x = 0, .1, .2, .4, .7)$

5.1 Introduction

Susceptibility data in the range 77K - 300K have been reported for the phases $La_xY_{1-x}TiO_3$ $(x = 0, .1, .2, .4, .7)$ (MacLean 1980). χ^{-1} is linear with temperature only for $YTiO_3$ and $La_{.1}Y_{.9}TiO_3$ (Fig. 5.1). As the La content increases, deviations from the Curie-Weiss law become more pronounced. The data for all five of these compounds have been fitted to a model assuming both a temperature dependent and temperature independent contribution (MacLean 1980).

$$\chi = \frac{C}{T-\theta} + \chi_{tip}$$

χ_{tip}, the temperature-independent term , increases linearly with La content (Table 5.1). The growth of χ_{tip} may be interpreted as a composition dependent Pauli paramagnetism. In this light, the itinerant character [illegible] the Ti^{3+} electron increases as more La is added to the system. Both the electrical resistivity and magnetic susceptibility imply that $LaTiO_3$ is metallic above 125K.

It may also be possible to identify χ_{tip} with a van Vleck paramagnetism arising from the effect of the crystal field

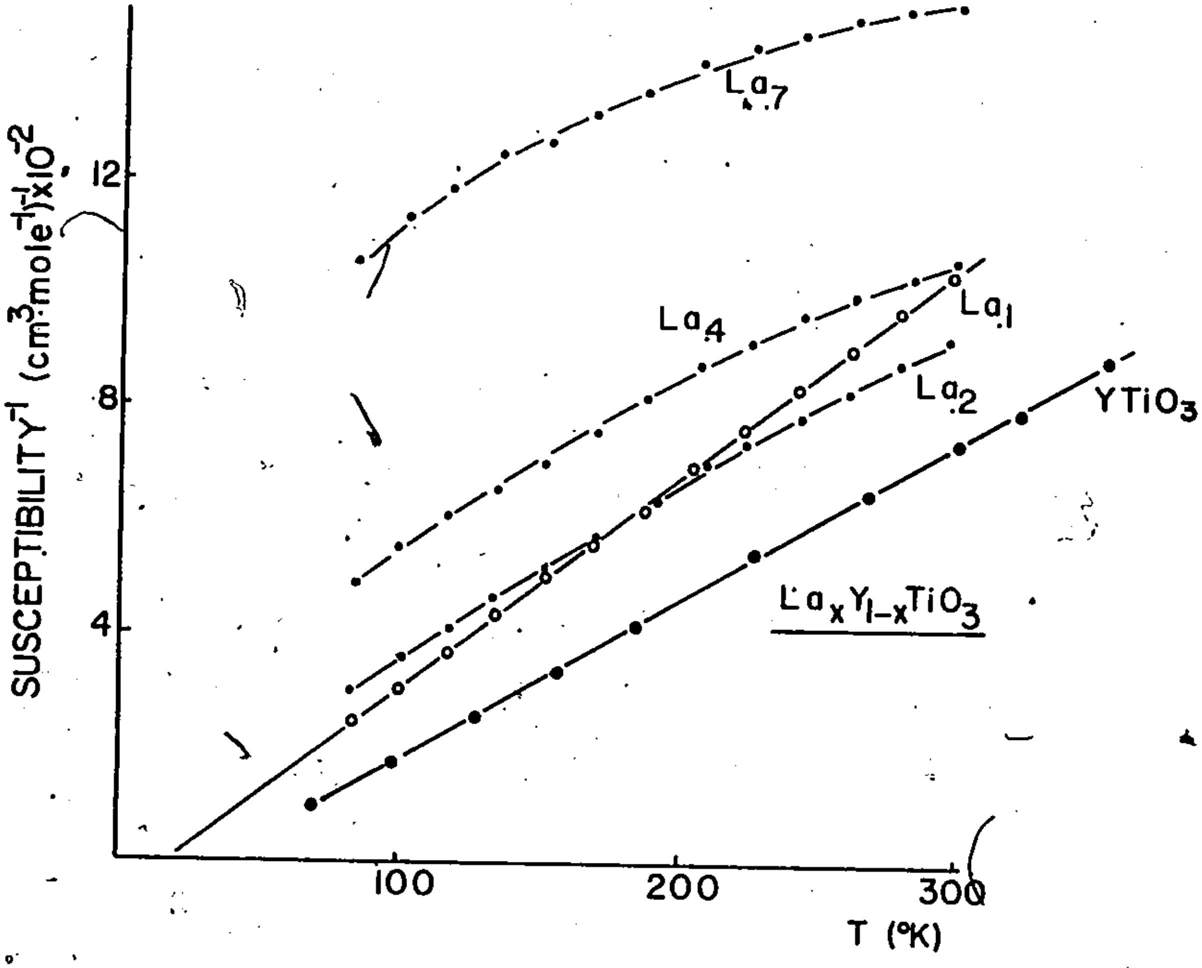

Fig. 5.1 Inverse susceptibility vs. temperature for the phases $La_xY_{1-x}TiO_3$ ($x = 0, .1, .2, .4, .7$) (from MacLean 1980).

Table 5.1

Magnetic and crystal field parameters for $La_xY_{1-x}TiO_3$

	$YTiO_3$	La $_{.1}$		La $_{.2}$	La $_{.4}$		La $_{.7}$	$LaTiO_3$
B_2^0(calc) ($\times 10^{14}$ ergs)	-3		-1	-2		-.3		2
C*(exptl.) (cm^3 K $mole^{-1}$)	.35	.27		.27	.17		.04	
C (calc) (cm^3 K $mole^{-1}$)	.24454(2)		.2152(3)			.144(2)		
χ^*_{tip}(exptl.) ($\times 10^6$ cm^3 $mole^{-1}$)	0	0		180	380		510	860
χ_{tip} (calc) ($\times 10^6$ cm^3 $mole^{-1}$)	54.1(3)		200(5)			760(3)		
μg (H=0) (μ_B)	.67		.62			.47		.07
μg (H=10^6 G) (μ_B)	.57		.54			.44		.66
η	.86			.86				.34

* from MacLean (1980).

on the localized Ti^{3+} ion. The resistivity data on $La_{.1}Y_{.9}TiO_3$ and $La_{.2}Y_{.8}TiO_3$ presented in the previous chapter imply that the Ti^{3+} $3d^1$ electron is localized.

Calculations were undertaken to determine if the general trends appearing in the experimentally observed susceptibilities could be reproduced based on crystal field arguments alone.

5.2 Theory

The electronic Hamiltonian of the Ti^{3+} electron may be expressed as the sum of three terms (Orton 1968).

$$\mathcal{H} = \mathcal{H}_{CF} + \mathcal{H}_{SO} + \mathcal{H}_{MAG}$$

$\mathcal{H}_{MAG}$ represents the interaction of the electron with a magnetic field. It is of the form $\mathcal{H}_{MAG} = \vec{H}\cdot(L+2S)$. $\vec{H}$ is the magnetic field and L,S are the orbital and spin momentum operators. The matrix element $\langle\phi_k^*|\mathcal{H}_{MAG}|\phi_k\rangle$ yields the interaction energy of the state ϕ_k with the magnetic field $\vec{H}$. $\mathcal{H}_{SO}$ expresses the coupling between the orbital and spin angular momenta. $\mathcal{H}_{SO} = \lambda L\cdot S$ where λ is the spin orbit coupling constant.

$\mathcal{H}_{CF}$, the crystal field Hamiltonian may be estimated by treating the surrounding ions as point charges and calculating the resulting electrostatic potential V. Assume a Ti^{3+} ion at the origin surrounded by an assembly of charges q_i disposed at positions $\vec{R}_i$. The electrostatic potential at a small distance $\vec{r}$ from the origin is

$$V = -\sum_i \frac{q_i}{|\vec{R}_i-\vec{r}|} .$$

For a single d^1 electron on Ti^{3+}, $H_{C.F.}$ may be expressed in the following form

$$H_{C.F.} = - \sum_i \frac{3eq_i}{|\vec{R}_i - \vec{r}|} .$$

The denominator of this expression involves complicated combinations of the single electron cartesian co-ordinates x, y and z. The method derived by Stevens (1952) replaces these spatial coordinates by the orbital angular momentum operators L_x, L_y and L_z. As a result, H_{CF} for the Ti^{3+} may be written in an equivalent form.

$$H_{CF} = \sum_{n=2,4} \sum_{m=-n}^{n} B_n^m O_n^m .$$

O_n^m are combinations of the orbital angular momentum operators. These Stevens operator equivalents have been tabulated by Hutchings (1964). B_n^m are crystal field intensity parameters which are usually derived experimentally. The values of n, m which appear in $H_{C.F.}$ are determined by the symmetry of the site in question. These relations have been compiled by Prather (1961).

The derivation of van Vleck's equation for χ, the magnetic susceptibility, may be found in many textbooks, for example Mabbs and Machin (1973).

$$\chi = \frac{\sum_i \sum_{j \neq i} \left(\frac{<\phi_i^*|L+2S|\phi_i>^2}{KT} - \frac{2<\phi_i^*|L+2S|\phi_j><\phi_j^*|L+2S|\phi_i>}{(E_i - E_j)} \right) \exp(- \frac{E_i}{KT})}{\sum_i \exp(- \frac{E_i}{KT})}$$

ϕ_k is the Ti^{3+} wavefunction at energy E_k which has been determined after consideration of the crystal field and spin orbit effects. Stevens (1953) has suggested that the free ion value of L is not appropriate in the above calculation of χ. He has shown that the overlap of the Ti^{3+} and ligand orbitals has the effect of reducing the orbital angular momentum of the pure metal wavefunction. Thus in calculating the magnetic susceptibility, the orbital angular momentum operator L appearing in the van Vleck equation has been replaced by pL where p is an orbital reduction factor. The value of p has been set to .8. The values of p for complexes of the first row transition metals fall in the range .7 - 1.0 (Gerloch and Miller 1968, Boudreaux and Mulay 1976).

5.3 Calculations and Discussion

In both $LaTiO_3$ and $YTiO_3$, the Ti^{3+} ion is surrounded by six nearest neighbour oxide ions. Within one standard deviation for the bond lengths and angles, these O^{2-} ions form a perfect octahedron in $LaTiO_3$. In $YTiO_3$, the X-ray data of MacLean et al. (1979) indicate a uniaxial elongation of the oxide cage. The precise site symmetry of the Ti^{3+} ions in both compounds is $\bar{1}$. Following the method of Stevens (1952) the crystal field Hamiltonian for Ti^{3+} contains eight terms.

$$H_{CF} = B_2^0O_2^0 + B_2^1O_2^1 + B_2^2O_2^2 + B_4^0O_4^0 + B_4^1O_4^1 + B_4^2O_4^2 + B_4^3O_4^3 + B_4^4O_4^4 .$$

Inclusion of all these parameters is not justified considering the small data base available. Instead the initial wavefunctions chosen were those of a d^1 electron in an octahedral field (Table 5.2). The octahedral field splitting was fixed at 20,000 cm^{-1}. A value of 18,000 cm^{-1} has been reported for Cr^{3+} doped into the isostructural $YAlO_3$ (Weber and Varitimos 1974).

H_{SO} and H_{CF} were applied as simultaneous perturbations on the octahedral field states (Levine 1974). The spin orbit coupling constant λ was set at the free ion value of 155 cm^{-1} (Mabbs and Machin 1973). The eight term crystal field Hamiltonian discussed above was approximated by H'_{CF}, a single parameter perturbation on the octahedral field states.

$$H'_{CF} = B_2^0 O_2^0$$

$B_2^0 O_2^0$ is the dominant parameter which describes the tetragonal elongation of the nearest neighbour oxygen octahedron. As the aim of this investigation was to reproduce the general features of the observed susceptibilities rather than to quantitatively duplicate the experimental data, the remaining terms in H_{CF} have been neglected.

B_2^0 may be calculated from EFG, the electric field gradient (Ofer 1968).

$$B_2^0 = \frac{V_{zz}\langle r^2\rangle(1-\sigma_2)}{42} \qquad (\text{for } d^1) .$$

$\langle r^2\rangle$ is the expectation value of the (electronic radius)^2 of the 3d electron of the Ti^{3+} ion. This has been fixed at the

Table 5.2

Initial wavefunctions of the d^1 system in an octahedral crystal field

$(\phi = |L_z,S_z>)$

$\phi_1 = |1,\frac{1}{2}>$

$\phi_2 = |1,-\frac{1}{2}>$

$\phi_3 = |-1,\frac{1}{2}>$

$\phi_4 = |-1,-\frac{1}{2}>$

$\phi_5 = 1/\sqrt{2}(|2,\frac{1}{2}>-|-2,\frac{1}{2}>)$

$\phi_6 = 1/\sqrt{2}(|2,-\frac{1}{2}>-|-2,-\frac{1}{2}>)$

$\phi_7 = |0,\frac{1}{2}>$

$\phi_8 = |0,-\frac{1}{2}>$

$\phi_9 = 1/\sqrt{2}(|2,\frac{1}{2}>+|-2,\frac{1}{2}>)$

$\phi_{10} = 1/\sqrt{2}(|2,-\frac{1}{2}>+|-2,-\frac{1}{2}>)$

free ion value of .53 Å^2 (Orton 1968). $(1-\sigma_2)$ is an electronic shielding factor. This term represents the degree of distortion of the core electrons from spherical symmetry due to the polarizing effects of the valence electrons. The magnitude of this factor was set at .8. V_{xx}, V_{yy} and V_{zz} are the principal components of EFG at the Ti^{3+} site. V_{zz} is defined as the largest of these components. The electric field gradient was calculated by a lattice summation assuming charges of +3 for both Ti^{3+} and the rare earth ions and -2 for the oxide ion.

A parameter η may be defined which reflects the asymmetry of the crystal field at the Ti^{3+} site due to the arrangement of the surrounding ions in the lattice.

$$\eta = \left|\frac{V_{xx}-V_{yy}}{V_{zz}}\right| \qquad |V_{zz}| \geq |V_{xx}| \geq |V_{yy}|$$

The values of B_2^0 and η calculated for $YTiO_3$, $La_{.2}Y_{.8}TiO_3$ and $LaTiO_3$ are given in Table 5.1. The symmetry parameter η is significantly smaller for $LaTiO_3$ than for the two Y-rich phases. This is not surprising since of all the $RTiO_3$ compounds studied, $LaTiO_3$ most closely resembles the cubic perovskite structure. It is interesting to note that the B_2^0 crystal field term obtained from the lattice summation changes sign somewhere in the composition range $La_{.2}Y_{.8}TiO_3$-$LaTiO_3$. This is not to be expected if one considers only the nearest neighbour coordination geometry. Crystallographic data on $YTiO_3$ confirm a tetragonal elongation of the nearest neighbour oxygen octahedron. This type of distortion implies a positive value of B_2^0.

From Table 5.1, it appears as though the value of B_2^0 becomes less negative as the La/Y ratio increases. B_2^0 values of -3×10^{-14}, -1×10^{-14}, -3×10^{-15} and 2×10^{-14} ergs were chosen to span the composition range $YTiO_3$ through $LaTiO_3$. The resulting wavefunctions are listed in Table 5.3 along with the corresponding energies.

In the absence of exchange, the wavefunctions occur as doublets in all cases. For $B_2^0 > 0$, the ground state doublets are non-magnetic within the strict crystal field approximation. The small ground state moment reported for the model based on $LaTiO_3$ ($B_2^0 = 2\times10^{-14}$ ergs) is due to the orbital reduction parameter p, which allows the mixing of the titanium and oxygen wavefunctions. Room temperature optical studies on single crystal $YTiO_3$ show two weak absorption bands at 1673K and 1841K (Fig. 5.2, MacLean 1980). These were assigned to d-d transitions from the ground doublet to the nearest neighbour doublets. The energy level scheme derived using the B_2^0 calculated for $YTiO_3$ predicts transitions at 1856K and 2091K.

Calculated inverse susceptibility curves are shown in Fig. 5.3. Clearly the data calculated for $LaTiO_3$ ($B_2^0 = 2\times10^{-14}$ ergs) bear no resemblance to the Pauli paramagnetic susceptibility observed experimentally. It is apparent that this simple crystal field approach is not applicable to this compound.

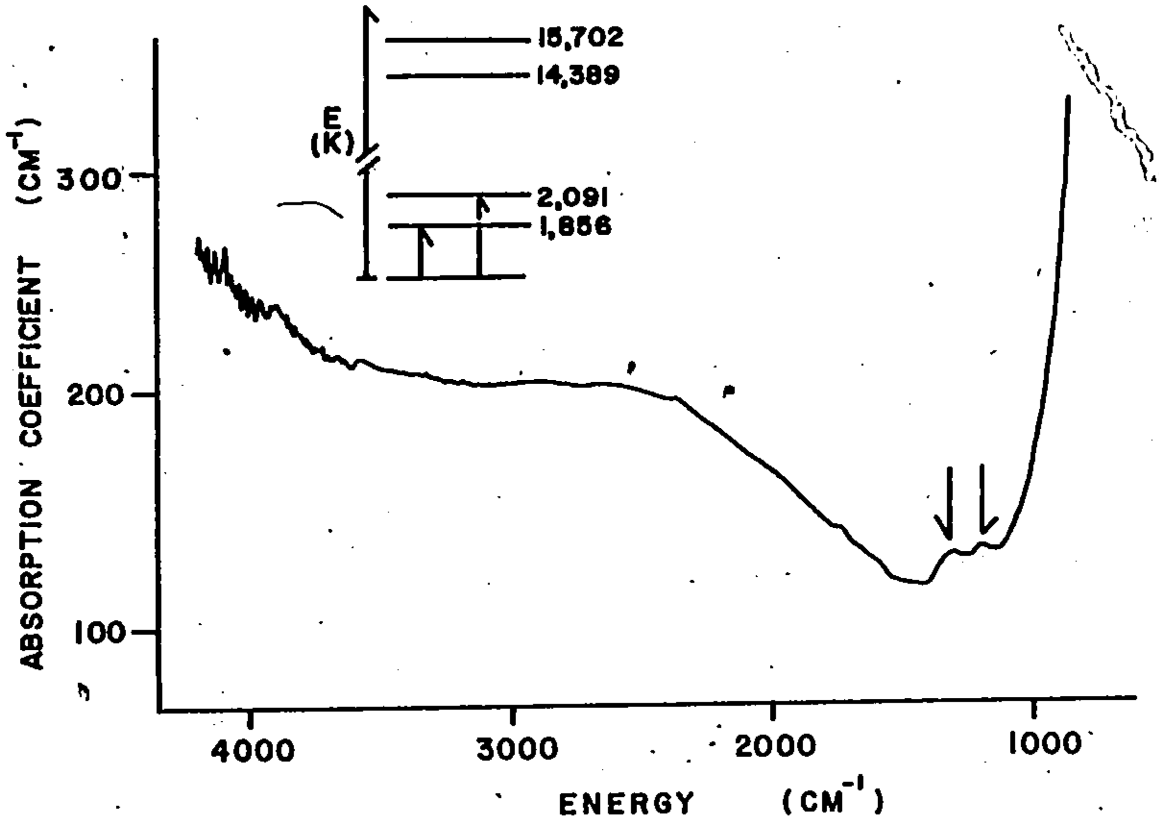

Fig. 5.2 The absorption spectrum of $YTiO_3$ in the range 800 cm^{-1} to 4000 cm^{-1}, obtained at 300K (from MacLean 1980). The inset shows the calculated energy levels for $YTiO_3$ ($B_2^0 = -3\times10^{-14}$ ergs).

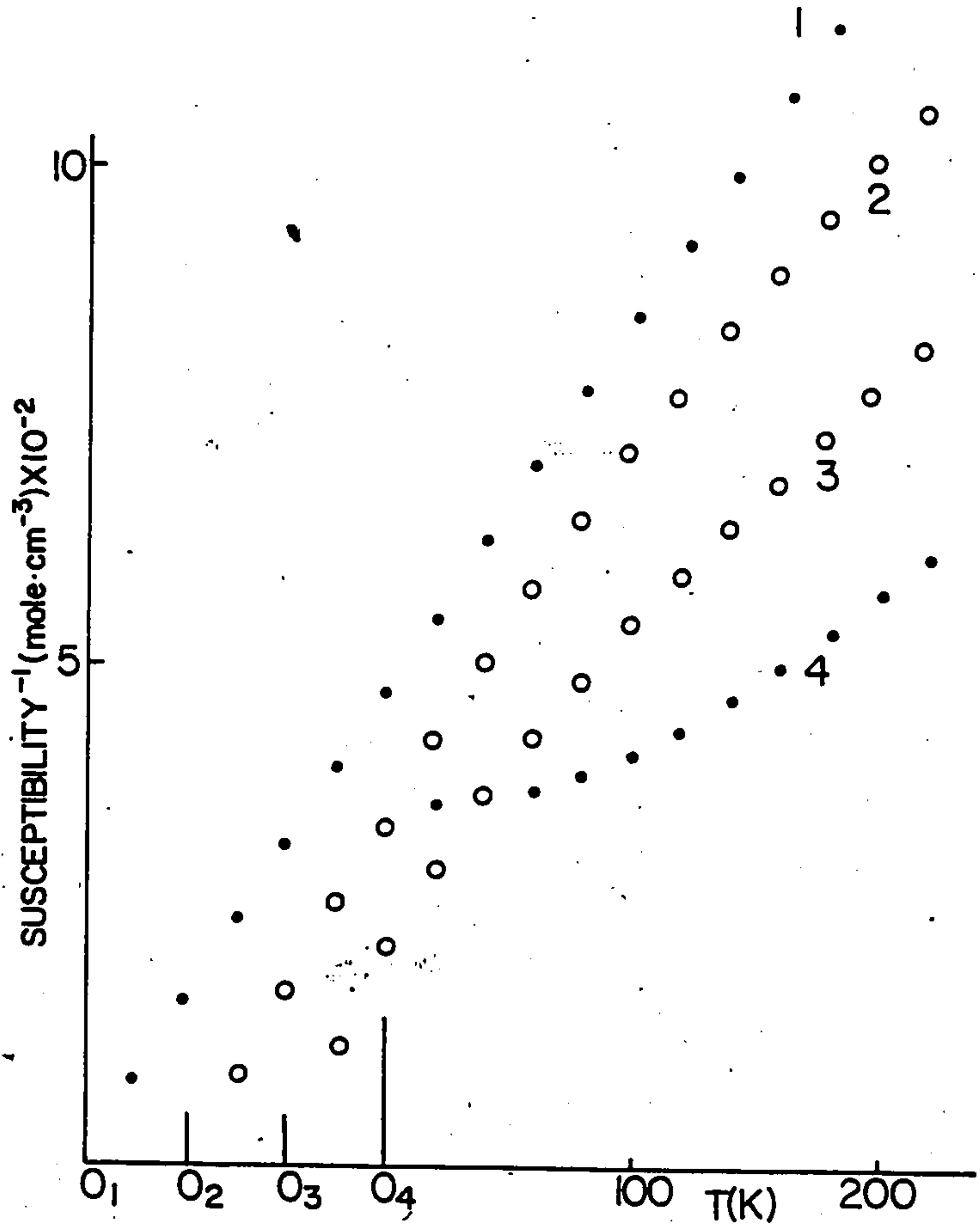

Fig. 5.3 Calculated inverse susceptibility vs. temperature for various values of B_2^0. Note that the temperature scale is shifted for clarity.

(1) $B_2^0 = -3\times10^{-14}$ ergs, (2) $B_2^0 = -1\times10^{-14}$ ergs

(3) $B_2^0 = -3\times10^{-15}$ ergs, (4) $B_2^0 = 2\times10^{-14}$ ergs.

Table 5.3

Calculated wavefunctions for $La_xY_{1-x}TiO_3$

B_2^0 ($\times 10^{14}$ ergs)	-3 ($YTiO_3$)	-1	$-.3$	2 ($LaTiO_3$)
ψ_1	$-.076\ \phi_1+.997\ \phi_6$	$-.195\ \phi_1+.981\ \phi_6$	$-.395\ \phi_1+.921\ \phi_6$	ϕ_2
ψ_2	$.076\ \phi_4+.997\ \phi_5$	$.195\ \phi_4+.981\ \phi_5$	$.389\ \phi_4+.921\ \phi_5$	ϕ_3
ψ_3	ϕ_2	ϕ_2	ϕ_2	$-.129\ \phi_6+.992\ \phi_1$
ψ_4	ϕ_3	ϕ_3	ϕ_3	$.129\ \phi_5+.992\ \phi_4$
ψ_5	$.076\ \phi_6+.997\ \phi_1$	$.195\ \phi_6+.981\ \phi_1$	$.389\ \phi_6+.921\ \phi_1$	$.129\ \phi_1+.992\ \phi_6$
ψ_6	$-.076\ \phi_5+.997\ \phi_4$	$-.195\ \phi_5+.981\ \phi_4$	$-.389\ \phi_5+.921\ \phi_4$	$-.129\ \phi_4+.992\ \phi_5$
ψ_7	ϕ_9	ϕ_9	ϕ_9	ϕ_7
ψ_8	ϕ_{10}	ϕ_{10}	ϕ_{10}	ϕ_8
ψ_9	ϕ_7	ϕ_7	ϕ_7	ϕ_9
ψ_{10}	ϕ_8	ϕ_8	ϕ_8	ϕ_{10}

(continued next page)

Table 5.3 (continued)

Energy of levels (K)

B_2^0 (×10^{14} ergs)	-3	-1	-.3	2
ψ_1, ψ_2	0	0	0	0
ψ_3, ψ_4	1,856*	572	151	202
ψ_5, ψ_6	2,091*	826	440	1,436
ψ_7, ψ_8	14,389	14,417	14,453	14,932
ψ_9, ψ_{10}	15,702	14,852	14,583	15,801

*$YTiO_3$ - experimentally observed transitions at 1673K and 1841K (MacLean 1980)

$\phi_1 - \phi_{10}$ are defined in Table 5.2

$\lambda = 155$ cm^{-1} $p = .8$ $10\ Dq = 2\times10^4$ cm^{-1}

For the B_2^0 value estimated for $YTiO_3$ (-3×10^{-14} ergs), χ^{-1} appears almost linear with temperature. As $|B_2^0|$ decreases, deviations from the Curie-Weiss law become more apparent. This is precisely the behaviour observed experimentally as the La content increases. In analogy with the susceptibility data reported for $La_xY_{1-x}TiO_3$ ($x=0,.1,.2,.4,.7$), the calculated susceptibilities have been expressed in terms of a temperature dependent and temperature independent contribution. ($\chi=\frac{C}{T}+\chi_{tip}$). The results are presented in Table 5.1. Although the agreement is not quantitative, the observed variations in C and χ_{tip} with increasing La concentration are generated by the predicted decrease in $|B_2^0|$.

Magnetic exchange may be introduced into the system as an effective internal field whose magnitude may be inferred from the Weiss constant θ (Cullity, 1972). For $YTiO_3$ the internal field so calculated is on the order of 10^6 gauss. In an attempt to estimate the ground state moment, this internal field has been introduced as an additional perturbation using H_{mag} discussed previously. The result of this calculation is a decrease in the ground state moment with increasing La concentration (Table 5.1). This trend has been observed experimentally by Greedan and MacLean (1978) for the phases $La_xY_{1-x}TiO_3$ ($x=0-.5$).

Thus the general features of the inverse susceptibility curves of the compositions $La_xY_{1-x}TiO_3$ ($x=0,.1,.2,.4,.7$) have been reproduced assuming a localized Ti^{3+} electron model. Using an admittedly deficient crystal field Hamiltonian, satisfactory agreement (within 15%) has been obtained between the energies of the predicted and observed optical transitions in YTiO$_3$. These calculations are also consistent with the observed decrease in magnetic moment with La composition. The above results coupled with magnetic and transport data discussed in the previous chapter strongly indicate that the Ti^{3+} 3d^1 electron is localized in the La$_x$Y$_{1-x}$TiO$_3$ system for values of $x \leq .2$.

CHAPTER 6

THE MAGNETIC PROPERTIES OF THE $La_xGd_{1-x}TiO_3$ SOLID SOLUTIONS

6.1 Introduction

The magnetic properties of the $La_xY_{1-x}TiO_3$ series have been shown to be varied and complex. The La-rich compounds adopt a canted antiferromagnetic structure while the phases $YTiO_3$-$La_{.3}Y_{.7}TiO_3$ appear to be ferromagnets. The behaviour of the intermediate compositions is intriguing and not yet understood. Since the rare earth ions are diamagnetic in this system, these effects are solely due to the Ti^{3+} $3d^1$ electrons. Correlations have been drawn between the magnetic properties of this series and those of the pure rare earth titanites, $RTiO_3$. Arguments have been made suggesting that the nature of the Ti-Ti exchange may be adjusted structurally through manipulation of the Ti-O-Ti bond angle.

In the $La_xGd_{1-x}TiO_3$ system the variation in the Ti-O-Ti bond angle is almost as great as in the La-Y series. The effect of the rare earth-titanium interactions may be more easily monitored than in the $RTiO_3$ series where the identity of R^{3+} is not constant. Gd^{3+} has the added advantage of being an S-state ion, therefore the crystal field effects present in many rare earth compounds will not be a complicating factor. As in the $YTiO_3$ and the other heavy rare earth titanites, the

Ti^{3+} sublattice in $GdTiO_3$ appears to be ferromagnetically ordered (Turner and Greedan 1980).

6.2 Results and Discussion

Magnetization-temperature curves were collected on all phases prepared. Composition dependent features in the magnetization appear over two separate temperature intervals; one below 20K, the other in the range 80 - 130K. For the compositions $La_{.5}Gd_{.5}TiO_3$-$La_{.98}Gd_{.02}TiO_3$ effects are present in both regions simultaneously. The M vs. T curves of the phases $LaTiO_3$-$La_{.5}Gd_{.5}TiO_3$ all exhibit a smooth drop in the magnetization in the region 130-80K (Fig. 6.1,6.2). This behaviour is most pronounced for $LaTiO_3$ and becomes less well defined as the Gd content increases. In analogy with the corresponding $La_xY_{1-x}TiO_3$ phases, this effect is identified as a critical temperature arising from magnetic ordering within the Ti^{3+} sublattice. The magnitude of T_c diminishes as the La/Gd ratio decreases (Table 6.1). For the phases $La_{.8}Gd_{.2}TiO_3$-$La_{.5}Gd_{.5}TiO_3$, the magnetization in the region of T_c is field dependent (Fig. 6.3). The application of an external field on order 10 KG suppresses all evidence of a critical temperature. Hysteresis in isothermal magnetization curves was observed at temperatures below this T_c but not above it. At temperatures above 60K, the M vs T curves of $LaTiO_3$, $La_{.95}Gd_{.05}TiO_3$ and $La_{.9}Gd_{.1}TiO_3$ are very similar. It is most likely that the titanium sublattice

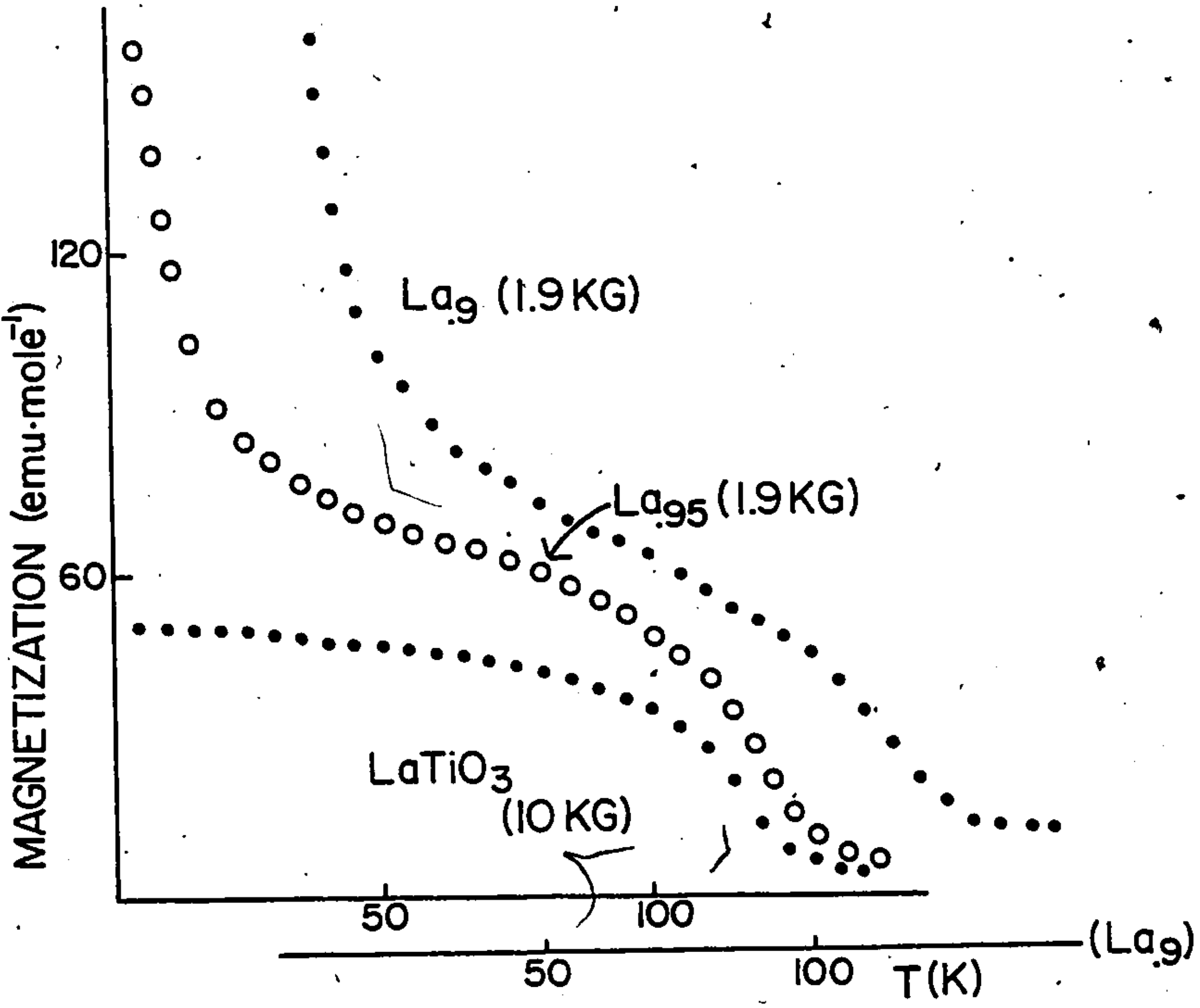

Fig. 6.1 Magnetization vs. temperature for $LaTiO_3$, $La_{.95}Gd_{.05}TiO_3$ and $La_{.9}Gd_{.1}TiO_3$. The applied field is given in brackets.

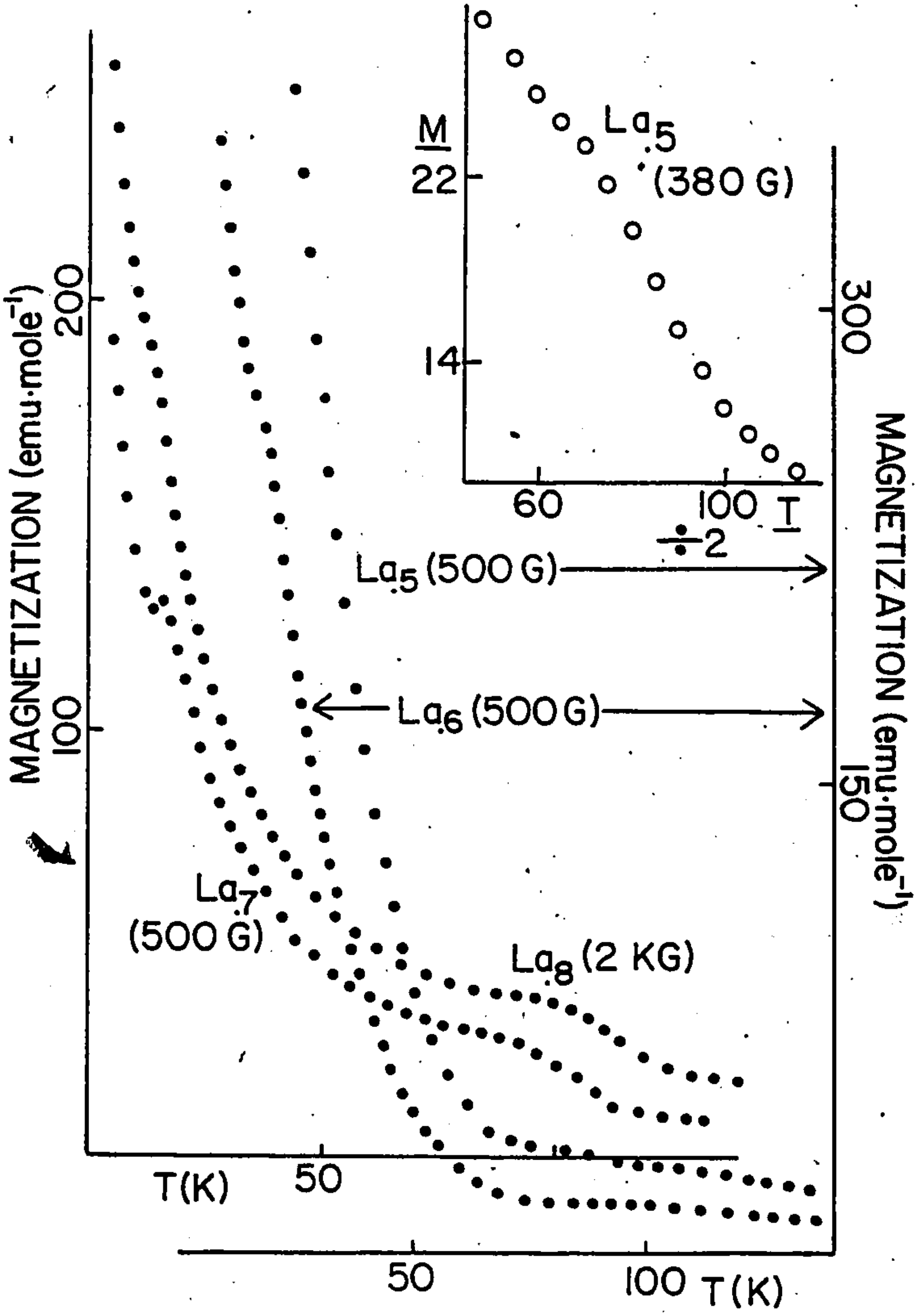

Fig. 6.2 Magnetization vs. temperature for the phases $La_xGd_{1-x}TiO_3$ (x = .5,.6,.7,.8). The scale for the 70% La and 80% La compounds is on the left, that for the 50% La and 60% La compounds is on the right. The magnitude of M for $La_{.5}Gd_{.5}TiO_3$ is one-half that shown on the right. The units of M and T on the insert are the same as those shown in the main graph. The applied field is given in brackets

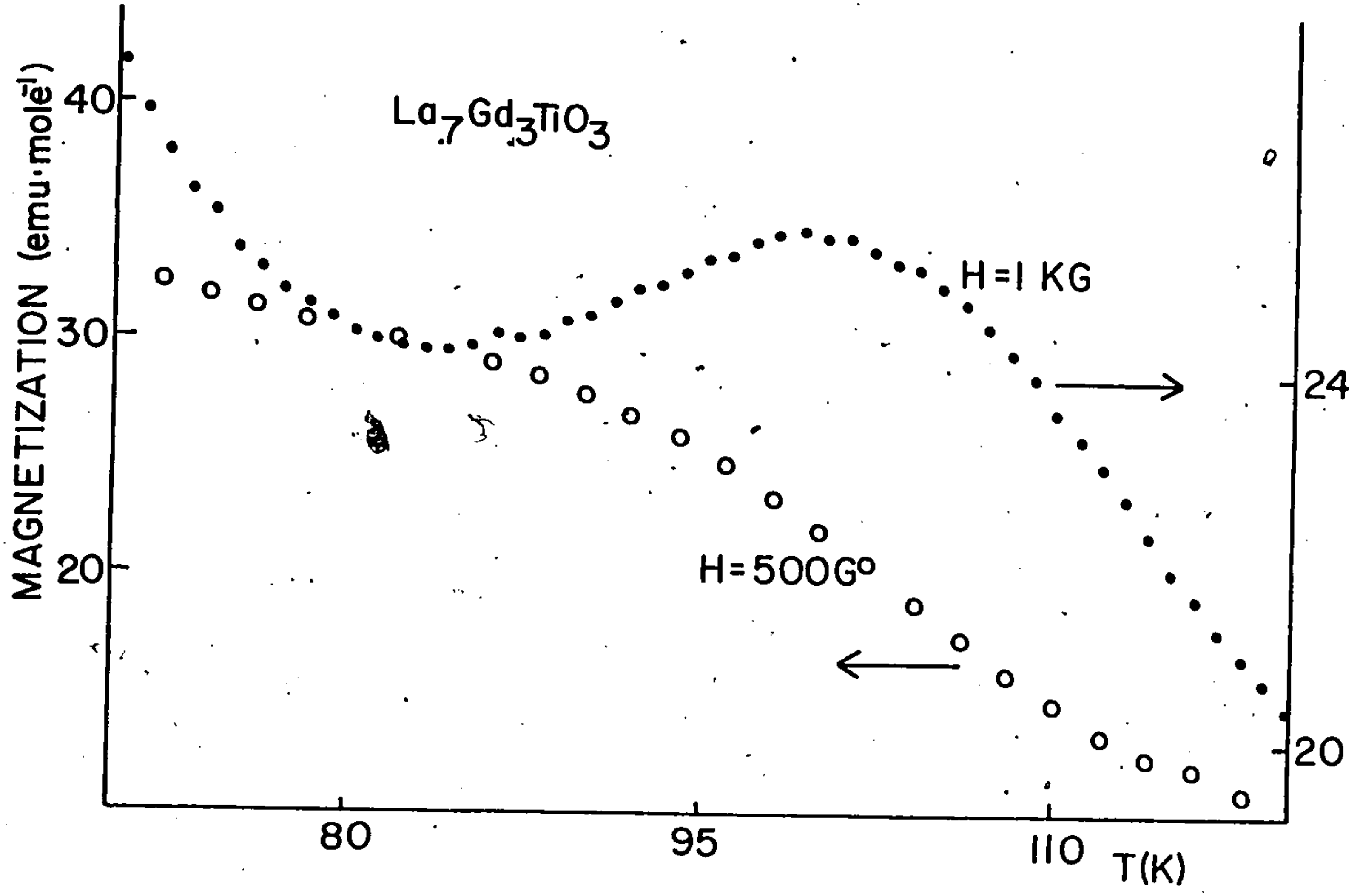

Fig. 6.3 Magnetization vs. temperature for $La_{.7}Gd_{.3}TiO_3$ at applied fields of 500 G and 1000 G.

in these materials orders in a canted antiferromagnetic arrangement as postulated for the corresponding phases $LaTiO_3$-$La_{.9}Y_{.1}TiO_3$. In the La-Gd system however, the introduction of small amounts of the magnetic rare earth ion leads to effects which are observable at low temperatures. For the phases $La_{.95}Gd_{.05}TiO_3$ and $La_{.9}Gd_{.1}TiO_3$, the magnetization increases sharply and smoothly with decreasing temperature below 30K. This feature is entirely absent in the La-Y system. Fig. 6.4 shows the magnetization temperature curves for $La_{.9}Gd_{.1}TiO_3$ and $La_{.9}Y_{.1}TiO_3$. Assuming the Ti-Ti interactions to be the same in both compounds, the contribution to M due to the rare earth ions has been extracted by means of a point by point subtraction of the two curves. This difference $(M(La_{.9}Gd_{.1}TiO_3)-M(La_{.9}Y_{.1}TiO_3))$ is shown in figure 6.5 expressed as an inverse susceptibility. The curve obeys the Curie Weiss law down to 4.2K. The Curie constant of .80(2) is very close to the .787 cm^3 K $mole^{-1}$ predicted for a paramagnetic rare earth sublattice of 90% La^{3+}/10% Gd^{3+}. The value of θ (-8(1)K) suggests the existence of antiferromagnetic exchange interactions. Note from Fig. 6.4 that the sum of the magnetic moment calculated for a paramagnetic 90% La^{3+}/10% Gd^{3+} sublattice plus the signal measured for $La_{.9}Y_{.1}TiO_3$ results in a magnetization larger than that observed for $La_{.9}Gd_{.1}TiO_3$. This behaviour is also consistent with the presence of antiferromagnetic exchange, most

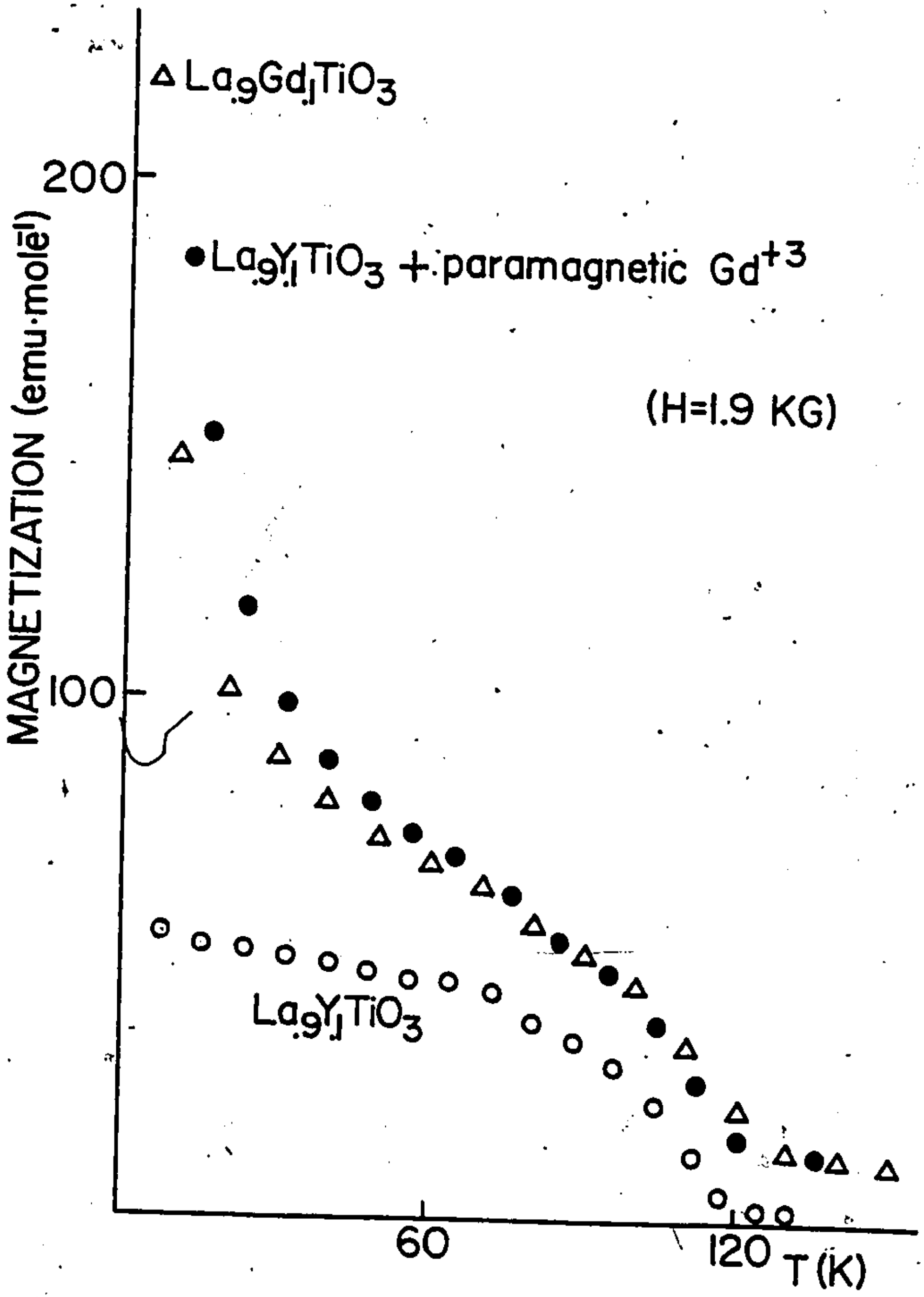

Fig. 6.4 Magnetization vs. temperature for $La_{.9}Gd_{.1}TiO_3$ and $La_{.9}Y_{.1}TiO_3$ at an applied field of 1.9 kG. Also shown is the magnetization expected for a paramagnetic lattice of 90% La^{3+}/10% Gd^{3+} added to that obtained for $La_{.9}Y_{.1}TiO_3$.

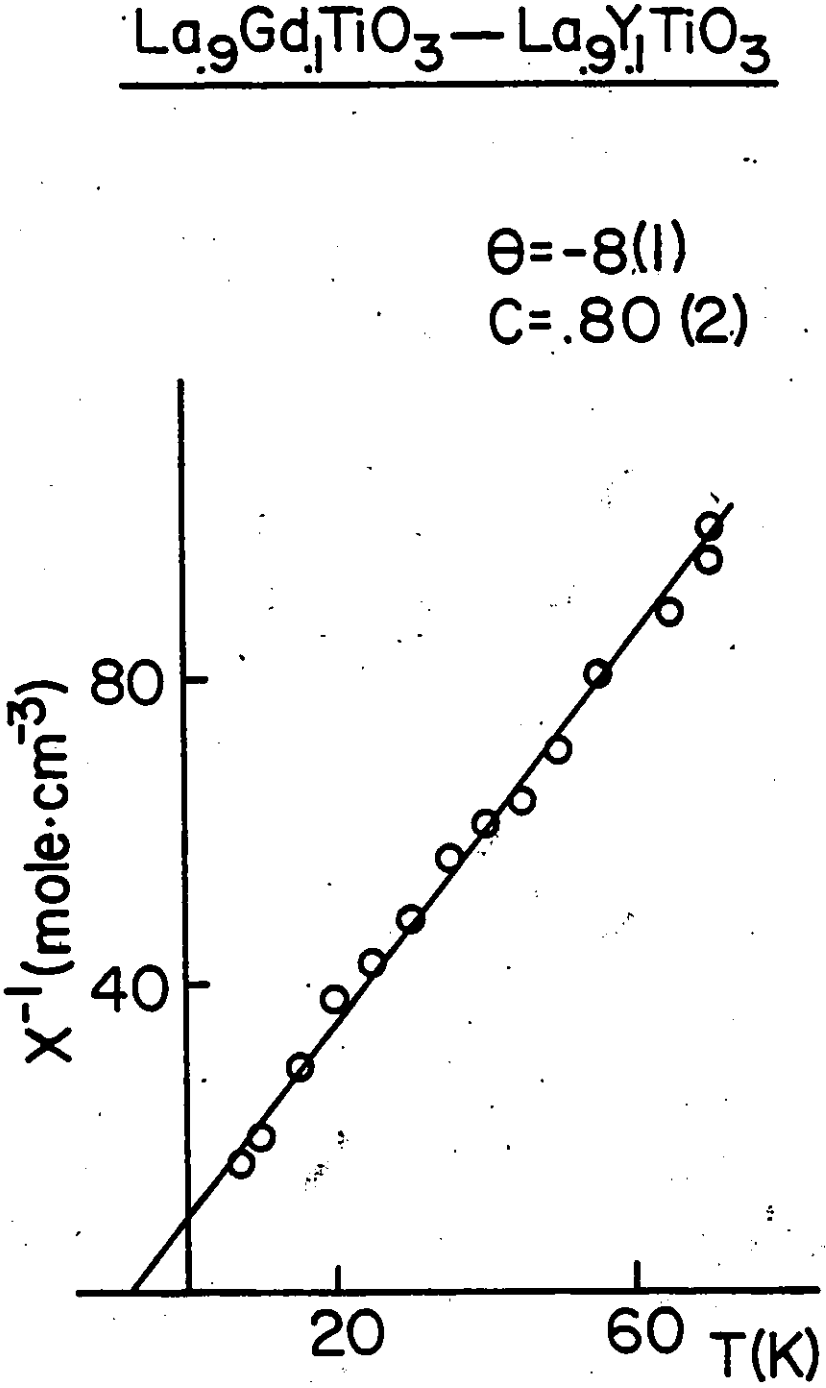

Fig. 6.5 Inverse susceptibility vs. temperature derived by subtraction of $M(La_{.9}Gd_{.1}TiO_3) - M(La_{.9}Y_{.1}TiO_3)$ in Fig. 6.4.

likely between Ti^{3+} and Gd^{3+}. This is not surprising since the Gd-Ti coupling is antiferromagnetic in the parent compound $GdTiO_3$. It should be stressed that the data presented in Fig. 6.5 show no evidence for magnetic ordering down to 4.2K, suggesting that these magnetic interactions are short range. From these considerations, it appears as though the phases $LaTiO_3$-$La_{.9}Gd_{.1}TiO_3$ are closely related to the corresponding $LaTiO_3$-$La_{.9}Y_{.1}TiO_3$ compositions. In both cases it is probable that the Ti^{3+} sublattice orders in a canted antiferromagnetic array. The critical temperatures in both series are comparable. The introduction of up to 10% Gd^{3+} does not seem to effect the titanium ordering at high temperatures although the effect of short range antiferromagnetic interactions (most likely between Gd^{3+} and Ti^{3+}) becomes observable below 30K. The compositions $LaTiO_3$-$La_{.9}Gd_{.1}TiO_3$ form group (I) of the $La_xGd_{1-x}TiO_3$ solid solutions.

The phases $La_{.8}Gd_{.2}$-$La_{.6}Gd_{.4}TiO_3$ comprise group (II). These compounds exhibit a high temperature T_c associated with ordering within the titanium sublattice. In addition, the smooth curvature of the low temperature magnetization observed for the group (I) compounds develops a fine structure. At applied fields of ∿ 500 G an anomalous linear region appears in the neighbourhood of 15K (Fig. 6.2). As the field is increased, the anomaly is systematically suppressed. In the case of

$La_{.7}Gd_{.3}TiO_3$, this anomaly takes the form of a cusp at low field which disappears as the applied field increases (Fig. 6.6). This behaviour is characteristic of a spin glass. While an actual cusp in the magnetization was observed only for $La_{.7}Gd_{.3}TiO_3$, deviations from the smooth curvature of the M vs T data persist for both the La 60% and La 80% phases. It is possible that the applied field of 500 G was large enough to suppress the cusp in these latter materials. Applied fields on the order of 10 G are usual in spin glass studies (Tholence et al. 1979). It has been postulated that one condition for spin glass behaviour may be the simultaneous coexistence of positive and negative exchange interactions (Beck 1981, Maletta and Felsch 1979). Exchange interactions of both sign are expected in these materials considering the ferrimagnetic structure of $GdTiO_3$. These data are insufficient to unambiguously characterize the spin glass system. It is probable however that the dominant interactions involve both Gd^{3+} and Ti^{3+}. Recall that these anomalies appear in the vicinity of 15K. Critical temperatures associated with rare earth-rare earth coupling in the isostructural $RAlO_3$ compounds are usually much lower than this (Goodenough and Longo 1970, Blazey and Rohrer 1967). The relatively dilute concentration of the magnetic rare earth ion also discounts significant Gd^{3+}-Gd^{3+} interactions. In summary, the M vs T curves of the group (II) compounds ($La_{.8}Gd_{.2}TiO_3$-$La_{.6}Gd_{.4}TiO_3$) exhibit two distinctive features.

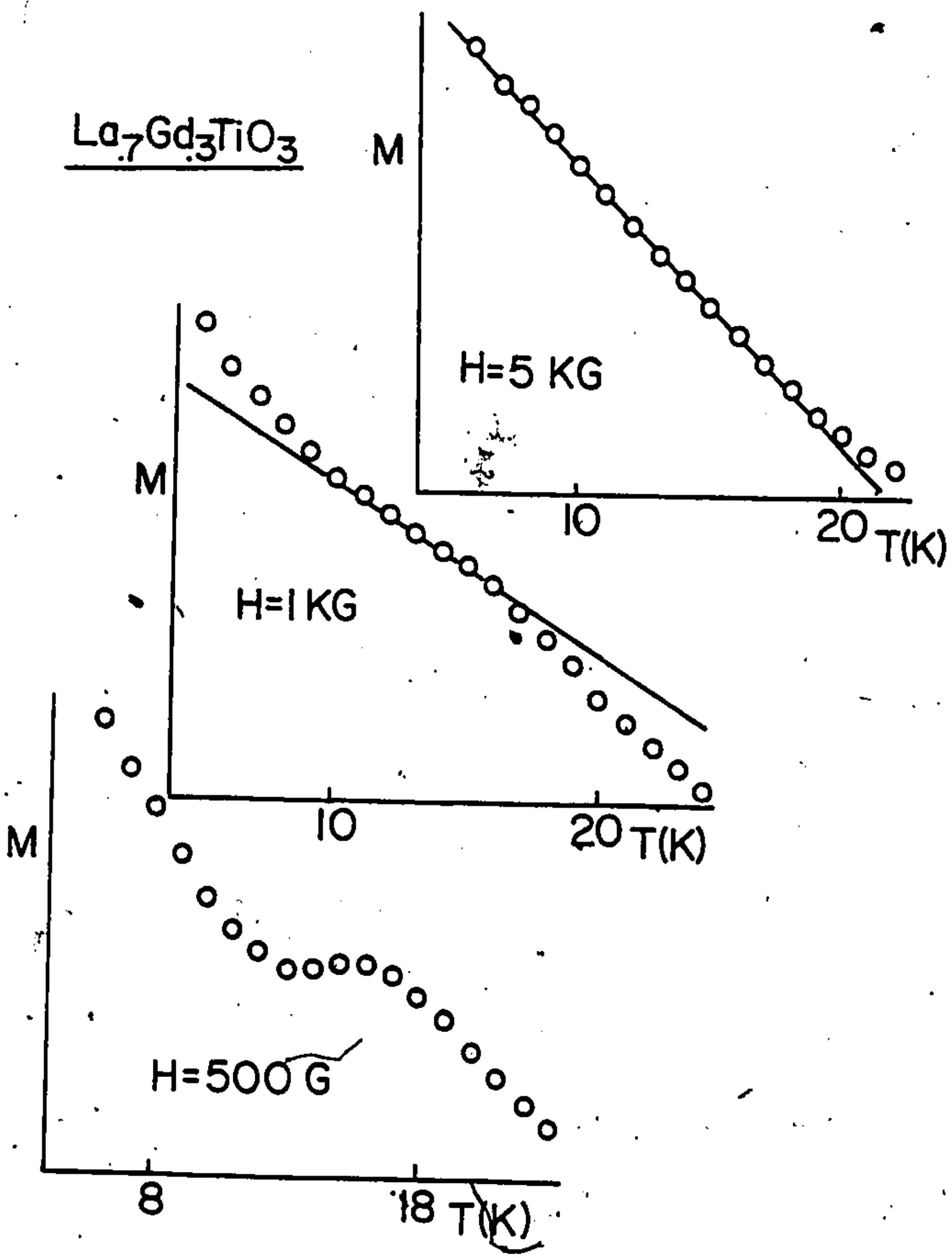

Fig. 6.6 Magnetization vs. temperature for $La_{.7}Gd_{.3}TiO_3$ at applied fields of 500 G, 1000 G and 5000 G.

A high temperature T_c is attributed to ordering of the Ti^{3+} sublattice. This critical temperature becomes less well-defined as the Gd concentration increases, suggesting that the canted antiferromagnetic structure postulated for the group (I) phases may be altered as more Gd^{3+} is added to the system. There is also evidence of spin glass behaviour below 20K. These magnetic interactions are thought to involve both Ti^{3+} and Gd^{3+}.

The magnetization-temperature curves of the group (IV) compounds ($GdTiO_3$-$La_{.3}Gd_{.7}TiO_3$) are all similar. They are characterized by a single smooth drop in the magnetization in the region 33 - 12K. The magnitude of T_c drops as the La content increases (Fig. 6.7). These values were estimated by linear extrapolation of M^2 vs T. Susceptibility data were collected on these compounds in the range 4K - 200K at an applied field of ∿ 1 T. Plotted as inverse susceptibility vs temperature (Fig. 6.8) these data exhibit curvature indicative of a 2 sublattice ferrimagnet. The curves were fitted to the Neel hyperbola

$$\chi^{-1} = \frac{T-\theta}{C} - \frac{\xi}{T-\theta'}$$

and the mean field coupling constants were extracted (Table 6.1). The results of these calculations imply that the ferromagnetic Ti-Ti coupling is the strongest magnetic interaction in the system. The strength of the coupling drops sharply as the effec-

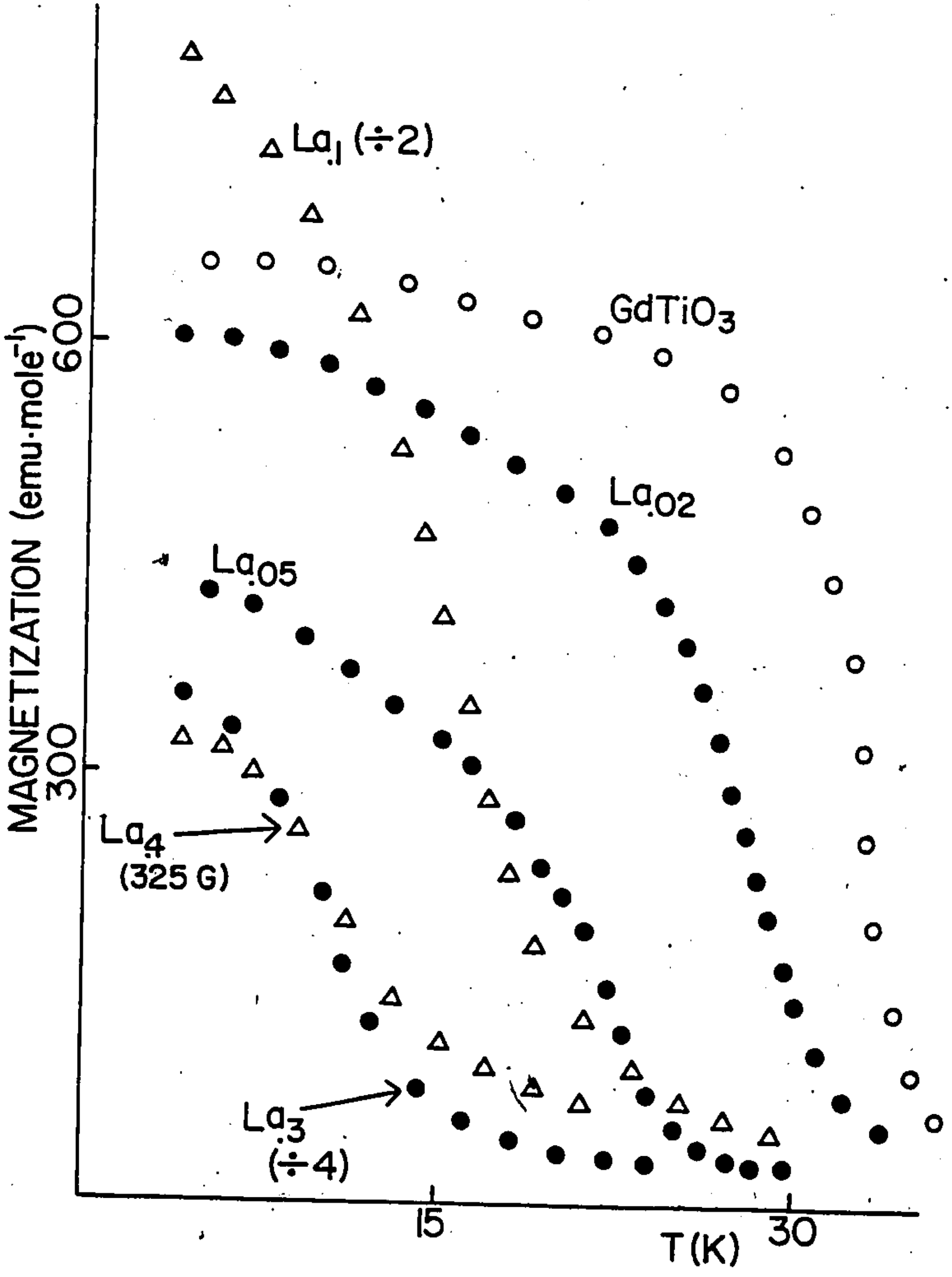

Fig. 6.7 Magnetization vs. temperature for the phases $La_xGd_{1-x}TiO_3$ (x = 0,.02,.05,.1,.3,.4). The magnitude of M for the 10% La phase is one half that shown. The magnitude of M for the 30% La phase is one quarter that shown. All data were obtained at an applied field of 45 G except that of the 40% La phase.

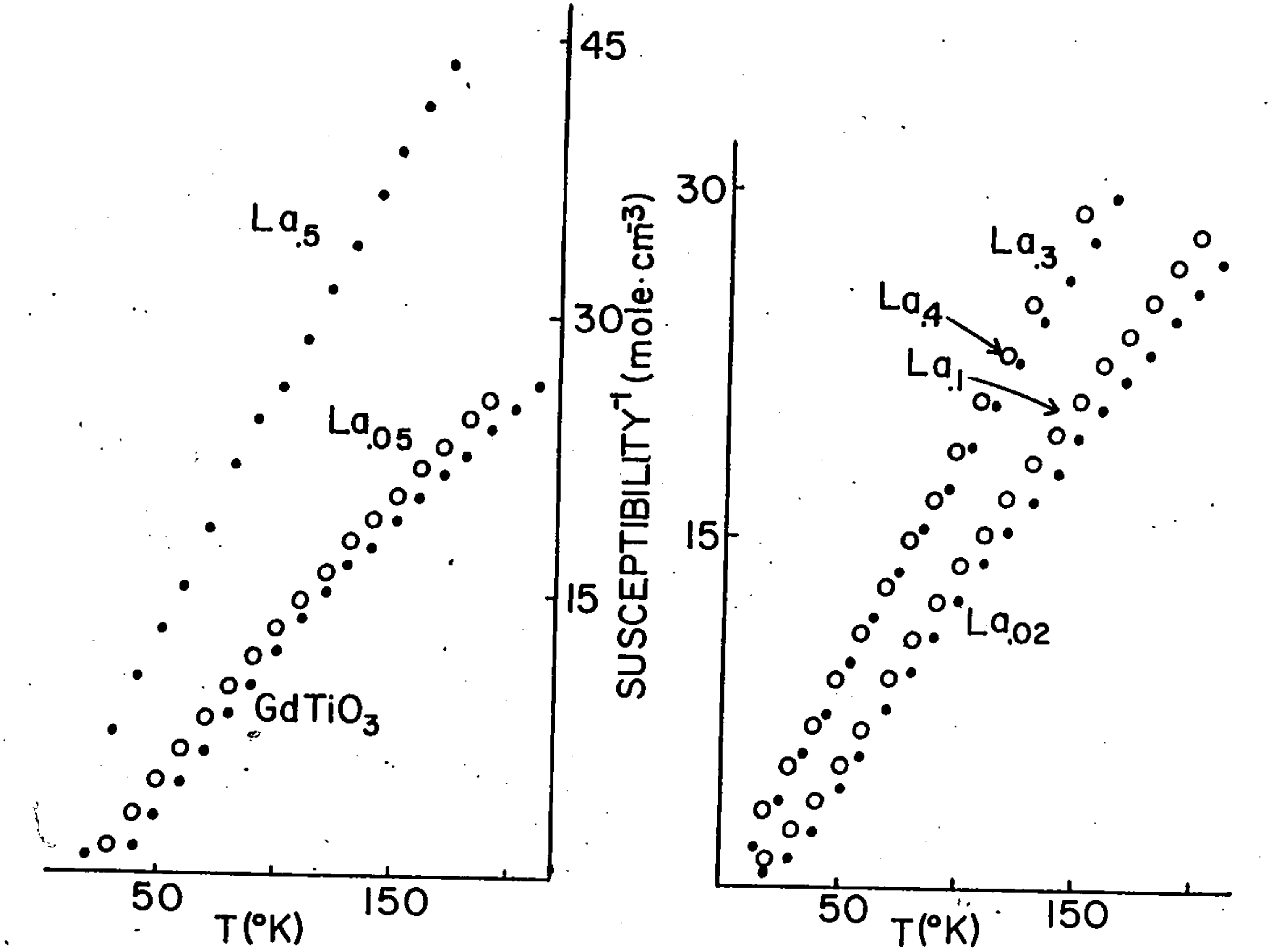

Fig. 6.8 Inverse susceptibility vs. temperature for the phases $La_xGd_{1-x}TiO_3$ (x = 0, .02, .05, .1, .3, .4, .5). The data were collected at an applied field of about 1 T.

tive rare earth radius increases. This is consistent with the observed dependence of T_c on rare earth size in the ferromagnetic regions of the $La_xY_{1-x}TiO_3$ and $RTiO_3$ series. The influence of Ti^{3+}-Gd^{3+} coupling diminishes as the Gd^{3+} sublattice is diluted with diamagnetic La^{3+}. The Gd^{3+}-Gd^{3+} interaction is small and does not vary systematically. Assuming the colinear ferrimagnetic model, the Curie constant for Ti^{3+} can be derived from these χ^{-1} data.

$$C(Ti^{3+}) = C_{total} - C_{Gd^{3+}} .$$

In all five compounds, $C(Ti^{3+})$ is markedly reduced from the free ion value of .37 ion cm^3 K $mole^{-1}$. Unfortunately these values are not significant with respect to the error in the experimentally observed C_{total}, on order of ±.1 cm^3 K $mole^{-1}$.

Magnetic saturation was achieved at 4.2K on single crystalline samples of $GdTiO_3$ and $La_{.02}Gd_{.98}TiO_3$. The data for the phases $La_{.05}Gd_{.95}TiO_3$ and $La_{.1}Gd_{.9}TiO_3$ were extrapolated to infinite field. For the Gd rich compositions, saturation becomes more difficult as the La/Gd ratio increases (Fig. 6.9). The moment of 5.8±.2 μ_B/F.U. observed for $GdTiO_3$ is in good agreement with the 6 μ_B/F.U. predicted by the simple two-sublattice ferrimagnetic model. The Ti^{3+} saturation moments estimated from these curves are 1.1±.2 μ_B for $GdTiO_3$ and 1.0±.02 μ_B for the remaining three phases. These values are consistent with the .84±.01 μ_B reported for Ti^{3+} in the ferromagnet $YTiO_3$

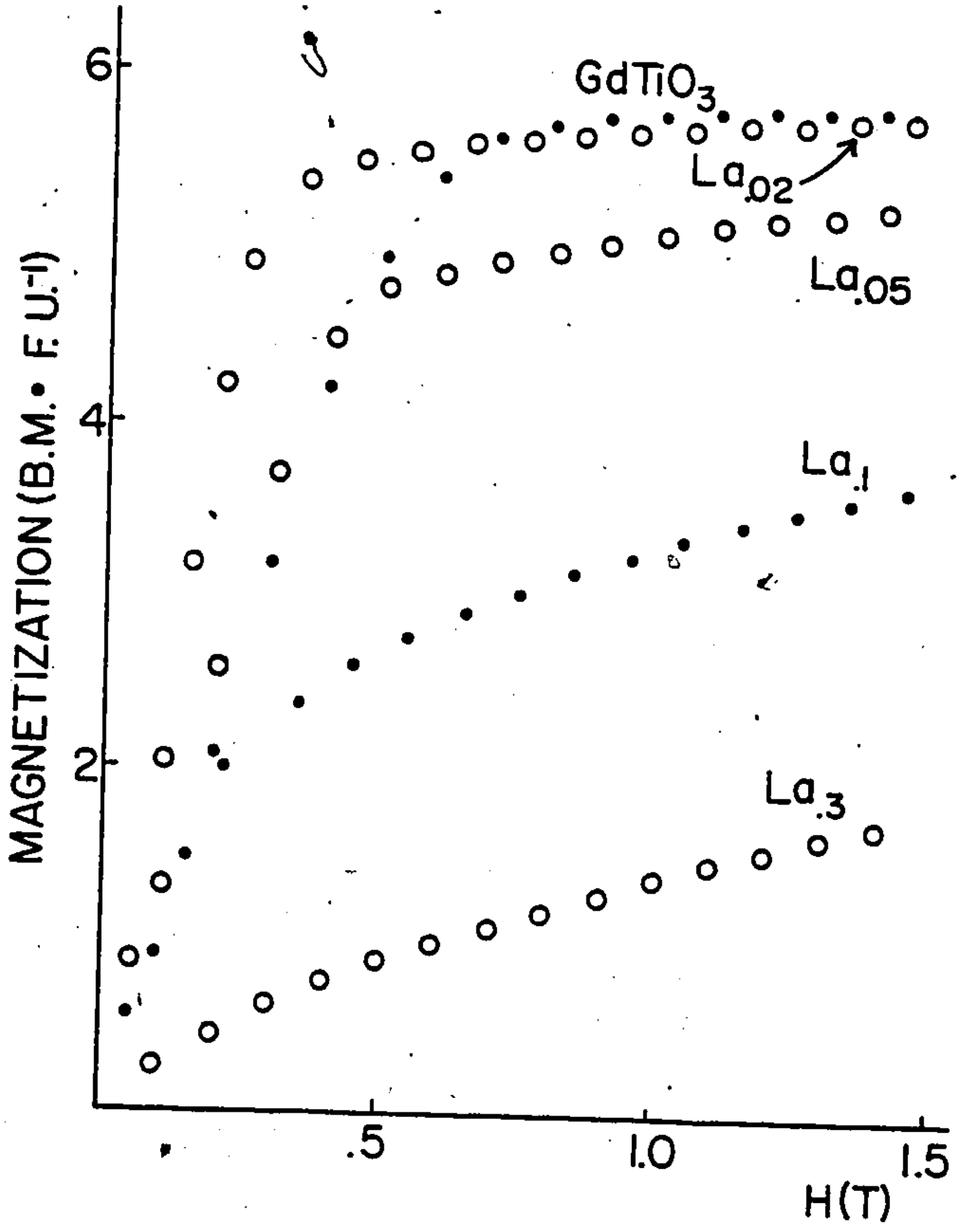

Fig. 6.9 Magnetization vs. field for the phases $La_xGd_{1-x}TiO_3$ (x = 0, .02, .05, .1, .3). The data were obtained at 4.2K.

(Garrett et al. 1981). In summary the group (IV) compositions $GdTiO_3$-$La_{.3}Gd_{.7}TiO_3$ appear to be 2-sublattice ferrimagnets. The strength of the magnetic interactions decreases as the effective rare earth radius increases. For the phases $GdTiO_3$-$La_{.1}Gd_{.9}TiO_3$ the saturation moments observed for Ti^{3+} are consistent with a spin only d^1 system.

$La_{.5}Gd_{.5}TiO_3$ and $La_{.4}Gd_{.6}TiO_3$ form the group (III) phases. The magnetic properties of these compounds are the least well characterized in the $La_xGd_{1-x}TiO_3$ system. The only feature present in the M vs T curve of $La_{.4}Gd_{.6}TiO_3$ is a smooth, sharp drop in the magnetization near 14K. $La_{.5}Gd_{.5}TiO_3$ exhibits similar behaviour near 16K. Recall however that this compound also displays a critical temperature at 85K associated with magnetic ordering within the Ti^{3+} sublattice. The nature of the low temperature anomaly is not understood. It is probable however that negative exchange interactions are involved at low temperature. For both the La 50% and La 40% phases, the experimentally observed magnetization-field curves have been compared to those calculated for a paramagnetic Gd^{3+} sublattice of the appropriate composition (Fig. 6.10). In both cases the magnetization calculated for a paramagnetic rare earth contribution only is greater than the total magnetization observed experimentally.

Susceptibility data have been collected at an applied field of ∿ 1 T. Under the influence of this large external

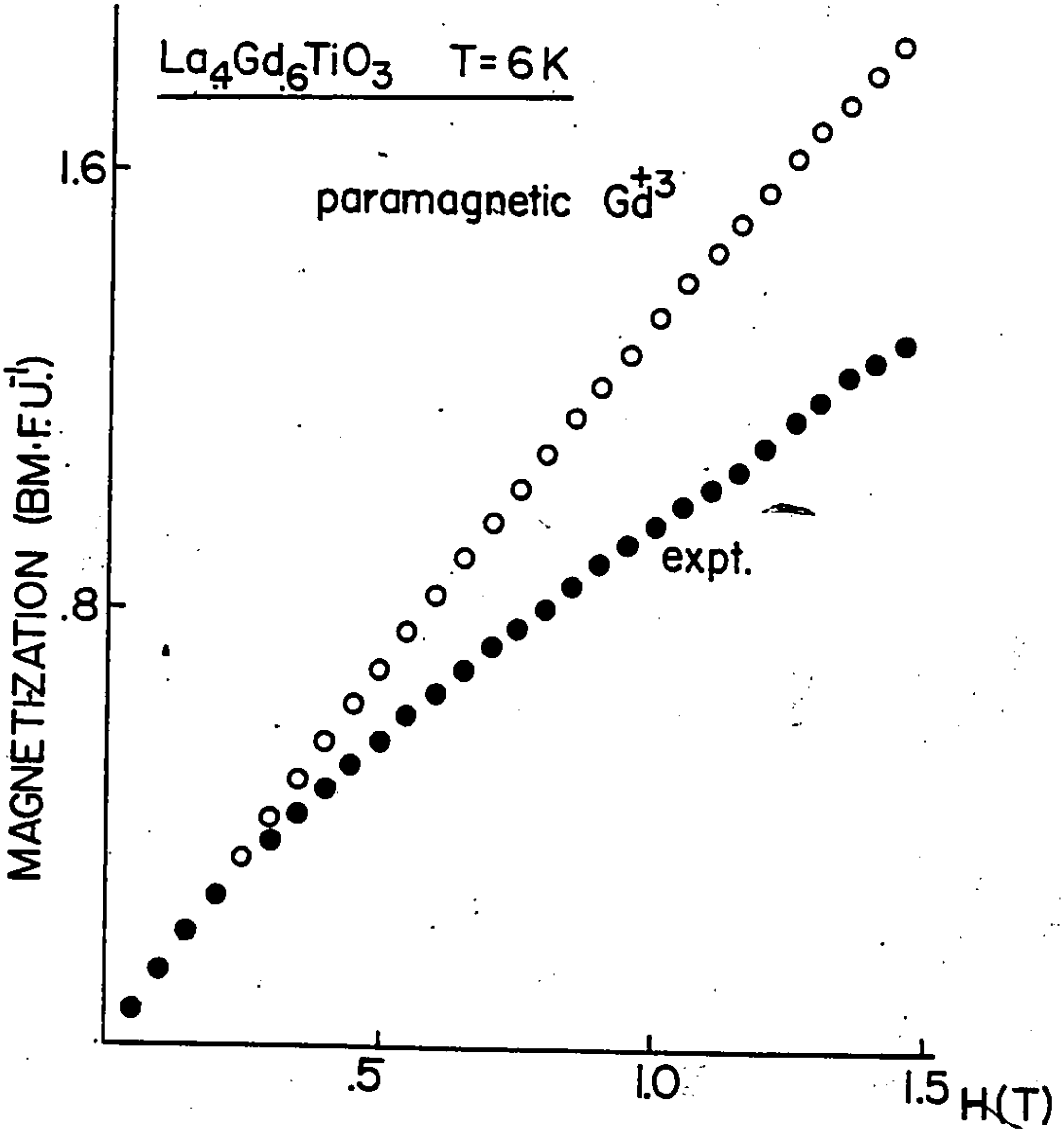

Fig. 6.10 Magnetization vs. field for $La_{.4}Gd_{.6}TiO_3$ at 6K. Also shown is the magnetization expected for a paramagnetic sublattice of 40% La^{3+}/60% Gd^{3+}.

field the curvature indicative of T_c observed for $La_{.5}Gd_{.5}TiO_3$ at 380 G (Fig. 6.2, insert) disappears. For both phases the results follow the Curie-Weiss law down to the low temperature anomaly. The significance of C and θ are difficult to interpret (Table 6.1).

The magnetic properties of the $La_xGd_{1-x}TiO_3$ system are summarized in Fig. 6.11. Certain features observed in this series are also common to the $La_xY_{1-x}TiO_3$ and $RTiO_3$ systems. In all three series, the compounds which display predominantly antiferromagnetic ordering of the Ti^{3+} sublattice have comparable effective rare earth radii. The same is true of the phases where the Ti^{3+} ions are most likely ferromagnetically ordered. This is apparent from Fig. 6.12 where T_c is plotted against (rare earth radius)^3 for all three systems. The agreement is exceptionally good between the $La_xGd_{1-x}TiO_3$ and $RTiO_3$ series. Perhaps this is due to the presence of rare earth-titanium magnetic interactions which are absent in the $La_xY_{1-x}TiO_3$ phases. Admittedly, the relationships discussed are only qualitative and the conclusions drawn are tentative. A more rigorous development of the concepts presented here necessitates extensive crystallographic and magnetic neutron studies. Hopefully this will be at least partially realized in the near future.

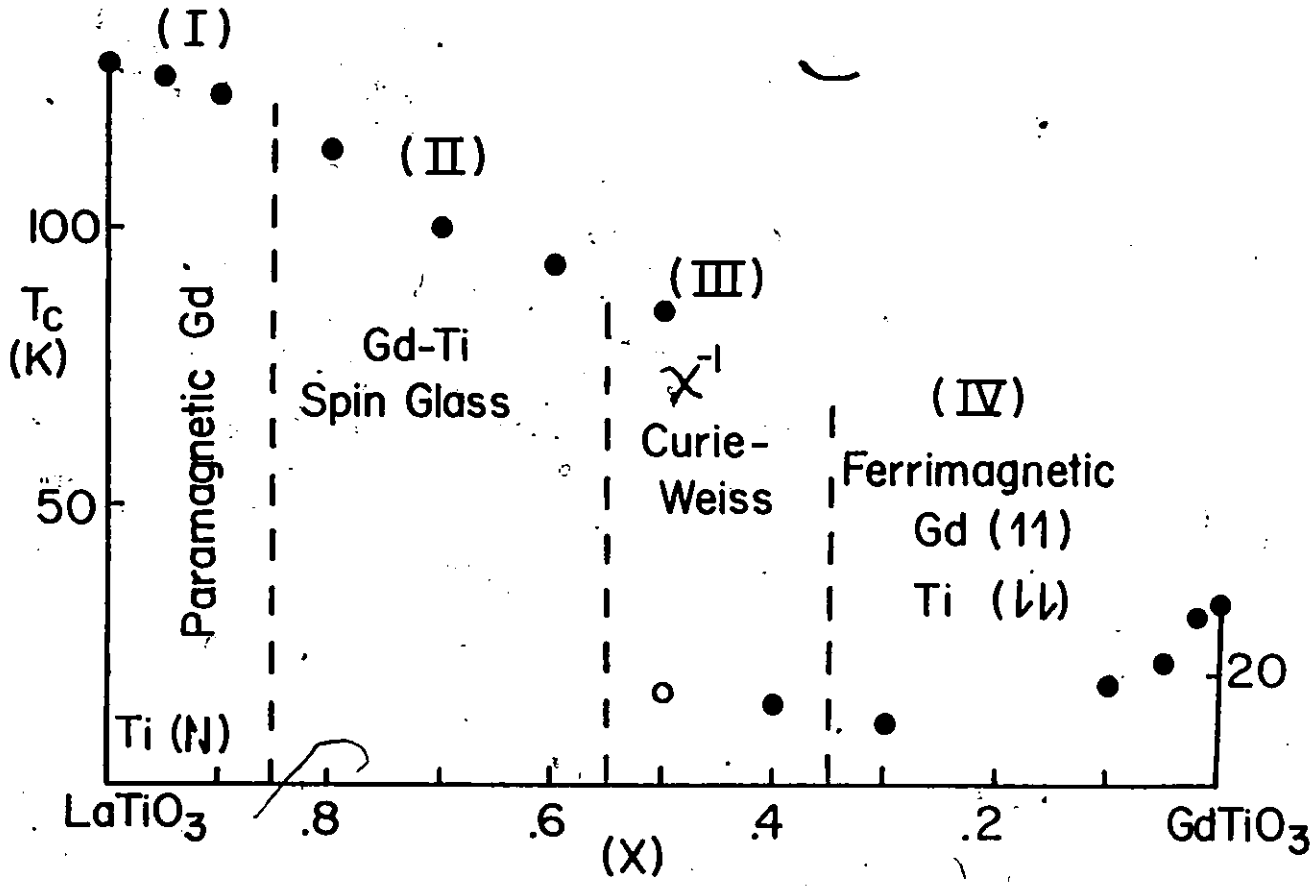

Fig. 6.11 Critical temperature vs. (effective rare earth radius)^3 for the $La_xGd_{1-x}TiO_3$ system.

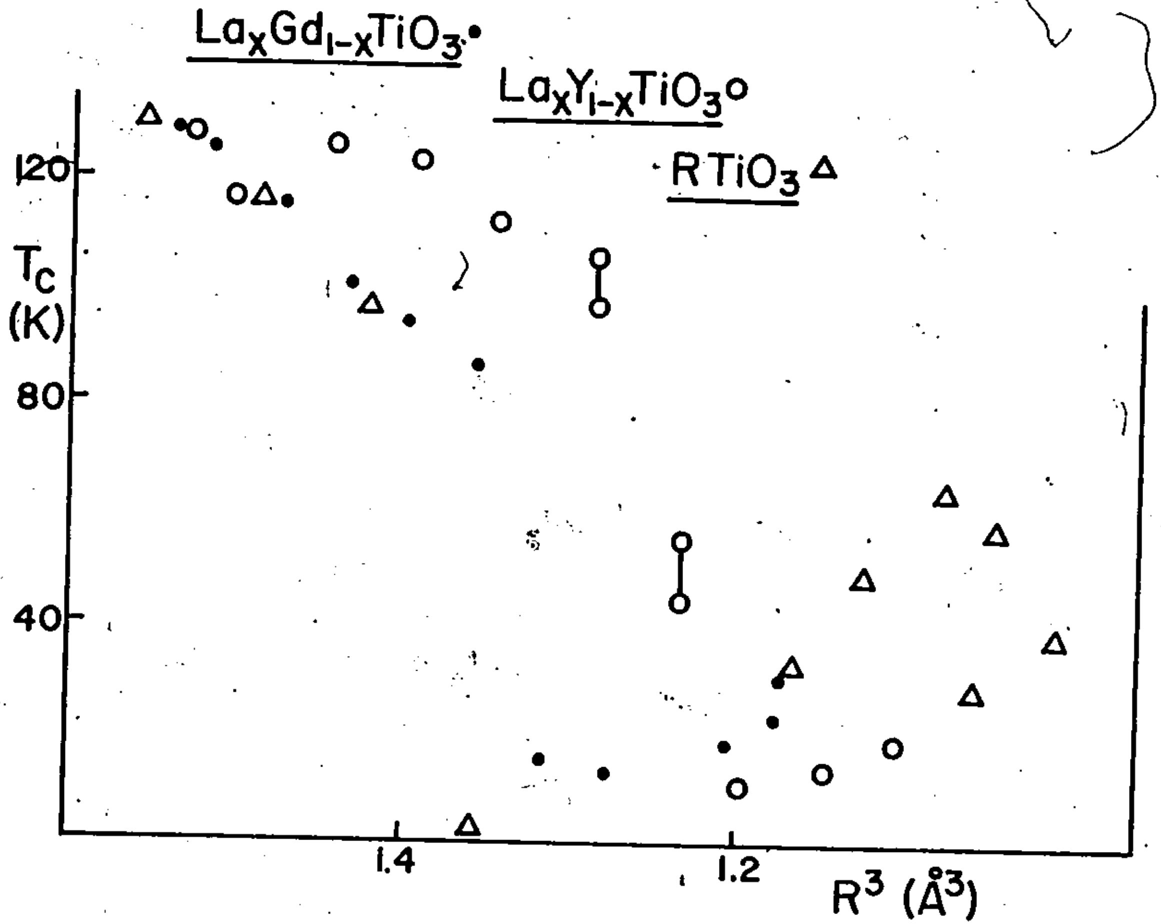

Fig. 6.12 Critical temperature vs. (effective rare earth radius)^3 for the $RTiO_3$, $La_xY_{1-x}TiO_3$ and $La_xGd_{1-x}TiO_3$ systems.

Table 6.1

Critical temperatures (T_c), low temperature anomalies (LTA), Neel hyperbola parameters (θ, C, ξ, θ) and magnetic coupling constants* (γGd-Ti, γTi-Ti, γGd-Gd) for $La_xGd_{1-x}TiO_3$.

	T_c	LTA(K)	μSAT Ti^{3+} (μ_B/ion)	θ	C	ξ	θ'	γ_{Ti-Gd}	γ_{Ti-Ti}	γ_{Gd-Gd}	$C(Ti^{3+})$
									(mole cm^{-3})		(cm^3 K $mole^{-1}$)
$GdTiO_3$	33(2)		1.1(.2)	-13(5)	7.9(1)	140(40)	30(5)	-23.8	40.6	.3	.01
$La_{.02}$	30(2)		1.0(.2)	-4(4)	7.77(9)	80(40)	30(10)	-17.6	43.4	1.0	.06
$La_{.05}$	22(2)		1.0(.2)	-6(5)	7.4(1)	90(4)	15(8)	-18.1	7.2	.9	-.07
$La_{.1}$	18(2)		1.0(.2)	-3(3)	7.07(9)	60(30)	14(10)	-14.9	10.6	1.2	.01
$La_{.3}$	12(2)			-3(1)	5.60(4)	20(10)	8(7)	-9.1	5.3	.6	.10
$La_{.4}$	14(2)			3.7(2)	5.0(1)						
$La_{.5}$	85(7)	16(2)		-5.7(2)	4.01(1)						
$La_{.6}$	93(5)	16(2)									
$La_{.7}$	100(4)	14(2)									
$La_{.8}$	114(3)	13(2)									
$La_{.9}$	124(2)										
$La_{.95}$	127(2)										
$LaTiO_3$	130(2)										

---

*In calculating these parameters, the value of $C(Ti^{3+})$ was taken to be .355 as reported for $YTiO_3$ by Johnston (1975).

CHAPTER 7

GOODENOUGH'S THEORY APPLIED TO THE RARE EARTH ORTHOTITANITES

The magnetic properties of the $La_xY_{1-x}TiO_3$ and $La_xGd_{1-x}TiO_3$ systems have been investigated and comparisons made with the $RTiO_3$ phases containing a single rare earth species. The results are in qualitative agreement with Goodenough's theory. As the effective rare earth size decreases, Goodenough postulates that the magnetic structure of the Ti^{3+} sublattice changes from an antiferromagnetic spiral to a ferromagnetic spiral to a simple ferromagnet (Fig. 1.4). Neutron diffraction studies on $LaTiO_3$ do not suggest a spiral structure. Rather, a conventional G-type antiferromagnet is indicated. The magnetic behaviour of the La-rich members of both solid solution series seem consistent with this determination. The magnetic properties of the $RTiO_3$ compounds of intermediate rare earth size are complex and not understood. Accordingly, neutron diffraction data imply that the Ti^{3+} sublattice in $CeTiO_3$ may possess both appreciable ferromagnetic and antiferromagnetic components. Magnetic data collected on the heavier compositions in the $La_xY_{1-x}TiO_3$ and $La_xGd_{1-x}TiO_3$ systems indicate a ferromagnetically ordered Ti^{3+} sublattice. This has been confirmed by neutron diffraction for the phases $RTiO_3$(R = Tb^{3+}-Yb^{3+}) (Turner et al. 1981, Turner et al. 1980). The observed dependence of the ordering temperature on composition in the antiferromagnetic region is in conflict with the phenomenological diagram in Fig. 1.4.

Goodenough postulates itinerant electron behaviour for large values of the exchange integral b. This is consistent with high temperature resistivity data reported for $LaTiO_3$ and $CeTiO_3$ (MacLean and Greedan 1981). As b decreases, the electrons are predicted to become eventually localized. This is in agreement with the resistivity data presented for $La_{.1}Y_{.9}TiO_3$ and $La_{.2}Y_{.8}TiO_3$. Also, susceptibility data on the compositions $La_xY_{1-x}TiO_3$ ($x = 0 - .7$) may be rationalized in terms of a localized moment in the presence of a crystal field. The Ti^{3+} moments obtained from saturation magnetization measurements of $La_xGd_{1-x}TiO_3$ ($x = 0 - .1$) are consistent with a localized, spin only d^1 system. Goodenough's treatment does not consider rare earth-transition metal interactions. The observed correlations between the magnetic properties and the Ti-O-Ti bond angle for all the phases studied strongly suggests that Ti-Ti exchange is the dominant interaction.

In summary, the general features of the magnetic and transport behaviour of the $RTiO_3$ system are reproduced by Goodenough's theory. There is conclusive evidence confirming the change in sign of the Ti-Ti coupling. Resistivity data strongly suggest a transition between localized and itinerant electron character. It is unclear whether or not the complex magnetic behaviour observed for the phases of intermediate rare earth size are due to the spiral magnetic structure suggested by Goodenough. Certainly the low values of T_c estimated for these materials are not anticipated in Goodenough's model.

CHAPTER 8

CONCLUSIONS

The magnetic structures of $LaTiO_3$ and $CeTiO_3$ were determined by neutron diffraction. $LaTiO_3$ is a G-type antiferromagnet. Bulk magnetization data imply a ferromagnetic canting angle of less than 1° (MacLean and Greedan 1981). For $CeTiO_3$ the neutron data are ambiguous. The Ti^{3+} sublattice displays G-type and possibly F-type ordering. Below 60K, the Ce^{3+} moments appear to order in an F-type/C-type arrangement through weak coupling with the Ti^{3+} sublattice.

The extent of solid solution in the series $La_xY_{1-x}TiO_3$ and $La_xGd_{1-x}TiO_3$ was investigated. From X-ray powder data it appears that complete miscibility occurs in both series. The magnetic behaviour of both systems was studied. The results suggest a weakening of the antiferromagnetic Ti-Ti exchange as the Ti-O-Ti bond angle decreases from 157° ($LaTiO_3$). For sufficiently small bond angle, the Ti-Ti coupling appears to become ferromagnetic. A strong correlation was observed between the magnetic behaviour of the $La_xY_{1-x}TiO_3$, $La_xGd_{1-x}TiO_3$ and $RTiO_3$ (R = single Lanthanide^{3+} species) series and the rare earth ionic volume. The ionic volume also correlates with the Ti-O-Ti bond angle. This suggests that the magnetic interactions in these systems may be adjusted structurally through variation of the Ti-O-Ti bond angle as proposed by Goodenough (1971).

Resistivity measurements on $La_{.1}Y_{.9}TiO_3$ and $La_{.2}Y_{.8}TiO_3$ are indicative of localized electron behaviour. Crystal field calculations assuming a localized Ti^{3+} $3d^1$ electron have reproduced the general features of the susceptibility data of the phases $La_xY_{1-x}TiO_3$ ($x = 0, .1, .2, .4, .7$). The saturation moment of $5.8 \pm .2$ μ_B/FU measured on a crystal of $GdTiO_3$ is consistent with a colinear 2-sublattice ferrimagnetic structure. The Ti^{3+} moment of $1.0 \pm .2$ μ_B extracted from single crystal saturation measurements on the phases $La_xGd_{1-x}TiO_3$ ($x = .02, .05, .1$) are indicative of a spin only d^1 system.

REFERENCES

Anderson, P.W., Phys. Rev. 79, 350 (1950).

Aschroft, N.W. and Mermin, N.D., Solid State Physics, Holt Rinehart and Winston, New York, 1976.

Bacon, G.E., Neutron Diffraction, Clarendon, Oxford, 1967.

Bazuev, G.V., Iutin, N.N., Matveenko, I.I. and Shveiken, G.P., Fiz. Tverd. Tela 17, 1167 (1975).

Bazuev, G.V., Makarova, O.V. and Shvieken, G.P., Neorg. Khim. 23, 1451 (1978).

Bazuev, G.V. and Shveiken, G.P., Izv. Akad. Nauk. SSSR, Neorg. Mater. 14, 267 (1978).

Beck, P.A., Phys. Rev. B23, 2290 (1981).

Bertaut, E.F. in Magnetism, Vol. III, G.T. Rado and H. Suhl eds., Academic Press, New York, 1963.

Bertaut, E.F. and Maréschal, J., Solid State Comm. 5, 93 (1967).

Blazey, B.K. and Rohrer, H., Helv. Phys. Acta 40, 370 (1967).

Boudreaux, E.A. and Mulay, L.N., Theory and Applications of Molecular Paramagnetism, Wiley and Sons, New York, 1976.

Cannella, V. and Mydosh, J.A., Phys. Rev. B6, 4220 (1972).

Courths, R. and Huffner, S., Z. Phys. B22, 245 (1975).

Cullity, B. D., Introduction to Magnetic Materials, Addison Wesley, New York, 1972.

Dirac, P.A.M., Proc. Roy. Soc. A112, 661 (1926).

Dirac, P.A.M., Proc. Roy. Soc. A123, 714 (1929).

Dzialoshinski, I.E., J. Phys. Chem. Solids 4, 241 (1958).

Ford, P.J., Contemp. Phys. 23, 141 (1982).

Freeman, A.J. and Watson, R.E., Acta Cryst. 14, 27 (1961).

Garrett, J.D., Greedan, J.E. and MacLean, D.A., Mater. Res. Bull. 16, 145 (1981).

Gerloch, M. and Miller, J.R., Progr. Inorg. Chem. 10, 1 (1968).

Goodenough, J.B., J. Phys. Chem. Solids 6, 287 (1958).

Goodenough, J.B., Magnetism and the Chemical Bond, Wiley and Sons, New York, 1963.

Goodenough, J.B., J. Appl. Phys. 37, 1415 (1966).

Goodenough, J.B., Prog. Solid State Chem. 5, 145 (1971).

Goodenough, J.B. and Longo, J.M., Crystallographic and Magnetic Properties of Perovskite and Perovskite-Related Compounds, Landholt-Bornstein Tabellen, Neue Serie III/4a, Springer-Verlag, Berlin, 1970.

Greedan, J.E. and MacLean, D.A., Inst. Phys. Conf. Ser., No. 37, 249 (1978).

Greedan, J.E. and Seto, K., Mat. Res. Bull. 16, 1479 (1981).

Heisenberg, W., Z. Phys. 38, 411 (1926).

Hornreich, R.M., J. Magn. Magn. Mat. 7, 280 (1978).

Hutchings, M.T., Solid State Physics 16, 227 (1964).

Johnston, D., Ph.D. Thesis, University of California, San Diego, 1975.

Kanamori, J., J. Phys. Chem. Solids 10, 87 (1959).

Keffer, F., Handbuch der Physik, XVII/2, H.P.J. Wijn ed., Springer-Verlag, Berlin, 1966.

Kestigian, M., and Ward, R., J. Am. Chem. Soc. 77, 6199 (1955).

Larson, A.C., Acta Cryst. 23, 664 (1967).

Laudise, R.A., The Growth of Single Crystals, Prentice-Hall, Englewood, 1970.

Levine, I.N., Quantum Chemistry, Allyn and Bacon, Boston, 1974.

Mabbs, F.E. and Machin, D.J., Magnetism and Transition Metal Complexes, Chapman and Hall, London, 1973.

MacLean, D.A., Ph.D. Thesis, McMaster University, Hamilton, 1980.

MacLean, D.A. and Greedan, J.E., Inorg. Chem. 20, 1025 (1981).

MacLean, D.A., Ng, Hok-Nam and Greedan, J.E., J. Solid State Chem. 30, 35 (1979).

MacLean, D.A., Seto, K. and Greedan, J.E., J. Solid State Chem. 40, 241 (1981).

Maletta, H. and Felsch, W., Phys. Rev. B20, 1245 (1979).

Martin, R.L. in New Pathways in Inorganic Chemistry, E.A.V. Ebsworth ed., Cambridge University Press, Cambridge, 1968.

Mattis, D.C., The Theory of Magnetism, Harper and Row, New York, 1965.

Moriya, T., Phys. Rev. 120, 91 (1960).

Morrish, A.H., The Physical Principles of Magnetism, Wiley and Sons, New York, 1965.

Mydosh, J.A., J. Magn. Magn. Mat. 7, 237 (1978).

Néel, L., Ann. Phys. (Paris) 3, 137 (1948).

Ofer, S., Nowik, I. and Cohen, S.G. in Chemical Application of Mössbauer Spectroscopy, V.I. Goldonskii and R.H. Herber eds., Academic Press, New York, 1968.

Orton, J.W., Electron Paramagnetic Resonance, Gordon and Breach, New York, 1968.

Prather, J.L., Atomic Energy Levels in Crystals, N.B.S. Monograph No. 19, 1961.

Shamir, N., Shaked, H. and Shtriknan, S., Physica 90B, 211 (1977).

Shannon, R.D., Acta Cryst. A32, 751 (1976).

Smart, J.S., Effective Field Theories of Magnetism, Saunders, Philadelphia, 1966.

Stassis, C., Deckman, H.W., Harmon, B.N., Desclaux, J.P. and Freeman, A.J., Phys. Rev. B15, 369 (1977).

Stevens, K.W.H., Proc. Phys. Soc. (London) A65, 209 (1952).

Stevens, K.W.H., Proc. Roy. Soc. A219, 542 (1953).

Tholence, J.L., Holtzberg, F., McGuire, T.R. and von Molnar, S., J. Appl. Phys. 50, 7350 (1979).

Tofield, B.C. and Scott, W.R., J. Solid State Chem. 10, 183 (1974).

Toulouse, G., Comm. Phys. 2, 115 (1977).

Turner, C.W., Collins, M.F. and Greedan, J.E., J. Magn. Magn. Mat. 23, 265 (1981).

Turner, C.W. and Greedan, J.E., J. Solid State Chem. 34, 207 (1980).

Turner, C.W., Greedan, J.E. and Collins, M.F., J. Magn. Magn. Mat. 20, 165 (1980).

Van der Pauw, L.J., Philips Res. Rep. 13, 1 (1958).

van Vleck, J.H., Phys. Rev. 52, 1178 (1937).

van Vleck, J.H., The Theory of Electric and Magnetic Susceptibilities, Oxford University Press, Oxford, 1965.

Weber, M.J. and Varitimos, T.E., J. Appl. Phys. 45, 810 (1974).

Weiss, P., J. Phys. Radium 4, 661 (1907).

Woolfson, M.M., An Introduction to X-Ray Crystallography, Cambridge University Press, Cambridge, 1970.

APPENDIX I

X-RAY CRYSTAL STRUCTURE OF $La_{.2}Y_{.8}TiO_3$

Space group	Pbnm	
Unit cell parameters	$a = 5.395(3)$, $b = 5.672(3)$, $c = 7.684(5)$	
Crystal Size	sphere	$r = .05$ mm
$\mu R = 1.35$		
Maximum 2θ	55°	
Radiation	Mo $K\alpha_1$	$\lambda = .70926$ Å
Independent reflections	280	
$(I > 0)$	241	
Function minimized	$\Sigma\omega(\lvert F_o\rvert - \lvert F_c\rvert)^2$	
g secondary extinction (Larson, 1967)	7.7×10^{-6}	
Weighting	$\omega = (\sigma^2 + .0004\, F_o^2)^{-1}$	
Final unweighted $R_1^{(a)}$	.0226	
Final weighted $R_2^{(b)}$	.0303	

(a) $R_1 = \dfrac{\Sigma(\lvert F_o\rvert - \lvert F_c\rvert)}{\Sigma\lvert F_o\rvert}$ (b) $R_2 = \Sigma\omega\left(\dfrac{(\lvert F_0\rvert - \lvert F_c\rvert)^2}{\Sigma F_o^2}\right)^{1/2}$

Table I.1

$La_{.2}Y_{.8}TiO_3$

Positional and Thermal Parameters (× 10^4)

	R	Ti	01	02
X	.98214(17)	.5	.5	.6934(6)
Y	.06751(16)	0	.1118(9)	.3059(6)
Z	.25	.5	.4635(9)	.0559(5)
U_{11}	47(5)	27(6)	134(25)	56(16)
U_{12}	46(5)	29(5)	54(24)	65(18)
U_{13}	78(5)	51(5)	33(21)	98(16)
U_{12}	-11(4)	-3(3)	-26(21)	-46(13)
U_{13}	0.	2(4)	0.	13(12)
U_{23}	0.	-2(4)	0.	1(13)

Bond Angles (°)

Ti(2)-01(1)-Ti(1)	143.24(.27)
Ti(2)-02(7)-Ti(4)	145.14(.19)

Ti-O-Ti average = 144.19(.46)

Table I.2

Structure Factors for $La_{.2}Y_{.8}TiO_3$

H	K	L	F_o	F_c
0	0	2	47.04	49.70
0	0	4	148.74	151.95
0	0	6	61.02	64.91
0	0	8	91.76	90.80
0	0	10	43.43	41.17
0	2	0	117.56	113.76
0	2	1	71.81	69.78
0	2	2	61.03	57.65
0	2	3	87.96	88.33
0	2	4	111.91	112.86
0	2	5	45.17	46.22
0	2	6	17.45	16.11
0	2	7	54.73	55.54
0	2	8	87.24	87.05
0	2	9	40.78	39.07
0	4	0	46.93	47.26
0	4	1	86.66	88.50
0	4	2	51.98	51.26
0	4	3	57.97	57.54
0	4	4	35.48	35.78
0	4	5	80.58	80.70
0	4	6	35.01	35.32
0	4	7	48.49	47.50
0	4	8	24.52	23.20
0	6	0	15.43	16.44
0	6	1	27.45	27.36
0	6	2	89.33	90.51
0	6	3	40.26	40.04
0	6	4	19.59	19.64
0	6	5	18.15	16.93
1	0	1	17.08	15.54
1	0	3	36.38	33.67
1	0	5	25.18	25.89
*1	0	7	9.16	8.16
1	1	0	38.54	39.36
1	1	1	52.55	51.32
1	1	2	127.87	125.68
1	1	3	57.92	59.83
1	1	4	29.38	30.31
1	1	5	31.75	31.96
1	1	6	99.81	103.74
1	1	7	34.49	34.84
1	1	8	20.45	20.39
1	1	9	26.32	24.60
1	2	0	11.23	9.72
1	2	1	16.71	14.23
1	2	2	34.12	33.00
1	2	3	19.36	18.66
*1	2	4	8.66	9.81
1	2	5	17.43	16.96
*1	2	6	5.40	3.89
1	2	7	7.78	7.16
1	2	8	14.09	15.14
*1	2	9	2.02	.77
1	3	0	44.24	43.35
1	3	1	104.51	101.16
1	3	2	76.59	75.75
1	3	3	89.40	90.61
1	3	4	25.93	26.59
1	3	5	80.50	82.55
1	3	6	49.77	48.78
1	3	7	63.65	64.01
1	3	8	14.05	12.97
1	3	9	55.10	52.71
1	5	0	76.04	75.37
1	5	1	72.20	72.91
1	5	2	10.90	10.90
1	5	3	67.57	66.29
1	5	4	70.88	70.54
1	5	5	61.55	61.13
*1	5	6	8.12	4.43
1	5	7	50.85	50.04
*1	6	0	3.37	3.49
*1	6	1	7.72	5.20
1	6	2	17.60	17.24
1	6	3	13.79	12.65
*1	6	4	4.40	6.07
*1	6	5	2.63	1.36
1	7	0	86.95	87.67
1	7	1	13.18	13.79
1	7	2	27.67	27.19
2	0	0	131.28	125.24
2	0	2	78.02	75.12
2	0	4	123.91	125.83
2	0	6	32.31	33.01
2	0	8	98.18	99.36
2	1	0	22.49	19.84
2	1	1	47.85	46.16
2	1	2	25.28	24.25
2	1	3	30.73	30.20
*2	1	4	2.35	3.10
2	1	5	32.04	33.94
2	1	7	20.64	19.81
2	1	8	12.30	11.71
2	1	9	18.33	17.55
2	2	0	128.19	131.76
2	2	1	78.41	81.07
2	2	2	7.55	6.80

H	K	L	F_o	F_c
2	2	3	55.69	58.04
2	2	4	97.75	103.70
2	2	5	65.24	68.24
2	2	6	18.73	18.91
2	2	7	44.55	44.29
2	2	8	63.68	61.84
2	2	9	39.99	38.35
2	3	0	20.16	21.00
2	3	1	10.16	10.62
2	3	2	6.83	6.65
2	3	3	24.70	26.00
2	3	4	12.25	12.45
2	3	6	12.50	12.31
2	3	7	13.18	14.22
*2	3	8	5.88	5.10
2	4	0	30.50	30.36
2	4	1	73.75	75.29
2	4	2	46.57	47.06
2	4	3	84.56	86.38
2	4	4	28.06	28.21
2	4	5	54.53	55.20
2	4	6	38.83	39.16
2	4	7	60.76	60.94
*2	5	0	8.33	8.97
*2	5	1	2.61	2.85
*2	5	2	5.21	4.41
2	5	3	13.17	14.50
*2	5	4	4.19	6.06
*2	5	5	2.70	3.49
*2	5	6	5.59	6.10
2	6	0	25.54	26.28
2	6	1	37.78	38.48
2	6	2	77.39	77.60
2	6	3	25.25	26.03
2	6	4	20.03	19.49
2	6	5	38.17	37.18
*2	7	0	9.62	11.48
2	7	1	15.31	14.49
3	0	1	16.05	16.23
3	0	3	31.54	31.78
3	0	5	8.60	9.31
3	0	7	20.74	19.59
3	0	9	13.87	12.59
3	1	0	36.02	35.04
3	1	1	47.24	46.37
3	1	2	129.06	129.22
3	1	3	17.67	16.70
3	1	4	35.84	36.36
3	1	5	43.68	44.82
3	1	6	93.00	95.69
3	1	7	16.68	17.11
3	1	8	28.05	28.46
3	2	0	38.99	37.78
3	2	1	13.73	14.19
3	2	2	21.75	22.68
*3	2	3	4.52	3.29
3	2	4	25.06	25.55
3	2	5	15.96	15.91
3	2	6	21.83	22.91
*3	2	7	5.21	5.23
3	2	8	12.81	13.58
*3	3	0	2.14	3.72
3	3	1	69.91	71.55
3	3	2	55.73	56.82
3	3	3	73.56	75.83
3	3	4	9.97	10.37
3	3	5	54.65	54.74
3	3	6	58.33	57.89
3	3	7	55.38	54.17
3	3	8	18.95	18.12
3	4	0	24.13	23.54
*3	4	1	9.35	10.41
3	4	2	36.15	37.05
*3	4	3	6.45	6.62
3	4	4	27.43	27.09
*3	4	5	8.63	9.63
3	4	6	20.00	20.78
*3	4	7	1.68	5.37
3	5	0	78.56	79.05
3	5	1	52.38	52.02
*3	5	2	11.75	11.95
3	5	3	51.56	52.38
3	5	4	61.42	61.51
3	5	5	44.03	42.47
3	5	6	11.44	4.52
3	6	0	21.19	21.88
3	6	1	20.99	19.90
3	6	2	10.80	10.69
3	6	3	15.27	16.29
3	6	4	16.29	15.05
4	0	0	113.73	114.60
4	0	2	23.94	24.45
4	0	4	96.98	96.78
4	0	6	23.91	22.98
4	0	8	69.63	68.12
4	1	0	38.66	37.59
4	1	1	35.39	35.58
*4	1	2	1.96	2.36
4	1	3	39.99	41.05
4	1	4	16.77	16.39
4	1	5	25.05	25.35
4	1	6	17.31	18.28
4	1	7	27.07	28.07
4	2	0	80.69	79.76
4	2	1	60.20	59.84
*4	2	2	5.64	6.35

H	K	L	F_o	F_c
4	2	3	56.20	57.04
4	2	4	70.21	71.96
4	2	5	46.76	48.24
* 4	2	6	2.85	5.23
4	2	7	41.58	41.63
4	3	0	24.64	22.70
4	3	1	18.07	16.74
4	3	2	36.68	37.16
* 4	3	3	2.60	2.65
4	3	4	26.81	26.48
4	3	5	19.79	21.07
4	3	6	20.67	21.26
* 4	3	7	5.52	1.81
4	4	0	28.19	25.13
4	4	1	69.51	69.32
4	4	2	45.44	46.12
4	4	3	62.39	63.01
4	4	4	21.34	21.23
4	4	5	59.24	59.17
4	4	6	36.62	36.06
4	5	0	18.90	18.54
4	5	1	19.79	19.34
4	5	2	23.00	23.03
* 4	5	3	6.22	4.19
4	5	4	17.56	18.65
4	6	0	17.67	16.07
4	6	1	33.86	33.93
5	0	1	42.76	42.67
5	0	3	44.15	43.82
5	0	5	33.33	33.41
5	0	7	32.73	32.76
5	1	0	35.57	35.44
5	1	1	19.28	19.26
5	1	2	92.79	93.09
5	1	3	35.41	35.89
5	1	4	26.58	26.68
* 5	1	5	9.37	8.96
5	1	6	80.20	79.89
5	2	0	31.81	31.82
5	2	1	28.74	28.00
5	2	2	26.28	25.55
5	2	3	23.75	24.36
5	2	4	26.86	26.19
5	2	5	23.91	24.32
5	2	6	22 59	22.88
5	3	0	23.43	23.80
5	3	1	54.06	53.98
5	3	2	63.17	63.48
5	3	3	41.96	42.74
* 5	3	4	10.84	11.98
5	3	5	48.45	49.28
5	4	0	28.46	28.96
* 5	4	1	5.11	4.46
5	4	2	32.81	32.93
* 5	4	3	6.86	5.36
5	4	4	28.05	27.89
5	5	0	40.04	39.58
5	5	1	38.48	38.53
6	0	0	87.08	87.14
6	0	2	12.92	12.35
6	0	4	73.34	73.58
* 6	1	0	9.50	7.52
6	1	1	32.67	33.54
6	1	2	25.33	26.43
6	1	3	27.62	27.27
6	1	4	15.32	15.16
6	1	5	30.59	30.38
6	2	0	56.79	56.62
6	2	1	36.68	35.98
* 6	2	2	7.13	5.37
6	2	3	39.89	39.84
6	2	4	55.15	54.83
6	3	0	46.50	45.04
* 6	3	1	3.67	3.62
6	3	2	34.37	34.26
6	3	3	13.64	13.31

* unobserved reflection

APPENDIX II

THERMAL PARAMETERS FOR $LaTiO_3$

$$U = \frac{\sqrt{U_{11}^2 + U_{22}^2 + U_{33}^2}}{3} \qquad B = 8\pi^2 U$$

From MacLean et al., 1979

$U_{La}^{298} = 1.52 \times 10^{-4}$ $\qquad B_{La}^{298} = 1.20$

$U_{Ti}^{298} = 86 \times 10^{-4}$ $\qquad B_{Ti}^{298} = .68$

$U_{01}^{298} = 218 \times 10^{-4}$ $\qquad B_{01}^{298} = 1.72$

$U_{02}^{298} = 192 \times 10^{-4}$ $\qquad B_{02}^{298} = 1.52$

Assume $B = 0$ at $T = 0$ and scales linearly with temperature. Good agreement was observed for $LaTiO_3$ using values equal to .7 B_{calc}.

<u>B</u>

	148K(152K)	(81K)	10K
La(Ce)	.43	.23	.03
Ti	.24	.13	.02
01	.62	.34	.04
02	.54	.30	.04